Dissertation

Materials with exotic magnetic interactions: First principles computer simulations

Submitted in Fulfillment

of the Requirements for the Degree of

Doctor of Technical Sciences
(Doktor der technischen Wissenschaften)

at the Technical University of Vienna

(Technische Universität Wien)

Faculty of Physics

under supervision of

Ao. Univ. Prof. Dipl.-Ing. Dr. techn. Peter Mohn

Institut für Allgemeine Physik (E 134)

by

Dipl.-Ing. Martin Sieberer

(9926057)

Vienna, August 2007

. . . to my family

Contents

Abstract

The aim of the present work is to study the magnetic properties of seminal materials such as magnetic semiconductors (part II) and weak itinerant ferromagnets (part III). Recently magnetic semiconductors are very much in the center of attention, in particular in the emerging field of spin-based electronics. Researchers try to exploit the electrons' magnetic properties (e.g. their spin) to transport information. Weak itinerant ferromagnets are also very promising materials because their ferromagnetism is not very stable and can easily be tuned by external parameters like pressure or stoichiometry. Weak itinerant ferromagnets can be used for example in magneto-caloric applications like refrigerators. The investigations are done by applying density functional theory (DFT), one of the most powerful techniques for gaining a detailled understanding of real materials. In general, computer simulations have several advantages if done supplementary to experiment. For example one can study "hypothetical" materials with crystal structures or magnetic states usually not found in nature. In such an approach questions can be answered beyond the scope of experiment, e.g. why certain structures are found in nature and others are not. A thorough understanding of the relation between atomic structure and macroscopic, physical properties is the key requirement for the success in the design of so-called functional materials.

In part I of this work a short introduction into the theory of electronic structure methods and magnetism is given. In part II two completely different magnetic semiconductors are discussed. The binary I/II-V compounds (prototype CaAs) in the hypothetical zinc-blende structure belong to the so-called concentrated magnetic semiconductors (CMS). CaAs and related I/II-V compounds might be prepared as thin films and in that form were very promising materials for spintronics [A]. The second class of materials investigated, Cu_2O doped with Mn, Fe, Co, and Ni, belongs to the dilute magnetic semiconductors (DMS). The compounds derived from Cu_2O have already been prepared in experiment. They yield very diverse physical properties ranging from room-temperature ferromagnetism to spin-glass behavior [D]. In part III metals in the perovskite structure are in the center of attention. First the series TCu_3N with T=Pd, Rh, and Ru is investigated [B]. It is demonstrated that electron localization and magnetism can occur also for a material having 4d electrons, which is a very rare phenomenon. Subsequently $AlCNi_3$ and $GaCNi_3$ serve as examples demonstrating how tightly carbon stoichiometry and magnetism are connected [C]. Mo-cluster compounds (prototype $GaMo_4S_8$) studied in [E] owe their interesting magnetic properties to well-separated Mo_4 clusters and narrow, partially filled Mo 4d cluster orbitals. Finally non-collinear magnetism, a highly challenging field, is touched by studying $TNMn_3$ with T=Cu, Zn, Ga, and Ge.

The following publications were written in the context of this work:

A   M. Sieberer, J. Redinger, S. Khmelevskyi, and P. Mohn, *Ferromagnetism in tetrahedrally coordinated compounds of I/II-V elements: Ab initio calculations*, Phys. Rev. B **73**, 024404 (2006).

B   M. Sieberer, S. Khmelevskyi, and P. Mohn, *Magnetic instability within the series TCu_3N (T=Pd, Rh, and Ru): A first-principles study*, Phys. Rev. B **74**, 014416 (2006).

C   M. Sieberer, P. Mohn, and J. Redinger, *Role of carbon in $AlCNi_3$ and $GaCNi_3$: A density functional theory study*, Phys. Rev. B **75**, 024431 (2007).

D   M. Sieberer, J. Redinger, and P. Mohn, *Electronic and magnetic structure of cuprous oxide Cu_2O doped with Mn, Fe, Co, and Ni: A density-functional theory study*, Phys. Rev. B **75**, 035203 (2007).

E   M. Sieberer, S. Turnovszky, J. Redinger, and P. Mohn, *The importance of cluster-distortions in the tetrahedral cluster compounds: Ab initio investigations*, to be published in PRB (2007).

Kurzfassung

Ziel der hier vorliegenden Arbeit ist es, zukunftsträchtige Materialien wie beispielsweise magnetische Halbleiter (Teil II) oder schwach itinerante Ferromagnete (Teil III) hinsichtlich ihrer magnetischen Eigenschaften zu untersuchen. Besonders magnetische Halbleiter stehen in der letzten Zeit im Zentrum der Aufmerksamkeit. Forscher auf dem Gebiet der spin-basierten Elektronik verwenden diese um die magnetischen Eigenschaften der Elektronen (deren Spin) für den Informationstransport zu nutzen. Schwach itinerante Ferromagnete sind ebenfalls sehr vielversprechende Materialien, besonders deshalb weil ihr Ferromagnetismus nicht sehr "stabil" ist und somit gezielt durch äußere Einflüsse wie Druck oder Stöchiometrie verändert werden kann. Schwach itinerante Ferromagnete können beispielsweise in magneto-kalorischen Anwendungen (z.B. Kältetechnik) verwendet werden. Zur Untersuchung wird die Dichte-Funktional Theorie (DFT) herangezogen, eine der leistungsstärksten Techniken zur Beschreibung realer Materialien. Im Allgemeinen haben Computersimulationen viele Vorteile, vorausgesetzt sie werden als Ergänzung zum Experiment genutzt. Beispielsweise können hypothetische Materialien untersucht werden. Dazu zählen Verbindungen mit Kristallstrukturen oder in magnetischen Zuständen, die in der Natur gewöhnlich nicht vorkommen. Dies gestattet es, Fragen zu beantworten die das Experiment nicht oder nur sehr schwer beantworten kann, z.B. warum gewisse Strukturen in der Natur vorkommen und andere nicht. Ein tiefes Verständnis für den Zusammenhang zwischen der atomaren Struktur und den makroskopischen, physikalischen Eigenschaften ist die zentrale Voraussetzung für den Erfolg im Design sogenannter funktioneller Materialien.

Im ersten Teil dieser Arbeit wird eine kurze Einführung in die Theorie der Elektronenstruktur und des Magnetismus gegeben. In Teil II werden zwei völlig verschiedene magnetische Halbleiter vorgestellt. Die binären Verbindungen vom Typ I/II-V (Prototyp CaAs) in der hypothetischen Zinkblende Struktur gehören zu den sogenannten konzentrierten magnetischen Halbleitern (CMS). CaAs und verwandte I/II-V Verbindungen könnten in der Form dünner Schichten hergestellt werden und wären vielversprechende Materialien für die spin-basierte Elektronik [A]. Die zweite untersuchte Materialklasse, Cu_2O dotiert mit geringen Konzentrationen von Mn, Fe, Co und Ni, gehört zu den verdünnten magnetischen Halbleitern (DMS) und wurde bereits experimentell hergestellt. Die von Cu_2O abgeleiteten Verbindungen zeigen vielfältige physikalische Eigenschaften wie z.B. Ferromagnetismus bei Raumtemperatur sowie Spin-Glas Verhalten [D]. In Teil III stehen Metalle in der Perovskit-Struktur im Zentrum der Aufmerksamkeit. Zuerst wird die Serie TCu_3N mit T=Pd, Rh und Ru untersucht [B]. Es wird gezeigt, dass die Lokalisierung von Elektronen und der daraus resultierende Magnetismus auch in einem Material mit 4d Elektronen auftreten

kann, ein Phänomen das extrem selten ist. Anschließend dienen $AlCNi_3$ and $GaCNi_3$ als Beispiel dafür, wie eng Kohlenstoff-Stöchiometrie und Magnetismus miteinander verknüpft sein können [C]. Schließlich werden die sogenannten Mo-Cluster Verbindungen (Prototyp $GaMo_4S_8$) untersucht. Deren interessante magnetische Eigenschaften ergeben sich aus räumlich weit voneinander getrennten Mo_4 Clustern und den daraus resultierenden schmalen Mo 4d-Bändern [E]. Der letzte Teil der vorliegenden Arbeit ist ein kurzer Exkurs in das für die Forschung sehr interessante Gebiet des nicht-kollinearen Magnetismus, wobei die Serie $TNMn_3$ mit T=Cu, Zn, Ga und Ge als Beispiel herangezogen wird.

Die folgenden Publikationen entstanden im Zuge dieser Arbeit:

A   M. Sieberer, J. Redinger, S. Khmelevskyi, and P. Mohn, *Ferromagnetism in tetrahedrally coordinated compounds of I/II-V elements: Ab initio calculations*, Phys. Rev. B **73**, 024404 (2006).

B   M. Sieberer, S. Khmelevskyi, and P. Mohn, *Magnetic instability within the series TCu3N (T=Pd, Rh, and Ru): A first-principles study*, Phys. Rev. B **74**, 014416 (2006).

C   M. Sieberer, P. Mohn, and J. Redinger, *Role of carbon in AlCNi3 and GaCNi3: A density functional theory study*, Phys. Rev. B **75**, 024431 (2007).

D   M. Sieberer, J. Redinger, and P. Mohn, *Electronic and magnetic structure of cuprous oxide Cu2O doped with Mn, Fe, Co, and Ni: A density-functional theory study*, Phys. Rev. B **75**, 035203 (2007).

E   M. Sieberer, S. Turnovszky, J. Redinger, and P. Mohn, *The importance of cluster-distortions in the tetrahedral cluster compounds: Ab initio investigations*, to be published in PRB (2007).

Part I

Introduction

The history of magnetism reaches back far into the past. The first known application of a magnetic material is the compass. The oldest description of such a device was discovered in a chinese book of the year 1086. Nowadays a world without magnetic materials is not to be imagined. Their applications range from magnetic layers in hard discs, permanent magnets in electric motors to soft magnets in magnetic cores of transformers. Magnetism not only has great influence in our everyday lives, it is also of central interest for many research groups all over the world. The key issue of magnetism in solid state physics is to understand, predict and finally improve the magnetic properties of certain materials in order to improve or guarantee their applicability in particular devices. Examples for active research fields are numerous. Recently researchers try to combine the properties of conventional semiconductors with those of magnets. The aim is to develop a new kind of electronics, so-called spin-based electronics or shorter spintronics. In spintronics materials the electron spin in addition to its charge is actively used to process information. Also magnetic thin films are in the center of attention nowadays. They are used to store information on hard disks. One of their key quantity is the magnetic anisotropy, a measure for the energy (or temperature) required to change the magnetization direcion of a single bit stored within the magnetic layer. Many more examples for magnetic materials as part of technologically important devices could be listed. Those mentioned above were just meant to demonstrate that magnetism is not only a very interesting academic problem. It is also of great technological importance now and probably even more in the future.

Chapter 1

Basic theoretical background

Modern computational approaches are getting more and more successful in solving the solid state many-body problem. However, up to now there is no complete, unified theory of magnetism in matter. On the one hand this is due to the huge diversity of materials we know nowadays, ranging from metals over (magnetic) semiconductors or insulators to so-called strongly correlated and low-dimensional systems. On the other hand it is due to the difficulty coming from the many-body problem itself. As it is outlined below, the Schrödinger equation can only be solved after having performed many approximations. The most frequently used one assumes the electrons to be independent, feeling each others only in an averaged way. However, even though the computer can calculate many important quantities like for example the charge density, spin density, core level spectra, optical properties, etc. it is the scientist's job to interpret the results. The difficulty is to reduce the degrees of freedom in a way the results can be understood in terms of "simpler" models. Understanding is only possible if on the one hand the computational approach is appropriate for the description of the material of interest, and on the other hand if the scientist is already familiar with the huge number of phenomenological models being on the market nowadays. The following introduction is by no means complete, it is intended for making the reader familiar with the basic techniques.

1.1   The Schrödinger equation for a solid

One of the most important equations of theoretical solid state physics is the Schrödinger equation of electrons and nuclei combined in the solid. Throughout the work a time-independent formalism is used. This is not a serious restriction if one is interested in static properties like e.g. chemical bonding and static magnetic properties, which usually are measured on a time scale much larger than that of the internal degrees of freedom. In

order to keep notation simple and to introduce as much physics as possible without going deep into the mathematical formalism a non-relativistic description suitable for light elements (e.g. up to Z=50) is used. For the latter a fully relativistic treatment in the scope of the Dirac equation is not absolutely necessary. The most important relativistic corrections will be introduced in the context of the Hund rules.

In order to keep notation simpler, unless otherwise noted atomic units are used throughout the text. That implies the quantum of action $\hbar$, the electron mass m_e, and the elementary charge e to be unity. The naturally arising unit of energy is then called the Hartree (1 hartree = 27.208 eV) and the unit-length is called atomic unit (a.u.) or bohr, 1 bohr is equivalent to the first Bohr radius (1a.u. = 0.529177$\times 10^{-10}$ m).

The desired solution of the time-independent, non-relativistic Schrödinger equation is the wavefunction $\Psi = \Psi(\boldsymbol{r}_1, \boldsymbol{r}_2, \cdots, \boldsymbol{r}_N; \boldsymbol{R}_1, \boldsymbol{R}_2, \cdots, \boldsymbol{R}_M)$. It depends on the coordinates of all N electrons and M nuclei, in a bulk typically involving 10^{19} to 10^{23} particles. The first thing one knows about the solution is its symmetry due to electron exchange. In principle one can not distinguish between electrons. This has the important consequence that the wavefunction can either change sign upon an arbitrary exchange of 2 electrons (antisymmetric character) or remain unchanged (symmetric character). The spin statistics theorem says that the wavefunction has to be antisymmetric for half-spin particles (fermions) like the electron, and symmetric for integer-spin particles (bosons). This information, however, is not enough to make the problem tractable. The wavefunction still describes a system of typically 10^{19} to 10^{23} atoms and similarly many electrons mutually depending on each others. It is easy to accept that the full solution can not be obtained and approximations are absolutely necessary.

If one is interested mainly in the electronic properties of solids (excluding e.g. superconductivity), the first simplification usually performed is the Born-Oppenheimer approximation. An electron is approximately 1800 times lighter than a single proton or neutron. From the viewpoint of an electron the nucleus is only very slowly moving and its movement in a good approximation can be neglected at all. This is an enormous simplification because it allows for a decomposition of the full Hamiltonian into an independent electronic and ionic part. Without that separation electron-ion scattering would automatically be included also in the defect free, perfect solid and the electron quantum number $\boldsymbol{k}$ would no longer be conserved.

Thus the Hamilton Operator $\hat{H}$ of a solid containing N electrons and M nuclei (in atomic

units) is given by

$$\hat{H}(\boldsymbol{r}_i; Z_\mu, \boldsymbol{R}_\mu) \; = \; \hat{T} + \hat{V}_{Coul} = -\frac{1}{2} \sum_{i=1}^{N} \nabla_i^2 \; + \; \frac{1}{2} \sum_{i \neq j}^{N} \frac{1}{|\boldsymbol{r}_i - \boldsymbol{r}_j|}$$
$$- \; \sum_{i=1}^{N} \sum_{\mu=1}^{M} \frac{Z_\mu}{|\boldsymbol{r}_i - \boldsymbol{R}_\mu|} \; + \; \frac{1}{2} \sum_{\mu \neq \nu}^{M} \frac{Z_\mu Z_\nu}{|\boldsymbol{R}_\mu - \boldsymbol{R}_\nu|}. \tag{1.1}$$

The first term on the right hand side is the kinetic energy, the second one the Coulomb interaction between different electrons, followed by the Coulomb interaction between electrons and nuclei and between nuclei. Due to the Born-Oppenheimer approximation the ionic coordinates already enter the equation as fixed parameters. Thus one can neglect the last and constant term in above equation. Of course, after having solved the electronic problem this constant term will be added again in order to get the correct result for the total energy. More conveniently the Hamilton operator is often written as

$$\hat{H}(\boldsymbol{r}_i) \; = \; \hat{T} + \hat{V}_{ext} + \hat{V}_{Coul} =$$
$$-\frac{1}{2} \sum_{i=1}^{N} \nabla_i^2 + \sum_{i=1}^{N} v_{ext}(\boldsymbol{r}_i) + \frac{1}{2} \sum_{i \neq j}^{N} w(|\boldsymbol{r}_i - \boldsymbol{r}_j|). \tag{1.2}$$

This form will be referred to in the following. The second expression, v_{ext}, includes the interaction of the electrons with all M nuclei and (if present) with an external electric field. The third term is the electron-electron Coulomb interaction, equivalent to the second term on the right hand side of equation 1.1.

1.2 Consequences of periodicity

Above simplifications are still not enough to solve the many-body Schrödinger equation. We thus assume that the solids we are interested in are perfect single crystals or at least polycrystalline materials, with physical properties mainly determined by regions with a highly symmetric arrangement of atoms (neglecting grain boundaries, etc.). Consequently also the electrons feel a highly symmetric potential v_{ext}. A perfect single crystal can be divided into regions in space repeating each others. These unit cells can formally be accounted for by introducing primitive lattice translations $\boldsymbol{R}_j = l_j \boldsymbol{a} + m_j \boldsymbol{b} + n_j \boldsymbol{c}$. In three dimensions the lattice must belong to one out of the 14 Bravais lattices. The Bravais lattices have one conceptual advantage. Within the proper basis of the Bravais lattice the symmetry operations of the solid can be written as matrices containing simplify 0,+1 and -1 as elements. For a proper characterization of a material in addition to the lattice one

needs to specify the basis, the positions of the atoms within one unit cell relative to its origin. The more complex a material is the higher is the number of basis atoms within one cell. It is important to keep in mind that there are always several ways to describe the solid, usually the simplest combination of lattice and basis is used. Deviding the solid into repeating, identical unit cells has the advantage that one needs to consider only one out of 10^{19} to 10^{23} cells. The rest of the solid, which is assumed to be a perfect single-crystal from now on, can be neglected because it contributes no significant information. Mathematically this is expressed in Bloch's theorem:

$$v_{ext}(\boldsymbol{r} + \boldsymbol{R}_j) = v_{ext}(\boldsymbol{r}), \quad \boldsymbol{R}_j = l_j\boldsymbol{a} + m_j\boldsymbol{b} + n_j\boldsymbol{c} \longrightarrow$$
$$\Psi_{n\boldsymbol{k}}(\boldsymbol{r} + \boldsymbol{R}_j) = e^{i\boldsymbol{k}\boldsymbol{R}_j}\ \Psi_{n\boldsymbol{k}}(\boldsymbol{r}). \tag{1.3}$$

The only difference in the wavefunction when going from one unit cell to the next can be a phase factor. This ensures that the charge density, which is insensitive to the phase factor, has the full symmetry of the crystal. The only requirement is that $\boldsymbol{R}_j = l_j\boldsymbol{a} + m_j\boldsymbol{b} + n_j\boldsymbol{c}$ is a lattice translation, mapping atoms of one unit cell to equivalent ones in other cells. The next important step is to fix the boundary conditions. For the simplest case of free electrons it would be possible to demand $\Psi_{n\boldsymbol{k}}(\boldsymbol{r}) = 0$ at the border of the solid. However, this would destroy the above made assumption of translational symmetry and $\boldsymbol{k}$ would no longer be a conserved quantum number. Thus one usually assumes periodic boundary consitions:

$$\Psi_{n\boldsymbol{k}}(\boldsymbol{r} + N_1\boldsymbol{a}) = \Psi_{n\boldsymbol{k}}(\boldsymbol{r}) = \Psi_{n\boldsymbol{k}}(\boldsymbol{r} + N_2\boldsymbol{b}) = \Psi_{n\boldsymbol{k}}(\boldsymbol{r} + N_3\boldsymbol{c}) \tag{1.4}$$

The total number of unit cells is $N = N_1N_2N_3$, $\boldsymbol{a}, \boldsymbol{b}, \boldsymbol{c}$ are the primitive translations building up the lattice. Perfect periodicity leads to special solutions of the Schrödinger equation, so-called Bloch waves. In their most general form they can be expressed as

$$\Psi_{n\boldsymbol{k}}(\boldsymbol{r}) = \frac{1}{\sqrt{V}}\ u_{n\boldsymbol{k}}(\boldsymbol{r})\ e^{i\boldsymbol{k}\boldsymbol{r}}, \tag{1.5}$$

$u_{n\boldsymbol{k}}(\boldsymbol{r})$ is a plane wave coefficient that in its most general form depends on the coordinate $\boldsymbol{r}$. The phase factor $\boldsymbol{k}$ is called the electron wavenumber or electron quasi-momentum and is a conserved quantity. This is valid as long as there are no terms in the Hamiltonian coupling electronic states with different $\boldsymbol{k}$. Periodicity not only leads to the formal division of the crystal into unit cells, also in reciprocal space a lattice can be defined with the end points $\boldsymbol{G}_j = u_j\boldsymbol{A} + v_j\boldsymbol{B} + w_j\boldsymbol{C}$. $\boldsymbol{A}$, $\boldsymbol{B}$, and $\boldsymbol{C}$ are the primitive translation vectors connected to the real space vectors $\boldsymbol{a}, \boldsymbol{b}$, and $\boldsymbol{c}$ via

$$\boldsymbol{A} = 2\pi\frac{\boldsymbol{b} \times \boldsymbol{c}}{\boldsymbol{a} \cdot (\boldsymbol{b} \times \boldsymbol{c})}, \ \boldsymbol{B} = 2\pi\frac{\boldsymbol{c} \times \boldsymbol{a}}{\boldsymbol{a} \cdot (\boldsymbol{b} \times \boldsymbol{c})}, \ \boldsymbol{C} = 2\pi\frac{\boldsymbol{a} \times \boldsymbol{b}}{\boldsymbol{a} \cdot (\boldsymbol{b} \times \boldsymbol{c})}. \tag{1.6}$$

The reciprocal lattice is very useful because all quantities having the full symmetry of the crystal (e.g. charge density, potential) can be expanded in a Fourier series with a sum extending only over reciprocal lattice vectors $\boldsymbol{G}_j$. Moreover, all relevant information regarding $E(\boldsymbol{k})$ can be folded back into the first Brillouin zone due to $E(\boldsymbol{k}) = E(\boldsymbol{k} + \boldsymbol{G}_j)$ for all j. Moreover, if time-inversion symmetry holds one can further assume only positive $\boldsymbol{k}$ because of $E(\boldsymbol{k}) = E(-\boldsymbol{k})$.

1.3   Electrons in a weakly varying potential

In the free electron model the potentials of the atomic cores are completely neglected and so are the electron-electron interactions. The solutions of the free electron Schrödinger equation,

$$-\frac{1}{2} \triangle \Psi(\boldsymbol{r}) = E\Psi(\boldsymbol{r}), \tag{1.7}$$

are plane waves normalized to the volume V. The solutions are the eigenstates of the momentum operator ∇/i:

$$\Psi(\boldsymbol{r}) = \frac{1}{\sqrt{V}} \, e^{i\boldsymbol{k}\boldsymbol{r}}. \tag{1.8}$$

The free electron dispersion relation is a parabola, $E = \frac{k^2}{2}$. By imposing periodicity and introducing unit cells, even though there is no potential which would really motivate this step, one can plot the simplest form of a bandstructure possible. This is done by simply folding back the free electron bands into the (first) Brillouin zone, of course upon taking into account the correct crystal structure and hence the correct form of the Brillouin zone. This free electron empty lattice model can easily be improved by treating the nuclear potentials as a weak perturbation. This ansatz, however, is at best justified in a few cases like Cu or Al, for which more sophisticated approaches like the orthogonalized plane wave (OPW) technique and the pseudopotential (PP) approach showed that screening of almost fully occupied shells significantly reduces the positive core potentials. In those cases screening can be sufficient for free-electron like behavior to occur, explaining why Cu ($3\mathrm{d}^{10}$ + 1× 4s) and Al ($3\mathrm{s}^2$ + 1× 3p) with only one electron outside a filled shell roughly obey this description.

However, the perturbative treatment of $V(\boldsymbol{r})$ as a whole has turned out to be rather disappointing in general. In particular for materials with more strongly varying potentials (e.g. semiconductors) it is more successful to look at a particular region of the bandstructure in which $E(\boldsymbol{k})$ has an extremum, and to develop the energy around this extremum. This method is called $\boldsymbol{kp}$ method and usually applied to semiconductors. The name becomes obvious when inserting the general Bloch wave into the Schrödinger equation for

free electrons plus external potential v_{ext}:

$$-\frac{1}{2} \triangle u_{n\boldsymbol{k}}(\boldsymbol{r}) + [v_{ext}(\boldsymbol{r}) + \boldsymbol{k} \cdot \boldsymbol{p}] u_{n\boldsymbol{k}}(\boldsymbol{r}) = E_n u_{n\boldsymbol{k}}(\boldsymbol{r}). \tag{1.9}$$

The presence of the term $\boldsymbol{k} \cdot \boldsymbol{p}$ has important consequences. The symmetry of this "pseudo" Schrödinger equation for the periodic part of the solution, $u_{n\boldsymbol{k}}(\boldsymbol{r})$, depends on $\boldsymbol{k}$ and hence on the direction of the running wave of the electron (simply speaking). This $\boldsymbol{k}$ dependency reminds of the hydrogen atom, where spherical symmetry allows a decomposition of angular and radial differential equations. The coupling between both equations is due to the centrifugal term -l(l+1)/$\boldsymbol{r}^2$ in the radial equation, coupling the spherical symmetry (l-quantum number) to the energy. Since symmetry depends on the direction of $\boldsymbol{k}$, bandstructure plots $E_n(\boldsymbol{k})$ are usually performed for high symmetry directions.

1.4 Tightly bound electrons

The opposite border-case of nearly free electrons are almost localized, tightly bound electrons. This behavior is found if the wavefunction overlap of neighboring atoms is sufficiently small, e.g. for d or f-electrons with small radial expansion compared to internuclear distances. The tight binding approximation so as the free electron approximation neglects electron-electron interactions. The kinetic energy and the interaction with the external potential arising from the atomic cores are included. It is quite natural to start from solutions of the isolated atom centered at $\boldsymbol{R}_l$, $\phi(\boldsymbol{r} - \boldsymbol{R}_l)$, and to combine these solutions linearly in the solid,

$$\Psi_{n\boldsymbol{k}}(\boldsymbol{r}) = \sum_l e^{i\boldsymbol{k}\boldsymbol{R}_l} \phi(\boldsymbol{r} - \boldsymbol{R}_l). \tag{1.10}$$

The functions $\phi(\boldsymbol{r} - \boldsymbol{R}_l)$ are called Wannier functions and the phase factor is necessary in order to fullfill the Bloch condition. While the Schrödinger equation for the isolated atom (one band, band index omitted) is

$$\left[-\frac{1}{2} \triangle + U(\boldsymbol{r}) \right] \phi(\boldsymbol{r}) = E^0 \phi(\boldsymbol{r}), \tag{1.11}$$

the solution of the whole crystal is assumed to be

$$\left[-\frac{1}{2} \triangle + V(\boldsymbol{r}) \right] \phi(\boldsymbol{r}) = E\phi(\boldsymbol{r}), \tag{1.12}$$

with the crystal potential denoted as $V(\boldsymbol{r})$. One now can evaluate the expectation value of the energy with respect to the basis functions 1.10 and express the result in terms of

(V-U), the deviation of the true crystal potential from the simple, combined atomic one. This yields

$$E = E^0 + \frac{1}{N} \sum_{\boldsymbol{R}=0, nn} e^{i\boldsymbol{k}\boldsymbol{R}} \int \phi^*(\boldsymbol{r} - \boldsymbol{R})(V(\boldsymbol{r}) - U(\boldsymbol{r}))\phi(\boldsymbol{r})\, d^3r. \qquad (1.13)$$

Since the atomic solutions (Wannier functions) are spatially localized, the summation over $\boldsymbol{R}$ extends usually only up to the nearest or next nearest neighborhood. This is the main advantage of the tight binding technique. The matrix of the Hamiltonian becomes larger the more atomic shells and neighbor-shells are included. The eigenvalues are simply determined by diagonalizing the Hamilton matrix, which has to be done separately for each $\boldsymbol{k}$ of interest. The summation in equ. 1.13 comprises two types of integrals, on-site integrals

$$-A = \int \phi^*(\boldsymbol{r})(V(\boldsymbol{r}) - U(\boldsymbol{r}))\phi(\boldsymbol{r})\, d^3r, \qquad (1.14)$$

and so-called "hopping" integrals

$$-B = \int \phi^*(\boldsymbol{r} - \boldsymbol{R})(V(\boldsymbol{r}) - U(\boldsymbol{r}))\phi(\boldsymbol{r})\, d^3r. \qquad (1.15)$$

While the former are a measure of the crystal field effect, reflecting the change in on-site energy due to the presence of neighboring atoms, the hopping integrals are proportional to the overlap of the wavefunctions centered on two different sites. While parameter A changes the energetic position of a band, parameter B determines the band-width. Large B means large overlap and broad bands. There are two reasons for the occurrance of a dispersionless band having B=0. Either the sites $(\boldsymbol{r} - \boldsymbol{R})$ and $(\boldsymbol{r})$ are too far apart for any interaction, or the corresponding wavefunctions are orthogonal. This means that symmetry arguments (the sign of the wave-function) lead to a cancellation of the integral even though there is charge overlap (e.g. one s and one p_z orbital shifted by (1,0,0)). One should be aware of the fact that while A contains one and two center integrals, B even contains three center integrals. In the latter, $\phi^*,(V - U)$, and ϕ are centered on three different sites. Three-center integrals are often neglected, also in the present work the Slater-Koster technique [1], a well-known two-center approximation, has been applied. Above integrals are usually not calculated but fitted to band-structure results obtained by more accurate but much slower methods. Once the matrix elements are parameterized, the method is very fast and if sufficiently many neighbors are included also surprisingly accurate.

1.5 The variational principle and Hartree-Fock theory

Both border-cases mentioned above neglected electron-electron interactions. Even though the empirical tight binding parameters can be adopted to yield good results even for com-

plex materials, the agreement is due to the fact that the tight binding parameters absorb the many body effects. This, however, is not very physical because it is desired to resolve as many contributions to the total energy as possible. The methods discussed from now on have the advantage that they exploit the extremely useful quantum mechanically variational principle. It says that if the Hamiltonian $\hat{H}$ of a system is known, the expectation value E^t of $\hat{H}$ using trial wavefunctions $|\Psi^t\rangle$ as basis is always larger or equal the energy of the true ground state E:

$$E \leq \langle \Psi^t | \hat{H} | \Psi^t \rangle \tag{1.16}$$

This opens the door to computer ab-initio methods. The only input parameters are the types of atoms involved and their position within the unit cell. The orbital occupation (Hartree Fock) or the charge density (Density functional theory, see later) is successively adopted until the minimal energy configuration is found.

One widely used technique to solve the many-body Schrödinger equation including electron-electron interactions explicitly is the Hartree-Fock (HF) self consistent field method. Even though the electron spin is not included from the beginning, HF theory is sophisticated enough for magnetism to occur. Starting point is the Hamiltonian 1.2. Since the correct wave-function has to be antisymmetric, a possible ansatz for a trial wave function would be

$$\Psi_{HF}(\boldsymbol{r}_1, \boldsymbol{r}_2, \cdots, \boldsymbol{r}_N) = \frac{1}{N!} \sum_s (-1)^s \prod_{i=1}^{N} \Phi_{s,i}(\boldsymbol{r}_i), \tag{1.17}$$

the sum runs over all possible $N!$ permutations s. The Φ typically are a set of localized wavefunctions such as Slater or Gaussian type orbitals. The antisymmetric form allows a formulation of the wave-function also as a so-called Slater determinant. In HF theory one asks for the best antisymmetric product wave-function (or Slater determinant) approximating the true N-particle ground state as that one which minimizes the expectation value of the Hamiltonian. In its simplest form (restricted HF technique) the Slater determinant of N electrons is built up from $N/2$ orbitals with 2 electrons each, being in a S=0 singulett configuration. This is necessary if both electrons are assumed to be in the same quantum state. The expectation value of the Hamiltonian becomes

$$E_{HF} = \langle \Psi_{HF} | \hat{H} | \Psi_{HF} \rangle = 2 \sum_{i=1}^{N/2} \langle i | \hat{h} | i \rangle + 2 \sum_{i,j=1}^{N/2} \langle ij | w | ij \rangle - \sum_{i,j=1}^{N/2} \langle ij | w | ji \rangle, \tag{1.18}$$

$\hat{h}$ consists of the kinetic energy and the potential energy of one electron in the external potential v_{ext}. Consequently the first term on the right hand side of equation 1.18 is an expectation value of a one-particle operator. The next two contributions in 1.18 are expectation values of the electron-electron interaction involving two particles, the first

one is called Hartree term, the second one exchange term. Explicitly writing out above abbreviations results in the following:

$$\langle ij| \, w \, |ij\rangle \;\; = \;\; \int d^3 r_i d^3 r_j \; \Phi_i^*(\boldsymbol{r}_i)\Phi_j^*(\boldsymbol{r}_j)\frac{1}{|\boldsymbol{r}_i - \boldsymbol{r}_j|}\Phi_i(\boldsymbol{r}_i)\Phi_j(\boldsymbol{r}_j)$$

$$\langle ij| \, w \, |ji\rangle \;\; = \;\; \int d^3 r_i d^3 r_j \; \Phi_i^*(\boldsymbol{r}_i)\Phi_j^*(\boldsymbol{r}_j)\frac{1}{|\boldsymbol{r}_i - \boldsymbol{r}_j|}\Phi_j(\boldsymbol{r}_i)\Phi_i(\boldsymbol{r}_j) \qquad (1.19)$$

While the Hartree term (first line) can be understood classically as the Coulomb interaction of the charge densities of two electrons, the exchange term (second line) is a pure quantum effect and as such can not be understood classically. It is the starting point for the discussion of magnetism. Even though HF theory starts initially without any explicit spin-dependent contribution to the Hamiltonian, the Pauli principle in combination with the indistinguishability of electrons leads to the exchange term, the so-called direct exchange between overlapping wavefunctions. It is responsible e.g. for the triplet ground state of the O_2 molecule. However, HF has two major drawbacks. First, it is computationally expensive because the expression for the exchange energy is non-local. This means that the exchange energy for one orbital depends on all the other orbitals. The second major problem is that HF in its original form does not include electron-electron correlations. These correlations are defined as the energy difference between the result of a single determinant HF calculation and the exact electronic energy determined e.g. via Quantum monte carlo techniques. Correlations have the effect that the electrons tend to avoid each others more than HF theory would predict and thus correlations reduce the energy of the system. They always play a role when electrons do not feel an average potential of all the other electrons in the neighborhood but a potential of electrons belonging to distinct orbitals (e.g. the same d/f orbital or a spatially localized bonding orbital). This neglect of correlation energy is the reason why single-determinant HF fails to describe metals. One prominent failure is the free electron gas which is predicted to have a vanishing density of states (DOS) at the Fermi energy. On the other side, HF gives good results for atoms and molecules, where screening is not so pronounced. In order to account for correlations in HF, further determinants, in which one orbital has been replaced by a corresponding excited state orbital, have to be used. The addition of further determinants increases the variational freedom and hence reduces the total energy of the system. This technique is called configuration interaction (CI) and belongs to so-called post-HF methods.

1.6 Density matrices and the Fermi-hole

While HF is a method designed for molecules and weakly screened materials, one of the most successful ways to calculate the electronic properties of metals is Density Functional

theory (DFT). The concept is based on the idea of describing as system mainly using its charge density as the fundamental quantity, instead of orbitals like in HF. This speeds up the calculation, because the charge density is a local quantity. Before DFT can be discussed, it is useful to start with Thomas-Fermi theory and density matrices. The reduced single particle density matrices related to a pure N-particle wave-function is defined as

$$\gamma_1(x; x') = N \int dx_2 \ldots dx_N \ \Psi(x, x_2, \ldots, x_N) \Psi^*(x', x_2, \ldots, x_N), \qquad (1.20)$$

where $x = (\boldsymbol{r}; s)$ combines space and spin coordinates [2]. For the spin-independent form one has to sum over the spin

$$\gamma_1(\boldsymbol{r}, \boldsymbol{r}') = \sum_s \gamma_1(\boldsymbol{r}, s; \boldsymbol{r}', s). \qquad (1.21)$$

The prefactor N ensures that the diagonal of $\gamma_1(\boldsymbol{r}, s; \boldsymbol{r}', s)$ with $\boldsymbol{r} = \boldsymbol{r}'$ equals the electron density $n(\boldsymbol{r})$. In analogy the (spin dependent) two-particle density matrix can be defined as

$$\gamma_2(x_1, x_2; x'_1, x'_2) = \frac{N(N-1)}{2!} \int dx_3 \ldots dx_N \ \Psi(x_1, x_2, x_3 \ldots, x_N) \Psi^*(x'_1, x'_2, x_3 \ldots, x_N). \qquad (1.22)$$

It is related to the the single-particle density via the relation

$$\gamma_1(x; x') = \frac{2}{N-1} \int dx_2 \ \gamma_2(x, x_2; x', x_2). \qquad (1.23)$$

The pair density $n_2(x_1, x_2)$ is the diagonal of the two-particle density matrix γ_2 and gives the probability density to find one particle at x_1 and another one at x_2. Within a fixed basis of single-particle spin-orbitals $\Phi_i(x)$ (like in HF) the Heisenberg representation of the one particle density matrix is

$$\langle i | \gamma_1 | j \rangle = \int dx dx' \ \Phi_i^\star(x) \gamma_1(x, x') \Phi_j(x'). \qquad (1.24)$$

Finally two different pair correlation functions can be defined,

$$g(\boldsymbol{r}_1, \boldsymbol{r}_2) = \frac{n_2(\boldsymbol{r}_1, \boldsymbol{r}_2)}{n(\boldsymbol{r}_1) n(\boldsymbol{r}_2)}, \quad h(\boldsymbol{r}_1, \boldsymbol{r}_1) = n_2(\boldsymbol{r}_1, \boldsymbol{r}_2) - n(\boldsymbol{r}_1) n(\boldsymbol{r}_2). \qquad (1.25)$$

Assuming that Ψ in equ. 1.20 and 1.22 is an anti-symmetrized product of plane waves (no interactions, only symmetry constraints), the pair correlation functions exhibit interesting properties. For large distances $|\boldsymbol{r}_1 - \boldsymbol{r}_2|$, g goes to unity and h goes to zero. This is the limit in which the electons do not "feel" each others any more and become independent.

The other limit, $g(\boldsymbol{r}_1 = \boldsymbol{r}_2) = 1/2$, reflects the Pauli exclusion principle which has been put into the symmetry constraint of the wave-function. If there is an electron at $\boldsymbol{r}_1$, no other electron with the same spin can be at $\boldsymbol{r}_2 = \boldsymbol{r}_1$. This so-called Fermi-hole in the pair correlation function $g(r = |\boldsymbol{r}_1 - \boldsymbol{r}_2|)$ takes the form

$$g(r) = 1 - \frac{9}{2}\left[\frac{\sin(k_f r) - k_f r\cos(k_f r)}{(k_f r)^3}\right]^2. \tag{1.26}$$

$g(r)$ increases from $1/2$ at $r = 0$ to 1, weakly oscillating when approaching the limit $g(r) \to 1$. Using above definitions the expectation values of quantum mechanical operators can conveniently be defined now. Expectation values of one particle operators such as the kinetic energy can be expressed by

$$\langle \hat{T} \rangle = -\frac{1}{2}\int d^3r\ [\triangle\gamma_1(\boldsymbol{r};\boldsymbol{r}'),]_{\boldsymbol{r}'=\boldsymbol{r}} \tag{1.27}$$

and those for two-particle Coulomb interactions such as $w(\boldsymbol{r}_i, \boldsymbol{r}_j)$ (1.2) yield

$$\langle \hat{w} \rangle = \frac{1}{2}\int d^3r d^3r'\ w(\boldsymbol{r}, \boldsymbol{r}')n_2(\boldsymbol{r}, \boldsymbol{r}'). \tag{1.28}$$

Since the Schrödinger equation consists only of one- and two- particle operators, the knowledge of γ_1 and n_2 suffices to calculate the total energy of a system as the expectation value of its Hamiltonian. The decomposition of 1.2 can now be performed:

$$\begin{aligned}
E = \langle \hat{H} \rangle &= -\frac{1}{2}\int d^3r\left[\triangle\gamma_1(\boldsymbol{r}, \boldsymbol{r}')\right]_{\boldsymbol{r}'=\boldsymbol{r}} + \\
&+ \int dx\ v_{ext}(x)n(x) + \\
&+ \frac{1}{2}\int d^3r d^3r'\ n(\boldsymbol{r}')w(|\boldsymbol{r}' - \boldsymbol{r}|)n(\boldsymbol{r}) + \\
&+ \frac{1}{2}\int d^3r d^3r'\ w(|\boldsymbol{r}' - \boldsymbol{r}|)h(\boldsymbol{r}', \boldsymbol{r}) = \\
&= E_{kin} + E_{pot} + E_H + E_{XC}.
\end{aligned} \tag{1.29}$$

The energy can be decomposed into the kinetic energy E_{kin}, the interaction energy with an external potential due to ionic cores or an applied external field E_{pot}, the classical Hartree energy E_H, and the exchange and correlation energy E_{XC}.

1.7 Density functional theory (DFT)

The first approach based completely on the density $n(\boldsymbol{r})$ and not on either two-particle density matrices or orbitals was Thomas-Fermi theory [3, 4]. In that approximation exchange interactions were neglected. Since the kinetic energy is the only contribution that

is not explicitly expressed in terms of the electron density (see equ. 1.29), Thomas and Fermi approximated ϵ_{kin} of the interacting system through an expression valid for the homogeneous, interaction-free Fermi-gas:

$$\epsilon_{kin} = C_F \, n(\boldsymbol{r})^{2/3} \text{ with } C_F = \frac{3}{10}(3\pi^2)^{2/3} \approx 2.8712 \tag{1.30}$$

$$E_{kin} \approx \int d^3r \, n(\boldsymbol{r})\epsilon_{kin}(\boldsymbol{r}) = C_F \int d^3r \, n^{5/3}(\boldsymbol{r}) \tag{1.31}$$

This simplification, however, turned out to be the reason why Thomas-Fermi theory is neither able to describe the shell structure of atoms nor negatively charged ions at all. The breakthrough in finding a suitable parameterization for the energy as a functional of electron density was Density functional theory (DFT)[5]. It is based on two theorems of Hohenberg and Kohn [6]. The first HK theorem states that the external potential v_{ext} is apart from a trivial constant uniquely determined by the electron density $n(\boldsymbol{r})$. The use of this is to transform every functional dependence on v_{ext} into a functional dependence on $n(\boldsymbol{r})$ via $v_{ext}[n(\boldsymbol{r})]$. The first HK theorem allows to define a "universal" functional not depending on the external potential and hence not on any particular material-specific quantity:

$$E[n] = T[n] + v_{ext}[n] + w[n] = F_{HK}[n] + \int n(\boldsymbol{r})v_{ext}(\boldsymbol{r})d^3r \tag{1.32}$$

The second HK theorem proves that trial densities $n(\boldsymbol{r})$, if they are correctly normalized to the total number N of electrons, $N = \int n(\boldsymbol{r})d^3r$, always yield energies E_{trial} higher or equal to that determined via the true ground state density $n_0(\boldsymbol{r})$:

$$E_0 \leq E_{trial}[n]. \tag{1.33}$$

The HK theorems open the door to new techniques in solving the many-body Hamiltonian. By exploiting the one to one correspondence between the electron density $n(\boldsymbol{r})$ and the many-body wave-function $\Psi(x_1, x_2, \ldots, x_n)$ of groundstates (via the potential, HK-1), one tries to express the ground state energy E_0 through the ground-state density $n_0(\boldsymbol{r})$ instead of using the two particle density matrix. Even though the Hohenberg Kohn theorems give no information of how the energy functional $E[n(\boldsymbol{r})]$ can be approximated, the theorems prove its existence and its variational character.

Kohn and Sham suggested to decompose the HK functional F_{HK} as follows:

$$F_{HK}[n] = T[n] + E_H[n] + E_{XC}[n]. \tag{1.34}$$

Their great idea was to map the real system onto a hypothetical system of non-interacting electrons having a kinetic energy $T[n]$ of non-interacting electrons. $E_H[n]$ is the Hartree energy as introduced in 1.29 and E_{XC} is now defined as the exchange and correlation energy

plus the interaction-part of the kinetic energy. This quantity will be referred to as (Kohn-Sham) exchange-correlation energy E_{XC} in the following. Assuming the density $n(\boldsymbol{r}) = \sum_{i=1}^{N} \phi_i^\star(x)\phi_i(x)$ of a determinantal state $\Psi_0(x_1,\ldots,x_N) = \frac{1}{\sqrt{N}}\det||\phi_i(x_k)||$, $\langle\phi_i|\phi_j\rangle = \delta_{ij}$ the Kohn-Sham (KS) equations are given as

$$\left(-\frac{1}{2}\triangle + v_{eff}(x)\right)\phi_i(x) = \phi_i(x)\epsilon_i, \quad v_{eff} = v_{ext} + v_H + v_{XC}. \tag{1.35}$$

The Kohn-Sham exchange correlation potential v_{XC} is defined as

$$v_{XC} = \frac{\delta E_{XC}}{\delta n(x)}. \tag{1.36}$$

Equation 1.35 is a single-particle equation with the external potential v_{ext} replaced by the effective potential v_{eff}. The latter depends on the KS orbitals ϕ_i so that the problem must be solved iteratively (self-consistently) similar to the HF equations. The whole success of DFT now depends on the quality of the exchange-correlation energy E_{XC}. It is a functional of the electron density and a priori unknown. It can easily be generalized to the spin-polarized case if the spin density matrix is diagonal, meaning that spin-up and spin-down bands do not mix. One of the oldest but still very successful approximation is the local density approximation (LDA). The exchange-correlation energy is assumed to be a local function and not a functional of the electron density $n(\boldsymbol{r})$. E_{XC} is obtained by integrating the density $n(\boldsymbol{r})$ over the whole system, weighted locally with ϵ_{xc}, the exchange correlation energy of a interacting, homogeneous electron gas having the same electron density as the real system.

$$E_{XC}^{LDA} = \int n(\boldsymbol{r})\epsilon_{xc}(n(\boldsymbol{r}))d^3r. \tag{1.37}$$

The exchange-correlation energy for the free electron gas, ϵ_{xc}, consists of an exchange part ϵ_x that can exactly be determined from Hartree-Fock

$$\epsilon_x = -3\left(\frac{3}{4\pi}\right)^{1/3}\frac{1}{n}(n_\uparrow^{4/3} + n_\downarrow^{4/3}), \tag{1.38}$$

and the correlation part ϵ_c that can be determined only numerically, although to a rather high accuracy. The LDA is exact in the limit of slowly-varying and high electron densities. In real systems LDA tends to overbind materials, meaning that lattice constants are underestimated and Bulk moduli are overestimated. The sizes of the magnetic moments in weak, itinerant ferromagnets calculated at the equilibrium lattice constant usually are underestimated within LDA. One historically important case is Fe, which comes out fcc

and non-magnetic in LDA instead of bcc and ferromagnetic. This led to several corrections of LDA, most important is the generalized gradient approximation (GGA).

$$E_{XC}^{GGA} = \int f(n_\uparrow, n_\downarrow, \bigtriangledown n_\uparrow, \bigtriangledown n_\downarrow) d^3r. \tag{1.39}$$

GGA is better suited for 3d transition metals, however, in general one should compare both approximations and rely on that one being in better agreement with experiment.

The gain of above simplifications is enormous. Instead of a non-local exchange operator like in HF theory one can now express the total energy of the system as a local (or semi-local in the case of GGA) function of its density. Moreover, DFT allows to take into account correlations that are not present within single-determinant HF techniques. This is because one can approximate ϵ_{xc} for the interacting, free electron gas much better than plain HF is able to. A plausible reason for the success of the local character of DFT is screening. Even though the Coulomb interaction reaches to infinity, the electron is screened by a surrounding electron cloud. The effective potential v_{TF} can be expressed e.g. through the Thomas Fermi screening length $\lambda_{TF} = (\pi/12)^{1/3}r_s^{1/2}$ with $4\pi r_s^3/3$ being the average volume per atom:

$$v_{TF} = -\frac{2Z}{r}e^{-r/\lambda_{TF}}. \tag{1.40}$$

This potential is much-less far-reaching than the bare Coulomb potential.

One drawback of DFT in particular for non-metallic systems is that the KS orbitals ϕ_i as well as the energy eigenvalues not necessarily have a physical meaning. The energy eigenvalues are not quasi-particle energies in the sense of many-body perturbation theory. As mentioned above LDA is exact for either slowly varying densities or high densities. In the language of many-body theory DFT is an approximation for the self energy Σ like

$$\epsilon(\boldsymbol{k}) = \boldsymbol{k}^2 + \Sigma(k_F, E(k)), \tag{1.41}$$

being accurate if the variations of Σ with respect to $\boldsymbol{k}$ and the energy are small [7]. This is equivalent to postulating that the effective mass of the quasi-particles $m^\star$ should not be much enhanced compared to m because $m^\star/m$ can be written as

$$\frac{m^\star}{m} = \frac{1 - \frac{\partial \Sigma(\boldsymbol{k},\omega)}{\partial \omega}}{1 + \frac{m}{k_F}\frac{\partial \Sigma(\boldsymbol{k},\omega)}{\partial \boldsymbol{k}}}. \tag{1.42}$$

However, one has to distinguish between the quality of DFT eigenvalues (e.g. the band-gap) and the quality of DFT total energies [8]. It is well-known that the total energies, determining e.g. lattice constants or the Bulk moduli, are in very good agreement with experiment also for semiconductors, insulators and materials with more localized and "correlated" electrons. Moreover, one usually is not too far off when interpreting the calculated

eigenvalues as excitation energies. The energy gaps of semiconductors and insulators calculated within DFT typically come out too small by about 40%.

There are several approaches trying to improve upon DFT in the case of strong electron localization and hence strong variations of the electron density. One of the most natural ways to address this problem is the self-interaction-correction (SIC) [9]. While HF-theory is self-interaction free because direct and exchange Coulomb interaction exactly cancel each others, in LDA and GGA the self-interaction is only partially canceled. The error is the larger the more localized the orbitals become. A similar approach trying to improve the description of localized orbitals is LDA+U [10]. The technique exploits the fact that HF is better suited for the description of the so-called atomic limit [11] and a penalty functional is introduced that energetically disfavors non-integer occupations of certain, localized orbitals. Typically the parameter U is situated between 2eV and 8 eV. Within so-called constrained LDA [12] U can in principle be determined through the energy necessary to change the orbital occupation while at the same time isolating the orbital of interest from the environment. By construction U is not variational and can not be determined by minimizing the total energy w.r.t. U. In order to improve the band-gap for semiconductors a rather successful technique is to mix the DFT exchange-correlation energy with a small portion (usually 1/3) of exact Hartree-Fock exchange [13]. These functionals are called hybrid functionals (e.g. B3LYP). A completely different way to improve upon the gap in semiconductors is to explicitly calculate the single partice Green's function and the self energy Σ within the RPA approximation (L. Hedin, [14]). Even though this approach is very time-consuming it seems to yield very good results for quasiparticle energies (e.g. [15]), provided that very high-lying, unoccupied states are treated with high accuracy.

1.8 Computational approaches

Most computational approaches expand charge density and potential in a suitable set of functions $\phi_j(\boldsymbol{r})$. Suitable means physically motivated, e.g. plane waves for slowly varying potentials and localized functions for atomic-like potentials. In a general form the Bloch wave $\Psi_{\boldsymbol{k}}(\boldsymbol{r})$ can be written as

$$\Psi_{\boldsymbol{k}}(\boldsymbol{r}) = \sum_j a_j(\boldsymbol{k})\phi_j(\boldsymbol{r}). \tag{1.43}$$

The expansion coefficients $a_j(\boldsymbol{k})$ are obtained in a variational procedure leading to the secular equation:

$$\sum_j \left[\int \phi_i^\star(\boldsymbol{r})H\phi_j(\boldsymbol{r})d^3r - \epsilon_k \int \phi_i^\star(\boldsymbol{r})\phi_j(\boldsymbol{r})d^3r \right] a_j(\boldsymbol{k}) = 0 \tag{1.44}$$

H denotes the KS single-particle Hamiltonian. The solutions are found by setting the determinant (in [ ] brackets) to zero and finding the roots. In the computer this is done in diagonalizing a (huge) matrix. If the functions $\phi_i(\boldsymbol{r})$ do not depend on the eigenvalues ϵ_k, one faces a linear eigenvalue problem and the corresponding method is called linearized method [16]. Most approaches divide the real space unit cell into two regions, the core or also called muffin tin (MT) regions around the atomic sites and the rest of the unit cell, the interstitial (IS). The reason is that plane waves describe the interstitial well but their strong oscillations close to the nuclei require the inclusion of a huge number of plane waves up to very high energies. On the other hand, local basis sets slowly converge for e.g. far-reaching s- or p-states.

In the Augmented Plane Wave (APW) method the basis functions are twofold: Plane waves are used in the interstitial and spherical harmonics Y_{lm} inside the MT-spheres:

$$\text{IS:} \qquad \Psi(\mathbf{r}) = \sum_{\mathbf{G}_i} e^{i(\boldsymbol{k}+\mathbf{G}_i)\cdot\mathbf{r}}, \tag{1.45}$$

$$\text{MTs:} \qquad \Psi(\mathbf{r}) = \sum_{lm} A_{lm} R_l(r)\, Y_{lm}(\theta,\phi), $$

The functions $R_{lm}(r)$ are solutions of the radial Schrödinger equation with energy E regular at the origin but usually not vanishing (because continued) for $r \to \infty$:

$$-\frac{1}{2r^2}\frac{d}{dr}\left[r^2\frac{dR_l(r)}{dr}\right] + \left[\frac{l(l+1)}{2r^2} + V(r)\right] R_l(r) = E R_l(r). \tag{1.46}$$

The expansion coefficients A_{lm} are found by matching the solutions inside the MTs to the plane waves outside, yielding the necessary boundary condition for the solutions of the radial equation. The APW method is not a linear method because the basis set is energy dependent through the radial equation. Within the domain of LDA, the APW method can be made arbitrarily exact. The price to pay is its computational effort. For this purpose the APW method has been linearized. In the **L**APW method the energy in equ. 1.46 enters as a parameter E_p that is fixed at the approximate band center. The basis set becomes energy-independent, but one has to include a correction term including the derivative of the radial function with respect to the energy $\dot{R}_l(r)$:

$$R_l(r, E) = R_l(r, E_p) + (E - E_p)\dot{R}_l(r, E_p). \tag{1.47}$$

The solutions inside the MTs are now given as

$$\Psi(\mathbf{r}) = \sum_{lm} \left[A_{lm} R_l(r, E_p) + B_{lm}\dot{R}_l(r, E_p)\right] Y_{lm}(\theta,\phi), \tag{1.48}$$

The MT wavefunctions have to match continuously in value and first derivative to the plain waves outside. This allows to determine the coefficients B_{lm}. The LAPW method is usually a very good approximation to the APW one, only in the case energies far from the linearization energy are considered it can differ significantly from the APW. This problem can be circumvented by including several energy windows for one and the same l quantum number. Regarding the potential several levels of sophistication exist. In the (oldest) muffin-tin approximation the series expansion of the potential is truncated early: The potential is assumed to be constant in the IS and spherical symmetric within the MTs. Nowadays full-potential approaches are used (**FLAPW**, [17, 18]) imposing no shape restriction on the potential. In principle one could expand it up to arbitrary high partial waves l. Usually l=8 is enough, only in cases of high crystal symmetry the series should be truncated later because the first correction terms are already those for l=8.

An alternative to the (all-electron) FLAPW method is the pseudopotential method using exclusively plane waves as basis set. This can only be done efficiently if the core potential has been substituted by a softer "pseudo-potential", calculated from the constraint that the resulting valence-electron wave-function $\Psi^{pseudo}(\boldsymbol{r})$ must agree with the exact one $\Psi^{exact}(\boldsymbol{r})$ outside a core radius r_{core}. There exist several types of implementations. Norm-conserving pseudopotentials must accumulate the same valence electron charge inside r_{core} as the exact potential does, ultra-soft pseudopotentials relax this condition and allow for larger core radii r_{core} and fewer plane-waves. The PAW (projector-augmented wave) technique is the most elegant one. It combines the augmentation concept of the all-electron methods with the plane wave formalism ([19, 20, 21]). During the generation of PAW-potentials additionally so-called projectors are stored. These projectors are only defined inside r_{core}, the augmentation region, and are used during the solid-state calculation to restore the correct l partial waves and hence the correct all-electron wave-function inside of r_{core}. As a consequence, not only the error introduced by the neglect of norm-conservation is eliminated, also the restoration of the correct form of the wave-function in the augmentation region via a radial grid make the PAW method equivalent to all-electron methods.

Chapter 2

Magnetism

2.1 The origin of magnetism

In classical electrodynamics the sources of magnetic fields are either time-dependent electrical fields $\boldsymbol{E}$ or currents $\boldsymbol{I}$. If an electrical current flows through a straight wire running along the z-axis from $-\infty$ to ∞, a magnetic field $\boldsymbol{H}$ given by

$$\boldsymbol{H} = \frac{\mu_0}{2\pi} \frac{I}{r} \, \hat{e}_\phi \ \text{(SI units)} \tag{2.1}$$

is created. This $\boldsymbol{H}$-field depends only on the radial distance to the wire $r = (x^2 + y^2)^{1/2}$. The constant μ_0 is the permeability of vacuum ($\mu_0 = 4\pi 10^{-7} \ \text{N/A}^2$) and $\boldsymbol{H}$ has the dimension N/(Am)=Vs/m^2=1 Tesla (T). If the region inside a material is considered, the quantity $\boldsymbol{H}$ must be substituted by the more physical magnetic induction $\boldsymbol{B}$. Only in vacuum both quantities are equivalent (up to a factor), in matter $\boldsymbol{B}$ additionally includes the magnetization of the material, $\boldsymbol{M}$:

$$\boldsymbol{B} = \mu_0(\boldsymbol{H} + \boldsymbol{M}) \ \text{(SI units)}, \tag{2.2}$$

The magnetization is also defined as the derivative of the free energy F with respect to the external field $\boldsymbol{H}$:

$$\boldsymbol{M} = -\frac{\partial F}{\partial \boldsymbol{H}}. \tag{2.3}$$

In the limit of weak external fields the strength of the material's response to an applied field $\boldsymbol{H}$ is usually characterized by the magnetic susceptibility χ:

$$\chi = \frac{\boldsymbol{M}}{\boldsymbol{H}}. \tag{2.4}$$

In its most general form χ is a tensor because both, $\boldsymbol{H}$ and $\boldsymbol{M}$, are vectors. However,

this will be neglected and $\boldsymbol{M}$ is assumed to be either parallel (χ positive) or antiparallel (χ negative) to the applied field. It is further assumed that the probing magnetic field is constant in space and time, which is equivalent to neglecting the wavevector- $\boldsymbol{q}$ and frequency- ω dependence of $\chi = \chi(\boldsymbol{q}, \omega)$.

Even though the origin of magnetism can somehow be understood classically, magnetism can be fully understood only if quantum mechanics is applied. This has first been pointed out by van Leeuwen, who showed that the classical partition function Z_c is independent of the applied magnetic field $\boldsymbol{H}$. This makes a finite magnetization $\boldsymbol{M} = -(\partial F)/(\partial \boldsymbol{H})$ with the free energy $F = -k_B T \ln Z_c$ classically impossible, even in the presence of an external magnetic field.

2.2 The atomic limit

In the simplest case of the isolated hydrogen atom the single electron is subject to a potential having full rotational symmetry. The electron's orbital quantum number $\boldsymbol{L}$ is conserved and quantized in units of $\hbar$. It is hence plausible that also the magnetic moment $\boldsymbol{\mu}$ caused by its orbital motion is quantized. The proportionality between the orbital magnetic moment $\boldsymbol{\mu}$ and the angular orbital moment $\boldsymbol{L}$ can be determined classically via the current of the "orbiting" electron and its resulting magnetic moment. It is given as

$$\boldsymbol{\mu} = g_L \mu_B \boldsymbol{L}. \tag{2.5}$$

The gyromagnetic ratio g_L for orbital motion is -1, the quantity

$$\mu_B = \frac{e\hbar}{2m_e c} \text{ (SI)} = \frac{1}{2c} \text{ (a.u.)} = 5.78838 \ 10^{-5} \text{eV/T} \tag{2.6}$$

is the so-called Bohr magneton, the smallest possible unit of magnetization. This, however, is not the full story. When solving the Dirac equation one finds that the electron additionally has an intrinsic angular moment with $\hbar/2$ quantization, the electron spin $\boldsymbol{S}$. This is the second source of magnetism. In contrast to orbital motion the spin $\boldsymbol{S}$ has an "anomalous" gyromagnetic ratio g_S of roughly -2. The change in the Hamiltonian ΔH for an isolated atom due to the presence of an external magnetic field $\boldsymbol{H}_{ext}$ (assuming transverse gauge (div $\boldsymbol{A}$=0) and a homogeneous magnetic field $\boldsymbol{H}_{ext}$ pointing in the z-direction) is given (in SI) as [22]:

$$\Delta H = \mu_B (\boldsymbol{L} + 2\boldsymbol{S}) \boldsymbol{H}_{ext} + \frac{e^2}{8m_e c^2} \sum_i (x_i^2 + y_i^2). \tag{2.7}$$

The prefactor 2 for $\boldsymbol{S}$ is again the gyromagnetic ratio of the spin. The first term is the Zeeman term. It is the source of paramagnetism (positive χ). The second contribution

is the origin of diamagnetism, giving rise to a small but negative susceptibility χ. The summation runs over all electrons. The quantity $(x_i^2 + y_i^2)$ is related to the average distance between the electrons and the nucleus. This contribution is the classical analog of Lenz' rule. The $\boldsymbol{H}$ field slightly changes the electron's orbital motion, similar to a field that via induction reduces the current that generated it. Due to the smallness of the Bohr magneton μ_B and the term $e^2/(8mc^2)$ the field induced energy shifts ΔE_n are small. Second order perturbation theory yields (SI)

$$\Delta E_n = \mu_B \boldsymbol{H} \langle n| \boldsymbol{L} + 2\boldsymbol{S}|n\rangle + \frac{e^2}{8m_e c^2} H^2 \langle n| \sum_i (x_i^2 + y_i^2)|n\rangle + \sum_{n' \neq n} \frac{|\langle n|\mu_B \boldsymbol{H}(\boldsymbol{L} + 2\boldsymbol{S})|n'\rangle|^2}{E_n - E_{n'}}.$$

(2.8)

The most important contribution is the Zeeman term because it is linear in H, however, it is only present if the electron shell has a non-vanishing $\boldsymbol{L}$ or $\boldsymbol{S}$. The diamagnetic contribution is always present but very weak. The third term is the Van Vleck contribution. It involves excited states and thus can give rise to a weak response χ in the case the ground-state is non-magnetic and the first excited state is thermally accessible.

The crucial question now is how to add the spins $\boldsymbol{S}_i$ and the orbital momenta $\boldsymbol{L}_i$ of the individual electrons for a many-electron atom. In order to answer this it is useful to discuss the relativistic corrections arising from the solution of the Dirac equation. With exception of the electron spin $\boldsymbol{S}$ three further corrections can be identified. Most easy to understand is the relativistic mass-enhancement due to the electron's velocity. Instead of the constant electron mass m_e a relativistic, velocity-dependent mass M_{rel} appears: $M_{rel} = m_e + \epsilon - m_e c^2 - v_{ext}/(2c^2)$. Moreover, two terms without non-relativistic counterparts show up: The Darwin term, proportional to $dV/dr \, dg/dr$, $g(\boldsymbol{r})$ denoting the radial wavefunction, and the spin-orbit or also called LS coupling, being proportional to $1/r \, dV/dr \, \boldsymbol{L} \cdot \boldsymbol{S}$. If the LS coupling is weak, the quantum numbers $\boldsymbol{L}$ and $\boldsymbol{S}$ can in good approximation be considered as conserved. If the LS-coupling is added to the (non-relativistic) Schrödinger equation as a perturbation, it is the only term that couples the spin $\boldsymbol{S}$ to the lattice. Hence the LS-term is responsible for the magnetocrystalline anisotropy. For light atoms with weak spin-orbit coupling the appropriate coupling is thus the Russel Saunders coupling. $\boldsymbol{L}_i$ and $\boldsymbol{S}_i$ are first added up to yield a resulting $\boldsymbol{L}$ and $\boldsymbol{S}$ and then combined to a total angular moment $\boldsymbol{J}$. The ground-sates of an isolated atom is given by the three Hund rules. The ground state ...

1. has the largest value of the total spin $\boldsymbol{S}$.

2. has the largest value of the total orbital angular momentum $\boldsymbol{L}$ permitted by the first rule.

3. The total angular moment is $J=\mid \boldsymbol{L}-\boldsymbol{S} \mid$ for less than half filled shells, and $J=\mid \boldsymbol{L}+\boldsymbol{S} \mid$ for more than half filled shells.

The first Hund rule is the strongest restriction. Its origin is exchange, favoring electrons that avoid each others as much as possible. This is easiest if they have like-spin because then the Pauli principle automatically excludes double occupations of an orbital. The second Hund rule is already a weaker restriction. Using a strongly simplified classical analog one could say that in a state with maximum total $\boldsymbol{L}$ the electrons orbit in the same sense around the nucleus thus avoiding each others best. The third rule is a consequence of spin-orbit coupling. Since it comes from a relativistic effect it is the weakest rule. The most important consequence of the Hund rules is that an isolated atoms has a permanent magnetic moment if it has incompletely filled shells. Assuming that a solid is built from non-interacting atoms, above equations explain both, diamagnetic behavior if the highest-lying electronic shell is completely filled (Ar,Ne etc.), and paramagnetic behavior if $\boldsymbol{S}$ or $\boldsymbol{L}$ (or both) do not vanish. In that case the paramagnetic contribution is by orders of magnitude larger than the diamagnetic one.

2.3 Mean field approaches

In analogy to the two simple limits in electronic structure theory, tightly bound and almost free electrons, also in the field of magnetism two border-cases have developed historically (see e.g. [23]). The Stoner theory was originally developed for parabolic bands, so to say for free or "itinerant" electrons. On the other hand the Hubbard and the Heisenberg model assume perfect localization of the magnetic moments on lattice sites. The Hund rules are only valid for the isolated (or weakly interacting) atom. They always predict a local magnetic moment if a shell is partially filled. In the localized picture it is a matter of interactions whether the solid exhibits long-range order and if so, which type of magnetic order is favored. The important assumption in the localized regime is that the size of the (local) moments is independent of temperature and type of magnetic order. The macroscopic magnetization, averaged over all atoms, in the case of a ferromagnet is reduced only by thermal fluctuations. Above a critical temperature T_c the material is then called paramagnetic and exhibits no spontaneous, macroscopic magnetization any more. In a band-structure picture one speaks about a local moment if the bands-width W of the state responsible for magnetism is smaller that the exchange splitting, separating the spin-up band from its corresponding spin-down counterpart. In the itinerant picture one is in the domain of band electrons (Bloch electrons). They spread over the whole solid and thus the question whether magnetism arises or not is closely related to the type of
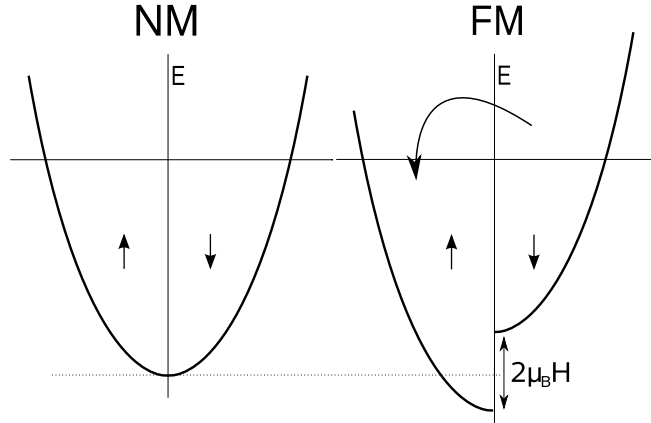
Figure 2.1: Stoner Theory: In the non-magnetic state spin-up and spin-down electrons are degenerate. If an external field H (or mean field H_M) is present, the bands shift by $\mu_B H$ up/down. While field energy is gained the redistribution of spin-down states into the spin-up band costs kinetic energy. This is because the spin-up electrons occupy the band up to higher energies than before the redistribution. In the case the density of states at E_F is high, the cost in kinetic energy is small and the spin-split states is energetically favored.

order being favored. If for a particular type of order the density of states exceeds a certain limit (the Stoner criterion), magnetic moments as well as long-range order set in. Upon raising the temperature, the size of the moments decreases. Ideal, itinerant magnets have no magnetic moments above the Curie temperature. This is in complete contrast to local systems having disordered moments above T_c. Itinerant magnets exhibit broad bands and small spin-splitting, so that spin-up and spin-down parts of one band overlap strongly.

Unfortunately, the vast majority of magnetic materials including such wide-spread cases like Fe or Ni lies inbetween these border-cases. Their magnetic moments change slightly with temperature but do not completely vanish above the ordering temperature. In DFT calculations the ordered magnetic and the non-magnetic state are easily accessible. The paramagnetic state requires the inclusion of disorder and is usually treated in the disordered local moment approach (DLM) [24] within the coherent potential approximation [25]. In the present work only the non-magnetic states as well as certain, ordered magnetic configurations are taken into account. When the atoms come close to form the solid interactions between the electrons set in. In the section about HF-theory direct exchange was introduced. This interaction is of Coulomb-type and much stronger than for example classical dipole-dipole interactions between local atomic moments. However, when the first models explaining spontaneous magnetization appeared (e.g. Weiss, Stoner), direct exchange was unknown. For this reason in many models very strong, phenomenological

"molecular fields" were introduced in order to explain spontaneous magnetization. These molecular fields H_M were treated on the same footing as external fields H_{ext} with the only difference that the former were considered as intrinsic material properties being at best temperature dependent. These molecular fields turned out to be unrealistically large and it took some time until it was recognized that it is not really a magnetic field that aligns the moments but rather an interaction of Coulomb type.

In the following paragraph the most important results of well-known mean-field approaches for both, the local moments and the itinerant moments, are listed. Since all directions are either parallel or anti-parallel to the quantization axis (z-axis), no vector notation is used. In the **Weiss** model the local moments are assumed to interact only via the mean-field H_M, given as

$$H_M = NM, \tag{2.9}$$

N is the molecular field constant relating the magnetization M with H_M. The magnetic moment of a particle with total angular momentum quantum number J and projection m_J in the quantization direction is given as

$$\mu = m_J g_J \mu_B, \text{ for } -J \leq m_j \leq +J, \tag{2.10}$$

g_J denotes the gyromagnetic ratio. The energy in a field H (external or mean field) is $W = -m_j g_J \mu_B H$ and the thermal energy is $k_B T$. By assuming independent, localized magnetic moments and by using Boltzmann statistics, the statistical average of the magnetization M normalized to the saturation magnetization M_0 (all moments having $m_J = -J$) is known as the Brillouin function $B(a, J)$:

$$\frac{M}{M_0} = B(a, J) = \frac{2J+1}{2J}\coth\left(a\frac{2J+1}{2J}\right) - \frac{1}{2J}\coth\left(\frac{a}{2J}\right), \tag{2.11}$$

The quantity a denotes the ratio between maximum magnetic and maximum thermal energy, $a = (J g_j \mu_B H)/(k_B T)$. In the presence of a mean-field H_M a phase transition to a ferromagnetic state occurs at the critical temperature T_c and spontaneous magnetic order sets in. The high temperature limit of the Brillouin function gives the well-known Curie-Weiss law, the 1/T dependency of the susceptibility χ above T_c:

$$\chi = \frac{C}{T - \theta} \text{ with the Curie constant } C = \frac{J(J+1)g_J^2\mu_B^2}{3k_B}, \tag{2.12}$$

In above expression θ is the paramagnetic Curie temperature. It can be estimated from the high temperature behavior of the susceptibility. Negative θ is an indication of antiferromagnetic order, positive θ usually is found in ferromagnets. In the latter case θ is usually close to the ferromagnetic Curie temperature at which spontaneous long-range order sets

in. The quantity $\sqrt{J(J+1)}g_J\mu_B$ is called effective moment. It can easily be obtained from experiment by fitting the Curie-Weiss law well above T_c.

In the **Stoner model** for itinerant electrons at T=0 one again introduces a molecular field H_M and a constant N connecting it with the relative magnetization ζ:

$$H_M = NM = NM_0\zeta, \text{ with } \zeta = \frac{M}{M_0}. \tag{2.13}$$

The electrons are considered as non-interacting, all interaction is absorbed in the molecular field. The density of states $N(E)$ for free electrons are parabolas. For Bloch waves only $\boldsymbol{k}$ and the spin S are assumed to be good quantum numbers and hence the magnetic field is assumed to couple only to the electron spin. This leads to a splitting into two spin-bands, spin up and spin down. The corresponding parabola are shifted against each others and the total magnetization, defined as the difference between the number of spin up (n^+) and spin down electrons (n^-), is different from zero. The energy shift due to the molecular field is given by

$$\epsilon_m = -\mu_B H_M = -\mu_B NM_0\zeta = -k_B\theta\zeta, \tag{2.14}$$

$\theta = (\mu_B NM_0)/k_B$ defines a characteristic temperature. The redistribution of initially $n = n^+ + n^- = 2\int_0^{E_F} N(\epsilon)d\epsilon$ spin-degenerate electrons from the spin-down to the spin-up channel costs kinetic energy (see fig. 2.1). This is because the Pauli exclusion principle forbids double-occupations of one state and higher energy states have to be populated. On the other hand the spin-polarization gives a negative energy contribution due to the (Zeeman-like) interaction with the external (or mean-) field. For parabolic bands the total energy as a function of ζ has two contributions, the positive, kinetic energy cost due to filling the spin-up band and the negative energy gain due to the interaction with the mean-field:

$$E = E_b + E_m = E(\zeta) = \frac{3}{10}nE_F\left[(1+\zeta)^{5/3} + (1-\zeta)^{5/3}\right] - \frac{1}{2}nk_B\theta\zeta^2 + \text{const.} \tag{2.15}$$

The higher the DOS at E_F ($N(E_F)$), the easier is the redistribution of spin-down to spin-up states and the more likely ferromagnetism occurs. Thus one can formulate a criterion yielding the instability (or tendency) towards the onset of ferromagnetism. This is the Stoner criterion:

$$2N^{\uparrow}(E_F)I \geq 1, \tag{2.16}$$

$N^{\uparrow}(E_F)$ denotes the density of states at E_F in the non-magnetic state for one spin direction ($N^{\uparrow}(E_F) = N^{\downarrow}(E_F) = N(E_F)/2$). The Stoner I changes only slowly throughout the periodic table and as a quasi-atomic property it is rather insensitive to the chemical environment [23]. Unfortunately, there appear two definitions of I in literature differing by a factor of two, depending on the initial contribution of I to the Landau expansion

of the total energy. In the present work I is assumed to contribute $E = -IM^2/2$ to the total energy. A generalization of equ. 2.16 for antiferromagnetism is given in a later section. Another important effect is observed if $N(E_F)$ increases and reaches the Stoner criterion from below. The electron-electron interaction leads to an enhancement of the temperature-independent, bare Pauli susceptibility χ_P by a factor of S:

$$\chi = \frac{2\mu_B^2 N^\uparrow(E_F)}{1 - 2\mu_B^2 I N^\uparrow(E_F)} = \frac{\chi_P}{1 - 2\mu_B^2 I N^\uparrow(E_F)} = \chi_P S. \tag{2.17}$$

$N^\uparrow$ always denotes the DOS at E_F taken from the non-magnetic calculation but given per spin channel. A non-magnetic metal with a strongly enhanced, magnetic susceptibility (e.g. Pd) is thus close to a magnetic transition. The value of I can be calculated using DFT by fitting the total energy versus the total magnetic moment. This is called fixed spin moment (FSM) method [23] and will be applied in a later section in order to probe a material's proximity to magnetism

2.4 From energy differences to effective Hamiltonians

One very successful technique to study the finite temperature behavior of a magnetic system is to map the results of ab-initio calculations on effective Hamiltonians. This generates a model system containing only the most relevant degrees of freedom. The model system can then be studied e.g. in a Monte-Carlo simulation and thermal properties such as the Curie temperature T_c can be determined. Very often the Heisenberg Hamiltonian is used [26]:

$$H = -\frac{1}{2}\sum_{i\neq j} J_{ij}\boldsymbol{S}_i\boldsymbol{S}_j - \sum_i k[\boldsymbol{S}_i]^2, \tag{2.18}$$

k denotes the single-ion anisotropy. It is large if changes in the size of the moment S_i are energetically expensive. In the case of semiconductors the anisotropy is assumed to be large enough so that in a good approximation the moments can be considered constant in size. The remaining part contains the exchange constants J_{ij}, functions of the distance $|\,\boldsymbol{r}_i - \boldsymbol{r}_j\,|$ and proportional to the energy required to change the angle between two spins $\boldsymbol{S}_i$ and $\boldsymbol{S}_j$ at sites i and j. Positive J_{ij} results in FM whereas negative J_{ij} cause AFM order. In principle there are two ways to determine the exchange constants J_{ij} within DFT [27]. One technique exploits the force theorem and calculates J_{ij} by infinitesimal rotations of single spins and pairs of spins away from their ground-state configuration [28]. This is appropriate for metals where the J_{ij} in general depend on the magnetic configuration. Thus small deviations from the ground state can be expected to give the best agreement, in particular at low temperatures. In the second technique one has to set up a supercell and compare

the total energies between the FM and certain AFM, collinear magnetic configurations for pairs of spins while fixing the rest of the system. In metals both methods are expected to differ [26]. While in the former technique only a slight rotation is performed without changing the potentials, in the latter two completely different configurations are calculated self-consistently. In semiconductors and local moment systems in general, however, both techniques are expected to give reasonable results. Even without performing a Monte-Carlo simulation the Curie temperature T_c can be estimated. Most frequently the mean-field approximation (MFA) [29] is used. It is based on rewriting the product of quantum mechanical operators $\hat{A}$ and $\hat{B}$ as

$$\hat{A} \cdot \hat{B} \to \hat{A} \cdot \langle \hat{B} \rangle + \langle \hat{A} \rangle \cdot \hat{B} - \langle \hat{A} \rangle \cdot \langle \hat{B} \rangle + (\hat{A} - \langle \hat{A} \rangle)(\hat{B} - \langle \hat{B} \rangle). \qquad (2.19)$$

The brackets $\langle \ \rangle$ denote a thermodynamical average. In the MFA the last term in expression 2.19 is neglected. It accounts for the fluctuations of the operators around their averages. The neglect of fluctuations has the effect that the estimates for T_c are too high and should rather be seen as upper bounds. However, T_c can successfully be estimated from above using the simple formula:

$$T_c = \frac{2S(S+1)}{3k_B} \frac{1}{N} \sum_{i \neq j} J_{ij}, \qquad (2.20)$$

the Boltzmann constant is denoted as k_B and N is the number of atoms included [23]. Above expression will be used in a later section to estimate the Curie temperature of zincblende CaAs.

2.5 Non-collinear magnetic order

There are mainly two models trying to explain the occurrance of non-collinear magnetic order. For a system with local moments and short range interactions non-collinearity usually is due to geometric frustration of AFM interactions. Frustration occurs if the magnetic interactions strongly prefer a certain spin-alignment (in most cases AFM) that is not compatible with the geometry of the lattice. For example in an fcc lattice collinear AFM is always frustrated. This is because the fcc lattice is no two-sublattice structure. In other words it is not possible to distribute the atoms into groups A and B so that all atoms in A have only neighbors of type B and vice versa. A simpler example of frustration is drawn in fig. 2.2. Even in a regular triangle it is impossible to align all atoms in a collinear AFM fashion. Prominent examples for frustrated systems are elemental Mn [30] and Mn/Cr on a Cu(111) surface [31]. Mn is particularly well suited for the occurrence of frustration because it usually strongly favors AFM due to its roughly half filled 3d-shell. However, geometric frustration does not necessarily lead to non-collinear order. One
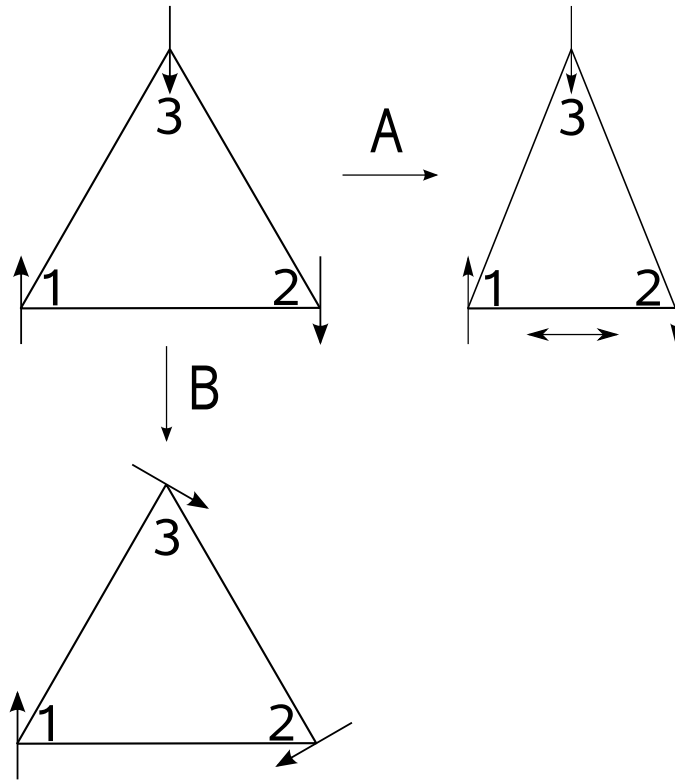
Figure 2.2: Upper left triangle: Geometric frustration of AFM interactions: Atoms 1 and atom 2 are coupled AFM, however, atom 3 can either be aligned AFM with 1 or with 2, but never with both at the same time. Frustration can be reduced either by distortion (A) or by non-collinear order (B).

alternative way to overcome frustration are lattice distortions. For the triangle this means that one pair of atoms approaches each others and two pairs increase their mutual distance. Since the magnetic interactions usually are strongly dependent on the inter-atomic distance, distortion can significantly reduce the degree of frustration. Another alternative is that no magnetic order arises at all. In that case the material either freezes below a certain freezing temperature into an arbitrary snap-shot of one of its highly degenerate spin-configurations (spin glass), or it remains a so-called spin liquid [32]. These cases, however, are very rare and at best found in low-dimensional (e.g. layered) materials.

Apart from frustration one can access the problem of non-collinear order also in a reciprocal space picture. As demonstrated in the previous section, the Stoner criterion yields possible instabilities against ferromagnetism. However, the criterion can be generalized to the cases of collinear AFM and spin-spiral states. For that purpose the bare susceptibility χ_0 for

Bloch states labeled with $\boldsymbol{k},\boldsymbol{k}'$ and band-indices μ and ν is required:

$$\chi_0(\boldsymbol{q}) = \sum_{\boldsymbol{k}\nu\mu} \frac{[f(\epsilon_{\boldsymbol{k}\nu}) - f(\epsilon_{\boldsymbol{k}-\boldsymbol{q}\mu})]}{\epsilon_{\boldsymbol{k}-\boldsymbol{q}\mu} - \epsilon_{\boldsymbol{k}\nu} + i\delta} \cdot |\langle \boldsymbol{k}\nu|e^{i\boldsymbol{q}\boldsymbol{r}}|\boldsymbol{k}-\boldsymbol{q}\mu\rangle|^2 . \tag{2.21}$$

The functions $f(\epsilon)$ denote the Fermi distribution function. The criterion now reads

$$\chi_0 I \geq 1. \tag{2.22}$$

The enhanced susceptibility is defined by

$$\chi = \frac{\chi_0(\boldsymbol{q})}{1 - \chi_0(\boldsymbol{q})I}. \tag{2.23}$$

This generalized Stoner criterion (2.22) says that if a $\boldsymbol{q}$-vector exists for which χ_0 exceeds $1/I$, the system will be unstable with respect to magnetic order. The corresponding type of order might be a spin-spiral with propagation vector $\boldsymbol{q}$ and a magnetization vector at the site ν of magnitude m_ν:

$$\boldsymbol{m}_{n\nu} = m_\nu \left[\cos(\boldsymbol{q}\boldsymbol{R}_n + \phi_\nu)\sin(\theta_\nu), \ \sin(\boldsymbol{q}\boldsymbol{R}_n + \phi_\nu)\sin(\theta_\nu), \ \cos(\theta_\nu)\right]. \tag{2.24}$$

The index n labels the atom at $\boldsymbol{R}_n$ and θ is the azimuthal angle with $\theta{=}0$ being equivalent to ferromagnetism. The criterion can be made plausible by recalling the generalized Bloch theorem [7]. It exploits the fact that if one combines a lattice translation $\boldsymbol{R}_n$ and a spin-rotation by the angle $\boldsymbol{q}\,\boldsymbol{R}_n$, the spin structure remains unchanged [7]. As a consequence certain $\boldsymbol{k}$-states, even though belonging to different spin-channels (up and down), start to hybridize.

$$\left(\boldsymbol{k} - \frac{1}{2}\boldsymbol{q}, \uparrow\right) \text{ and } \left(\boldsymbol{k} + \frac{1}{2}\boldsymbol{q}, \downarrow\right). \tag{2.25}$$

This hybridization can significantly reduce the total energy of a system if the Fermi-surface has nesting features. Nesting means that there are large regions on the Fermi-surface that can be connected via one and the same $\boldsymbol{q}$-vector. They cause local or global maxima in the generalized susceptibility χ_0 and instabilities against spin-spiral or non-collinear structures.

Part II

Semiconductors

Chapter 3

Magnetic Semiconductors

In conventual electronic devices the charge of the electron is the only property being exploited. This might change in the future. Recently a new technology called spintronics (short form for spin-based electronics) has emerged that uses the electron-spin as additional source of information. This opens the door to many new and promising devices. The new possibilities range from non-volatile storage, increased data processing speed, decreased electrical power consumption and increased integration densities compared to conventual, charge-based semiconductor devices [33, 34]. One of the key ingredients of spintronic devices are so-called spin filters. They are ferromagnetic and conduct only electrons of one, defined spin direction. This is why they are also called half-metals, being metallic for a preferred spin-direction and insulating (semiconducting) for the other. The word "half-metal" has first been used by de Groot et al. [35] in the case of the half-metallic Heusler-alloy NiMnSb. One of the hopes of the physicists is now to find new half-metals and magnetic semiconductors in general with Curie temperatures T_c as high as possible, but at least above room temperature. This, however, is a very challenging task. There exist two types of magnetic semiconductors. The concentrated magnetic semiconductors (CMS) are already known for some time. The prototype is $CrBr_3$ with T_c=37 K [36], well-known are also the Eu chalcogenides (EuO and EuS) and the Cr spinels (e.g. $CdCr_4S_4$). They are stoichiometric and their properties are rather insensitive to external influences such as e.g. doping. Unfortunately, the CMS often do not meet the requirements imposed by semiconductor engineers. Spintronic applications require thick films, layers, quantum dots, etc. retaining the useful physical as well as chemical properties of semiconductors. One hence needs materials being compatible with tetrahedrally coordinated semiconductors. As a consequence so-called dilute magnetic semiconductors (DMS) are in the center of interest now. DMS are semiconductors with a small amount (several percent) of defects. These defects are either alien atoms expected to carry a local moment (e.g. substitutional

Mn in GaAs) or designed intrinsic (or extrinsic) defects of the host itself, such as vacancies or interstitial atoms (e.g. O vacancies in In_2O_3). Unfortunately, ferromagnetic long range order with reasonably high T_c requires a subtle interplay between local moments usually carried by conventual magnetic elements (Mn,Fe,Co,etc) and defects (e.g. O-vacancies) mediating the magnetic interaction. The challenge is to insert magnetic impurities in a concentration as high as possible without destroying the host's semiconducting properties. The high concentration (several percent), however, is required in order to reach magnetic percolation, making collective ferromagnetism only possible. The final question is whether the dominant magnetic coupling is indeed ferromagnetic. In the present work transition metal doped Cu_2O, a representative of the DMS, and CaAs, a (hypothetical) member of the CMS having the highly desired zinc-blende structure combined with a high T_c, will be discussed in detail.

3.1 Basic physical properties

In contrast to metals semiconductors are materials with an energy gap at the Fermi energy E_F. If this gap is larger than 2 eV one already speaks about an insulator. The gap separates the occupied valence bands (VB) from the unoccupied conduction bands (CB), it is situated between the so-called valence band maximum (VBM) and the conduction band minimum (CBM). The most common semiconductors are Si and Ge. They crystallize in the cubic diamond structure. Also the III-V (GaAs, InSb) and II-VI (CdTe) semiconductors are of great technological importance. There is a clear structural trend for the binary AB semiconductors. When the electronegativity difference between A and B increases, the structure changes from diamond (and zinc-blende) over wurtzite to rock-salt (e.g. for I-VII CuBr). The reason is that the electrostatic interaction, favoring closed-packed structures, becomes increasingly important. The gap in elemental, tetrahedral semiconductors is neither a consequence of long-range periodicity ([37]) nor a result of energy bands being too narrow to form a continuous band. It instead comes from the covalent bond itself (see below). Only in very ionic compounds the gap is rather determined by the difference in the atomic energy levels of cation and anion, the electronegativity-difference. A simple expression for the gap E_g in a s-valent dimer with s-level mismatch ΔE is given as

$$E_g = (4h^2 + (\Delta E)^2)^{1/2}, \tag{3.1}$$

h is the covalent bond integral [38], a quantity similar to the hopping term in tight binding. Since the anti-bonding orbitals are empty, semiconductors exhibit strong cohesion and are hard but brittle materials. If impurities are inserted deliberately one speaks about doping. In the limit of low concentrations the impurities form sharp levels usually inside

the host band-gap (non-degenerate semiconductor), in the case of higher concentrations the impurities form bands (degenerate semiconductor). If the impurity states are situated close to the CBM (VBM) one speaks about n-type doping and donors (p-type doping and acceptors). Doping with either electrons or holes significantly changes the electrical conductivity because in doped materials thermal activation allows for an increase of the carrier concentration. Consequently the conductivity increases with increasing temperature. If the impurity states are close to (far from) the band-edges one speaks about shallow (deep) levels. In a non-degenerate, doped semiconductor shallow donors (acceptors) can be seen as electrons (holes) occupying effective Bohr orbits similar to the single electron in the H-atom. The only difference is that in the semiconductor one has to take into account the effective mass $m^\star$ of the carrier as well as the electrical polarizability of the host, expressed in the dielectric constant ϵ. The radial extension r_0 of this effective Bohr orbit is given by

$$r_0 = \epsilon r_B \frac{1}{m^\star}, \tag{3.2}$$

with the first Bohr radius $r_B = 1$ (atomic units). The effective mass of the carrier $m^\star$ is given in multiples of the electron mass m_e. Typical values of r_0 are around 100Å. In tetrahedral III-V and II-VI semiconductors holes usually have p-like character and high effective masses $m^\star$ due to a low dispersion at the VBM. Contrarily, electrons tend to be s-like having much smaller $m^\star$ (higher dispersion at the CBM).

In order to understand the diamagnetic nature of covalent semiconductors it is useful to recall that the covalent bond can be seen as a quantum interference effect between overlapping wavefunctions in the region between the corresponding atoms. In a two-sublattice structure, where all atoms of type A have only neighbors of type B and vice versa, one can speak about bonding and anti-bonding orbitals [39]. The bonding orbitals accumulate charge between the atoms weakening the electrostatic core-core repulsion. The anti-bonding ones pull the atoms further apart. For this reason the spin-paired singulett is energetically favored because the electrons can come arbitrarily close to each others (no Pauli exclusion) and together occupy the (even) bonding orbital. It has been first pointed out by Pauling [40] that those structures that avoid the necessity of electron exclusion in the region of orbital overlap are stabilized relative to those that do not. Following Goodenough, if the near neighbor overlapping atomic orbitals of a two-sublattice structure are half filled, optimum binding occurs when the electron pairs are singuletts [39]. This explains why the classical, elemental semiconductors have tetrahedral coordination with four nearest neighbors and also four outer electrons contributing to the bond (octet rule). Due to this singulett pairing there is no resulting magnetic moment on the atoms. It is important to recall that the covalent bond is an exception and only found in isovalent materials. If two different elements are involved, one can speak about cation (+) and anion

(-). Nevertheless, above argumentation regarding orbital overlap as well as bonding and anti-bonding orbitals is assumed to be valid also for moderately ionic compounds.

3.2 Defects and formation energies

In DMS long range order often crucially depends on defect-related free carriers. This is why a controlled preparation process is desired. The most common defects are vacancies of either anions V_a or cations V_c, the former acting as donors, creating impurity states close to the CBM, the latter as acceptors. Also anti-sites A_B, with type A atoms occupying a B site, and alien atoms - either isovalent or with different valency - are common. A measure of how easy it is to incorporate a particular defect into a material is the the formation enthalpy ΔH. It can actively be influenced by the conditions under which the material is prepared, by the so-called growth conditions. The formation enthalpy $\Delta H_{D,q}(E_F, \mu)$ is given by [41]:

$$\Delta H_{D,q}(E_F, \mu) = (E_{D,q} - E_H) + \sum_\alpha n_\alpha(\Delta\mu_\alpha + \mu_\alpha^{solid}) + q(E_v + E_F). \qquad (3.3)$$

The terms $E_{D,q}$ and E_H denote the total energy with and without defect D having the charge state q. The second term accounts for the energy change due to the exchange of atoms with the chemical reservoir, n_α being -1 if an atom is added and +1 if an atom is removed. The $\Delta\mu_\alpha$ are defined as the energy difference between the chemical potential of the corresponding element α, μ_α^{solid}, and the atomic chemical potentials μ_α in the compound of interest. The $\Delta\mu_\alpha$ are always negative guaranteeing that compound is more stable than its constituents alone. Considering for example the binary compound AB_2, the sum of the chemical potentials of its constituents must equal the formation enthalpy of the compound AB_2:

$$\Delta\mu_A + 2\Delta\mu_B = \Delta H(AB_2). \qquad (3.4)$$

However, one has a degree of freedom in the choice of the $\Delta\mu_\alpha$. This can be exploited during the preparation process in order to favor particular types of defects. The $\Delta\mu_\alpha$ can be chosen to lie between two border cases, the A-rich preparation using $\Delta\mu_A=0$ and $\Delta\mu_B = \Delta H(AB_2)/2$ and the B-rich preparation $\Delta\mu_B=0$ and $\Delta\mu_A = \Delta H(AB_2)$. The chemical potentials can be further restricted by competing phases, which is in particular important for ternary compounds. The third term in equ. 3.3 is only important for charged defects with $q \neq 0$. It accounts for the fact that the formation enthalpy and consequently the probability for a charged defect to be present depends on the position of E_F within the band-gap of the host, measured relative to the energy of the VBM, E_v. Positively charged defects (donors, q positive) are more stable if E_F is situated as low as possible within the

gap, negatively charged defects (acceptors, q negative) require E_F to be situated close to the CBM. Some more rules of thumb for doping are outlined in ref. [42]. The equilibrium defect concentration can be related to the formation enthalpies via the Boltzmann distribution:

$$c_{D,q}(E_F, \mu_\alpha, T) = N\exp[-\Delta H_{D,q}(E_F, \mu_\alpha)/(k_B T)], \qquad (3.5)$$

where N is the concentration of atomic sites substituted by the defect D having charge state q. Thus the equilibrium defect concentration has to be solved self-consistently using equ. 3.3 and equ. 3.5.

However, when dealing with semiconductors one has to apply several corrections in order to determine formation enthalpies reliably. If LDA/GGA is used, first of all the gap has to be corrected. If charged defects in supercells are considered, the potential is determined only up to a constant. For this reason it has been suggested that different calculations should be made comparable by aligning the potential at a reference point far from the defect. Moreover, image charge corrections as well as band-filling corrections are sometimes applied in order to cope with the finite size of the supercell and the resulting spurious interaction of the impurity with its counterparts in the periodically continued solid. A good review regarding above mentioned corrections can be found in ref. [41, 43].

3.3 Exchange interactions

Ferromagnetism in CMS/DMS can be invested theoretically either by model Hamiltonians such as the Kondo Hamiltonian and the Anderson Hamiltonian (for an overview see [44]) or by ab-initio methods, employing either ordered super-cell calculations or the CPA approximation [25]. However, it is rather hard to translate the results of model Hamiltonians into the language of band-structure methods and vice versa. Up to now there is no complete theory explaining magnetism in DMS, only several models have developed being rather restricted regarding their range of applicability. In the following several exchange mechanisms will be discussed. Even though direct exchange is not so important for semiconductors it is included because it is a good starting point for the indirect exchange mechanisms.

3.3.1 Direct exchange

Two simple cases can be studied in order get a feeling of how direct exchange works [45]. In the first model-system one consideres two electrons occupying the same shell, e.g. a 3d-shell. The two-electron Hamiltonian is of the form

$$H = h_0(\boldsymbol{r}_1) + h_0(\boldsymbol{r}_2) + \frac{1}{|\boldsymbol{r}_1 - \boldsymbol{r}_2|}, \qquad (3.6)$$

$h_0(\boldsymbol{r})$ are the (spin-independent) one-electron Hamiltonians, and the last term is the Coulomb interaction. The electrons occupy the orthogonal orbitals ϕ_a and ϕ_b, eigenstates of h_0 with the one-electron eigenenergies ϵ_a and ϵ_b. The total wavefunction is a Slater determinant of spin-orbitals, orbital functions ϕ combined with the spin functions for either spin up α or spin down β. All combinations of (ϕ_a, ϕ_b) with (α, β) are allowed, provided that there is always one singly occupied orbital ϕ_a and one singly occupied orbital ϕ_b. Only the spins can be varied allowing for 4 different Slater determinants, two with spin-parallel and two with spin anti-parallel. The energy difference between singulett ϵ_s and triplett ϵ_{tr} is given by

$$\epsilon_{tr} - \epsilon_s = (\epsilon_a + \epsilon_b + C_{ab} - J_{ab}) - (\epsilon_a + \epsilon_b + C_{ab} + J_{ab}) = -2J_{ab}, \tag{3.7}$$

with the Coulomb integral C_{ab}

$$C_{ab} = \int d^3r_1 \int d^3r_2 \, \frac{|\phi_a(\boldsymbol{r}_1)|^2 \, |\phi_b(\boldsymbol{r}_2)|^2}{|\boldsymbol{r}_1 - \boldsymbol{r}_2|}, \tag{3.8}$$

and the exchange integral J_{ab}

$$J_{ab} = \int d^3r_1 \int d^3r_2 \, \frac{\phi_a^\star(\boldsymbol{r}_1)\phi_b(\boldsymbol{r}_1)\phi_b^\star(\boldsymbol{r}_2)\phi_a(\boldsymbol{r}_2)}{|\boldsymbol{r}_1 - \boldsymbol{r}_2|}. \tag{3.9}$$

The most important result is that J_{ab} is always positive and the triplet state lower in energy. Generally speaking, direct exchange of electrons occupying mutually orthogonal orbitals is always ferromagnetic [45]. This is a mathematical justification of the first Hund rule.

The second model-example is the LCAO treatment of the H_2 molecule, with the simplification that only charge neutral configurations with not more than one electron at one nucleus are considered (Heitler-London treatment). Since the one electron orbitals ϕ_a and ϕ_b are shifted by the nuclear separation R_{ab} and supposed to describe binding, they can no longer be orthogonal and the corresponding overlap integral is defined as $l = \int \phi_a^\star(\boldsymbol{r})\phi_b(\boldsymbol{r})$. The energy difference between singulett and triplett state is given by

$$\epsilon_{tr} - \epsilon_s = 2\frac{l^2 C_{AB} - J_{AB}}{1 - l^4}, \tag{3.10}$$

with the Coulomb term C_{ab} and the exchange term J_{ab} defined as above, with the only difference that there are additional terms due to the interaction of electrons with the neighboring core. Due to the overlap the energy difference between singulett and triplett now can change sign. The case of orthogonal orbitals is restored for $l = 0$, yielding the triplet state. If the overlap is sufficiently large ($l^2 C_{ab} \geq J_{ab}$) the exchange coupling is anti-ferromagnetic yielding a singulett state. Thus one expects AF coupling of spins in

Table 3.1: Percolation treshholds for various lattices and lengths of interactions. The distances are the effective interaction radii $d_{ij}/v_{atom}^{1/3}$, taking into account also the volume of the non-magnetic counterparts (e.g. there is 1 anion and 1 cation within the CsCl unit-cell, but only the cation sublattice plays a role for percolation) [48].

	NaCl-fcc sublattice		CsCl-sc sublattice		diamond	
# NN (dist)	12	(1.414)	6	(1.260)	4	(0.866)
# NN2 (dist)	6	(2.000)	12	(1.782)	12	(1.414)
# NN3 (dist)	24	(2.450)	8	(2.182)	12	(1.658)
# NN4 (dist)	12	(2.829)	6	(2.520)	6	(2.000)
# NN5 (dist)	24	(3.162)	24	(2.817)	12	(2.180)
Perc. NN [%]	19.8		31.2		43.1	
Perc. NN2 [%]	13.7		13.8		14.7	
Perc. NN3 [%]	6.2		9.8		9.3	
Perc. NN4 [%]	4.9		8.0		7.6	
Perc. NN5 [%]	3.4		4.6		5.7	

cases of strong covalent bond, being in agreement with the discussions made above about the non-existence of magnetic moments in semiconductors. However, in semiconductors direct exchange between local d(f) orbitals originating from magnetic elements is short-ranged. Consequently this mechanism is not important if the concentration of the magnetic impurities is low and the mean-distances amongst them is large. Only in CMS or in DMS exhibiting strong, unwanted clustering one expects direct exchange to play a role. Much more important are indirect exchange interactions. They need an intermediate partner transferring the information regarding the spin-orientation of one impurity site to another site. These intermediate states have to be weakly localized and can be either holes [46] or electrons [47]. Thus the appropriate doping with either intrinsic or extrinsic defects is crucial for the occurrance of magnetic long range order. In order to get a feeling of how far-reaching the interactions have to be for a fixed concentration of impurities, the percolation treshholds for various simple lattices are listened in tab. 3.1 taken out of ref. [48]. One finds that e.g. in the diamond lattice 7.6 % of substitutional impurities are required in order to allow for percolation if the magnetic interactions range until the 4th nearest neighbor-shell. For the fcc lattice the percolation concentration is lowest for a given range of interaction.

3.3.2 RKKY interaction

The RKKY interaction was first proposed by Ruderman and Kittel [49] and later extended by Kasuya and Yoshida. It has originally been developed for nuclear magnetic moments in a metal. It is an indirect interaction of local moments via conduction electrons. If one puts an impurity into the free electron gas, slowly decaying oscillations of the electron charge density centered around the perturbation are found. These so-called Friedel oscillations are a consequence of screening. If the oscillations are different for spin-up and spin-down electrons one expects oscillations of the magnetization density. The mutual interaction of two impurities via the oscillations of their corresponding magnetization densities is then called RKKY interaction. For an impurity within a simple cubic lattice assuming the free electron dispersion and zero temperature, the interaction is of the form [45]

$$I(\boldsymbol{R}_i - \boldsymbol{R}_j) = -\frac{J^2}{\pi^3} \left(\frac{k_F a_0}{2}\right)^6 \frac{\sin 2k_F R_{ij} - 2k_F R_{ij} \cos 2k_F R_{ij}}{(2k_F R_{ij})^4}, \qquad (3.11)$$

and the corresponding Hamiltonian is given by

$$H_{RKKY} = \sum_{\boldsymbol{k},\sigma} \epsilon_{\boldsymbol{k}} \hat{n}_{\boldsymbol{k},\sigma} + \frac{1}{2} \sum_{i \neq j} I(\boldsymbol{R}_i - \boldsymbol{R}_j)\, \boldsymbol{S}_i \boldsymbol{S}_j. \qquad (3.12)$$

The argument of I, $R_{ij} = \boldsymbol{R}_i - \boldsymbol{R}_j$, denotes the distance between the magnetic impurities, a_0 the simple cubic lattice constant and J the direct exchange constant between the impurity and the conduction electrons. The period of the oscillation is determined by the Fermi-surface diameter k_F. There exist two important limits. In the limit of high carrier concentrations and low concentrations of magnetic impurities ($2k_F R_{ij} \gg 1$) the RKKY interaction changes sign and spin-glass behavior can be found. In the other limit, namely low carrier concentrations and high concentrations of magnetic impurities ($2k_F R_{ij} \ll 1$), the RKKY interaction is always FM. In undoped semiconductors the lack of free carriers leads to an exponential decay of the RKKY interaction and it becomes insignificant. For systems with a higher concentration of carriers the role of the RKKY interaction (e.g. as part of the mean-field Zener model) is still under debate [50].

3.3.3 Superexchange

One important magnetic exchange interaction in insulators and semiconductors is superexchange [51]. The word "super" comes from the peculiarity that the magnetic coupling of local moments on the cation M (usually a metal like Mn, Fe, ..) is mediated by an anion X (e.g. N,O,F), which has a formally filled shell and plays the role of an intermediary. Superexchange is no direct cation-cation but a cation-anion-cation interaction. In most cases
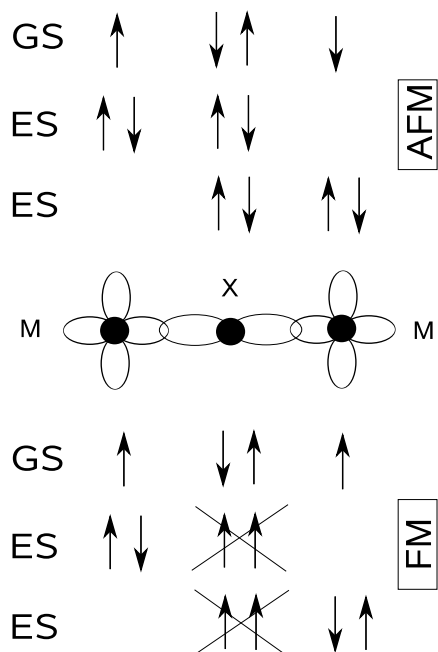
Figure 3.1: Kinetic superexchange: If the cations couple AF not only the ground state (GS) but also the 2 excited states (ES) are virtually accessible through virtual electron hopping without spin-change.

AFM alignment is favored. Following Goodenough [39] there are (mainly) two important sources of superexchange: Correlation superexchange and delocalization (or kinetic) superexchange. The former mirrors the fact that the cation spins are likely to be coupled in a way that bond formation on both sides of the anion is possible simultaneously. Delocalization or sometimes also called kinetic superexchange exploits the fact that if the electron is allowed to virtually hop from one cation to the other the energy is lowered because excited states are mixed to the ground state. The higher the symmetry of the bond, the easier is the analysis, e.g. for bond angles different from 180° the analysis is much more complicated because mixed σ- and π- bonding occurs. For the following considerations always 180° superexchange will be assumed. Qualitatively one can say that superexchange usually causes orbitals having strong overlap to couple AFM and orthogonal (e_g and t_{2g} on the same atom) or weakly overlapping orbitals to couple FM due to intra-atomic exchange. In principle the higher the orbital overlap is, the stronger is the interaction. In a simple picture superexchange interactions become weaker if the ionicity of the cation-anion bond increases. If half filled orbitals are involved superexchange leads to strong, effective AFM coupling of cations. The AFM state is lowered compared to the FM by the energy
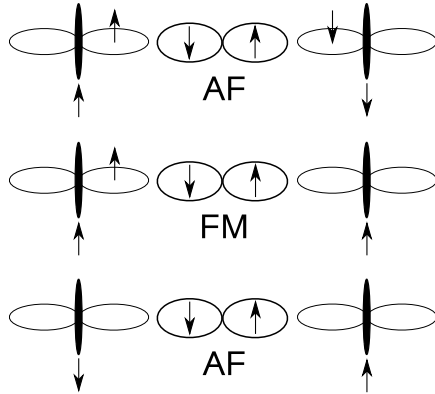
Figure 3.2: Superexchange involving two orthogonal orbitals on the cation: Only in one case FM occurs because the electron on the anion can virtually hop to the cation on the right hand side because intra-cation exchange favors FM alignment of the transferred electron to that already present on the cation.

$$\Delta E = E_{FM} - E_{AFM} = -2J$$

$$J \propto -\frac{t^2}{U}, \tag{3.13}$$

U is the intra-atomic energy cost for a double-occupation of a single orbital and t is a quantity related to the tight-binding hopping term, proportional to the band-width or alternatively to the probability that the electron hops from the cation to the anion or vice versa. It can be derived from second order perturbation theory. In fig. 3.1 (left panel) a simplified picture of superexchange is shown. The AFM configuration is lower in energy because for that configuration not only the ground-state (GS) with both electrons being attributed to the anion but also 2 excited states (ES) being in accordance with Pauli's principle are possible. In special cases superexchange can lead to ferromagnetism. For this it is necessary that two orbitals on the cation are involved. One cation must have a half-filled orbital and the other one an empty one, which is only possible if the magnetic moment comes from an orbital not participating in the bond. In that case FM is found because of intra-cation, direct exchange between the virtually transferred electron and the electron in the non-bonding orbital. For semiconductors superexchange is often described in a band-picture [44]. The free carriers (e.g. holes in the valence band) have now the role of the anions and superexchange can be seen as an interaction in which the local spins on two ions (e.g. impurity d-states) are correlated due to the spin-dependent exchange interaction between each of the ions and the valence p-band (or conductions s-band). Examples for semiconductors which are believed to couple FM via superexchange are the II-VI compounds such as Cr doped ZnTe[52, 53]. $Zn_{1-x}Cr_xTe$ with $x=0.035$ for example,
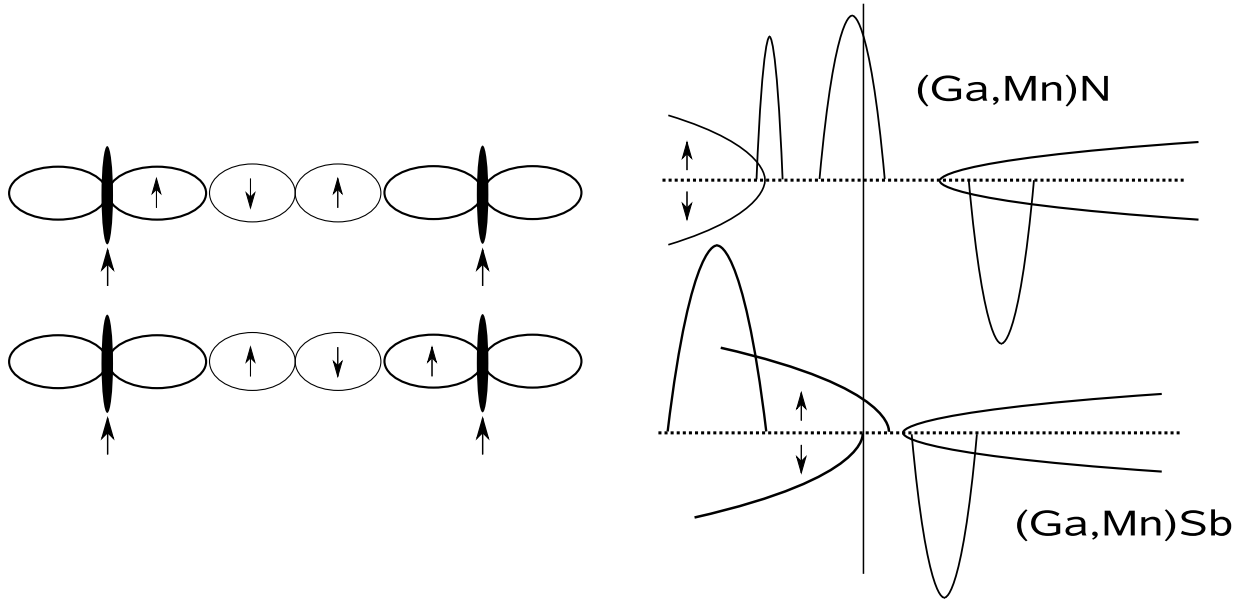
Figure 3.3: Left panel: Double exchange favors FM because it allows charge transfer between the left and the right magnetic ion. Right panel: The trend within the series (Ga,Mn)X with X=N, P, As, and Sb goes from double exchange in (Ga,Mn)N to mean-field Zener exchange in (Ga,Mn)Sb.

even though suffering from rather low $T_c \approx 15K$, has the advantage that low carrier concentrations are required. In contrast to many other systems like (Ga,Mn)As (see later) magnetism is not primarily dependent on the carrier concentration because superexchange works via virtual charge fluctuations and not via real electron transfer.

3.3.4 Double exchange

Double exchange in its original form of Zener [54] occurs in compounds having mixed valence. One of the prototypes is the perovskite $(La,A^{+2})MnO_3$, with Mn^{+3} coexisting with Mn^{+4} in the case La is partially substituted by a divalent element A. Double exchange always favors a spin-alignment that allows for charge transport. This charge transport involves a real hopping process and not a virtual transition like in the case of superexchange. While superexchange lifts the degeneracy of the two, virtual excited states (ES) at energy U while keeping fixed the charge on the magnetic element, double exchange occurs between differently charged ions (e.g. Mn^{+3} and Mn^{+4}) and involves delocalized electrons. The left panel of fig. 3.3 illustrates double exchange. There are two types of orbitals involved, localized ones and orbitals that allow electron hopping from one magnetic ion to the other. Charge transfer can only occur if the magnetic moments are aligned ferromagnetically.

This is because intra-atomic exchange favors FM alignment between the itinerant electrons and the localized ones not participating in the bond. Double exchange always favors ferromagnetism. In a band-picture double exchange can be identified by comparing the AFM and the FM bandstructure. While superexchange favors situations with a gap at the Fermi energy and AFM alignment, double exchange broadens the bands at E_F in the FM state. This band-broadening lowers the total energy. It is hence necessary that E_F falls into a partially filled impurity band if a FM set-up is assumed. In (In,Mn)As it was proposed by Akai that double exchange leads to ferromagnetism [55]. Sato et al. argued that there is a trend within the series (Ga,Mn)N $\rightarrow$ (Ga,Mn)Sb from double exchange in the former to the Zener p-d exchange (next paragraph) for the latter. This is also shown in the right panel of fig. 3.3. The energy gain due to double exchange is proportional to the band width W of the band at E_F, which in a mean-field approximation results in a $\sqrt{c}$ dependence of the Curie Temperature T_c on the impurity concentration c. The higher the impurity concentration the more relevant double exchange becomes.

3.3.5 Models based on host polarization

The mean-field Zener model (or Zener p-d exchange) was proposed by Dietl *et al.* [46]. It was successful in explaining the transition temperatures for p-type (Ga,Mn)As and (Zn,Mn)Te. The mean-field Zener model is based on the original model by Zener but it includes the RKKY interaction. It also takes into account the anisotropy of the carrier-mediated (hole-mediated) exchange interaction due to spin-orbit interaction in the host. It is only applicable to systems exhibiting a significant p-d interaction. For the model to work it is necessary that the strong p-d interaction leads to a spin-polarization of the valence band and to weakly localized, uncompensated holes. In the bottom right panel of fig. 3.3 the mean-field Zener mechanism is demonstrated for the case of (Ga,Mn)Sb. In contrast to (Ga,Mn)N, which has a larger gap and impurity Mn-states lying completely within the gap, in (Ga,Mn)Sb the Mn spin-up states lie deep within the host valence states. The strong localization of the Mn d-states leads to an up-shift of the valence band for the minority electrons and hence to an effective (AFM) spin-polarization of the host [56]. This polarization of the host makes a long-range interaction between magnetic impurities in DMS possible. One of the key elements of the model is the mean-field Kondo-like coupling between the host valence band and the magnetic impurity

$$H_{sp-d} = -N_0 \beta \boldsymbol{S} \cdot \boldsymbol{s}, \tag{3.14}$$

with the exchange constant β, the concentration of magnetic sites N_0, the impurity spin $\boldsymbol{S}$ and the the carrier spin $\boldsymbol{s}$. The Curie temperature T_c increases quadratically with the

exchange constant β:

$$T_c = \frac{x N_0 S(S+1)\beta^2 \chi_s}{3 k_B (g^\star \mu_B)^2}, \tag{3.15}$$

with the spin concentration $x N_0$, the magnetic susceptibility of the free carriers χ_s, their gyromagnetic ratio $g^\star$, the Boltzmann constant k_B and the Bohr magneton μ_B. Another result of the mean-field Zener model is that semiconductors with light anions (C,GaN, InN) are expected to have higher T_c than representatives with heavier anions (GaSb). Dietl *et al.* also observed a principal difference between the II-VI and III-V compounds, the II-VI ones having reduced T_c due to stronger superexchange counteracting the FM interaction. Unfortunately, in contrast to the II-VI compounds the experimental determination of β for the III-V compounds seems to be not conclusive. Both, sign and the magnitude are not well known, in particular for large Mn concentrations.

A different mechanism responsible for FM in n-type materials has been put forward by J. M. D. Coey et al. [47]. They assume an impurity band at the CBM. This impurity band becomes significantly polarized if it coincides energetically with empty d-states, either for spin-up (early TM) or spin-down (late TM). The polarization of the impurity band then mediates the long range interaction, similar to the case of holes in the mean-field Zener model.

Chapter 4

Tetrahedral CaAs and related I/II-V compounds

Many of the CMS systems have crystal structures incompatible to semiconductor structures. In this chapter a possible, new route for designing CMS is introduced [57]. It is based on forcing a material into a structure that is not its equilibrium ground state structure. Recent developments in non-equilibrium (low temperature), epitaxial growth (e.g. thin films) are getting increasingly successful. This opens the door to new, completely different techniques in materials design.

Recently Kusakabe et al. [58] proposed magnetic zinc-blende CaAs as a possible material for spintronics application. Their proposal was motivated by the need for half metallic ferromagnets in spintronic devices [59], which are seen as key ingredients. However, apart from the technological application the magnetic I/II-V compounds represent a new class of ferromagnetic materials where magnetic order is carried by the anion p-electrons without any direct involvement of d-electrons as in the magnetic transition metals and their compounds. The p-electron magnetism in CaAs and the other I/II-V systems appears in the fully ordered stoichiometric compounds and their magnetic order is intrinsic and not triggered by the presence of crystal defects of various kinds. Examples for this defect triggered p-electron magnetism are irradiated pyrolytic graphite containing defects [60, 61, 62] or CaB_6 doped with La [63].

In this chapter we calculate the magnetic and electronic properties of this class of compounds. For the prototypical representative CaAs we study the stability of the zinc-blende and wurtzite phase with respect to i) the true equilibrium structure and ii) tetragonal distortions. For the possible combinations of I/II-V zinc-blende compounds we investigate the occurrance of magnetic order at the respective equilibrium volumes. The appearance of the flat band in the all-electron calculation is confirmed on the basis of a model tight-

binding Hamiltonian of Slater-Koster type. We find that all I/II-V compounds have a tendency toward a ferromagnetic ground state, and the origin of the exchange is neither double exchange nor p-d exchange. In addition, CaAs exhibits an extremely flat, half filled band at the Fermi energy.

The calculations were performed using the FLAIR [18] code, an implementation of the full potential linearized augmented plane wave (FLAPW) method [17]. Exchange and correlation was treated within the local density functional formalism [64] using the generalized gradient approximation of Perdew, Burke and Ernzerhof [65]. The valence states are solutions of a semi-relativistic Hamiltonian, while for core states spin-orbit coupling is included as well. To ensure converged results for the electronic and magnetic properties of all the compounds investigated, potential and charge density were expanded up to $l = 8$ and $G_{\mathrm{max}} = 13$ $a.u.^{-1}$. Inside the spheres the wave-functions are expanded up to $l = 8$ and a plane-wave cutoff k_{max} of $8/\mathrm{min}(r_{MT})$ is used, where $\mathrm{min}(r_{MT})$ denotes the radius of the smallest muffin-tin sphere in the cell. In calculations involving larger unit cells a k_{max} of $6/\mathrm{min}(r_{MT})$ turned out to be sufficiently large. A **k**-mesh sampling with 24×24×24 **k**-points within the full Brillouin zone was found to be satisfactory in most cases. The muffin tin radii r_{MT} were chosen as touching spheres, adapted to the approximate atomic radius to keep as much core charge inside the muffin tin sphere as possible. For comparisons of total energies e.g. in order to optimize lattice constants, the muffin tin radii were chosen as touching spheres for the smallest volume investigated and held constant otherwise. The energy was converged better than 2.7×10^{-6} eV (10^{-7} Hartree).

4.1 Total energy

Since CaAs is the prototype of the half-metallic-ferromagnetic (HMF) systems among the II/V compounds, its total energy has been calculated for several crystal structures:

i) The zinc-blende (ZB) structure (I $\overline{4}$3m, Nr. 216) consists of two inter-penetrating fcc lattices, one of them shifted by the vector $[\frac{1}{4}, \frac{1}{4}, \frac{1}{4}]$, resulting in a two component analog of the diamond structure. Each atom of one kind is situated in an ideal tetrahedron made up of atoms of the other kind. As most semiconductors crystallize in this structure, it is of great technological importance.

ii) The wurtzite (WZ) structure (P 6_3mc, Nr. 186) is the hexagonal analog to the ZB structure and has the same local environment if one assumes the ideal c/a ratio of $\sqrt{8/3}$ and an internal u-parameter of 3/8 for the anion site and 0 for the cation site at the (2b) Wyckoff position [66]. The following discussion is limited to this ideal set-up.

iii) CaAs is rather ionic and thus might favor a higher coordinated atomic arrangement in order to reduce its electrostatic energy. For this reason also the sodium chloride (NaCl)
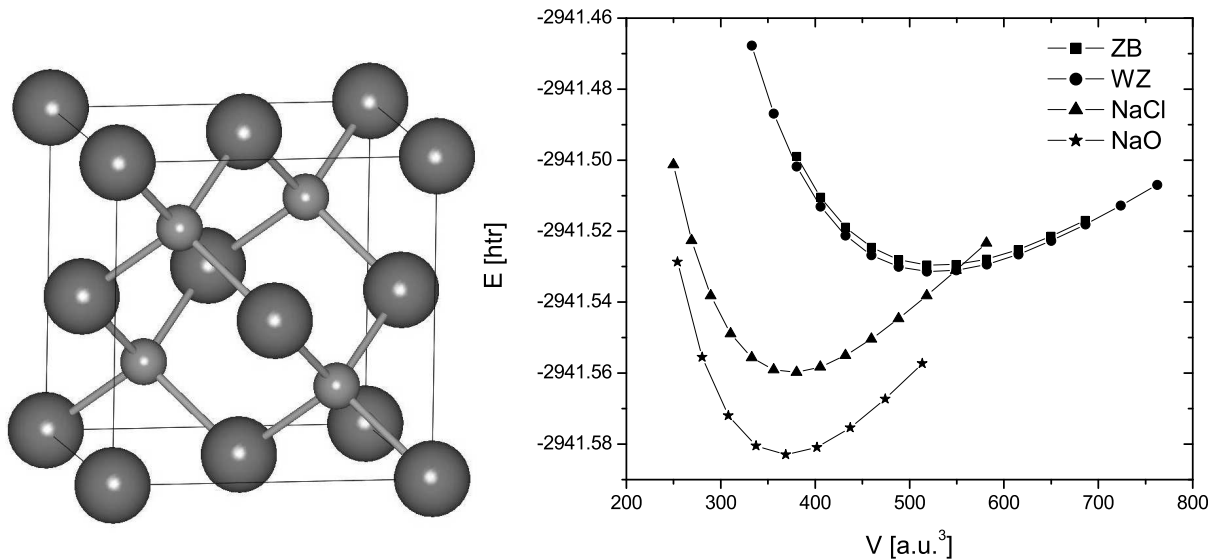
Figure 4.1: (Left panel) Cubic zinc-blende structure. Both, Ca (large, dark spheres) and As (small, light), are tetrahedrally coordinated. The structure is a typical two-subattice structure with Ca having only As nearest neighbors and vice versa. (Right panel) Total energy for CaAs in different crystal structures. Energies and volumes are given per formula unit.

structure (F m$\bar{3}$m, Nr. 225) has been investigated. It consists of two face centered cubic lattices, shifted by the vector $[\frac{1}{2}, \frac{1}{2}, \frac{1}{2}]$, which results in an octahedral coordination for both, cation and anion.

iv) The equilibrium modification for CaAs as reported by P. L'Haridon et al. [67] is the NaO structure (P $\bar{6}$2m, Nr. 189), (a=14.84(2) bohr, c=11.19(1) bohr), which places the As atoms in face-sharing, distorted octahedra. This structure can be derived from the ideal NiAs structure by an exchange of Ni and As atoms, a 30 degree rotation clockwise about the z-axis, a shift of [0,0,0.25] in z direction and finally an increase of the a=b cell parameter by a factor of $\sqrt{3}$. Moreover, the symmetry is reduced due to a distortion of the Ca octahedra, which leads to an enhancement of the mean As-Ca distance by approximately 0.37 %, and a reduction of the mean As-As distance by approximately 3.29 % with respect to the undistorted anti-NiAs parent lattice. To ensure that both, the ZB and WZ structure are calculated with the same accuracy, the ZB structure was transformed into a translational equivalent hexagonal (or trigonal) modification (R3m, Nr. 160) (see [68]). For the former, a **k**-mesh of 8×8×4 and for the latter a mesh with 8×8×6 points was used. This ensures the same k-point density in the Brillouin zone (BZ) so that the numerical errors for different structures due to the limited set of BZ sampling points will cancel. The

47

Table 4.1: Cell volume V/f.u., bulk modulus B, magnetic moment M per f.u., band gap at E_F for spin-up/spin-down and spin splitting ΔE for CaAs in different crystal structures.

	ZB	WZ	NaO	NaCl
V [bohr^3/f.u.]	531	523	369	374
B [GPa]	26	26	46	41
M [μ_B/f.u.]	1	1	0	0
Gap [eV]	2.78/2.30	2.80/2.30	0	0
ΔE [eV]	0.58	0.58	0	0

calculations show (fig. 4.1) that the compounds with the octahedral coordination for the anion – like in NaCl and NaO – are energetically favored. They have a smaller cell volume and a higher bulk modulus, indicating that the bonding is stronger due to the smaller interatomic distances. The experimentally observed NaO structure has indeed the lowest total energy, the calculated lattice constant of 15.03 bohr is in good agreement with the experimentally found value of 14.89 bohr. If one starts a calculation with the corresponding ideal anti-NiAs structure and allows for a relaxation of the atoms, the distortion found is less pronounced as in experiment, and reduces the total energy only slightly (by ≈ 16 meV/f.u.). The comparison of ZB and WZ structure shows that the hexagonal arrangement is lower in energy by approximately 46 meV/f.u., but both exhibit HMF. In contrast to that, CaAs in the NaO as well as the NaCl arrangement is nonmagnetic and metallic at the equilibrium cell volume. Table 4.1 lists the cell parameters, the bulk modulus B (determined from a Murnaghan equation fit [69]), the magnetic moment M, the energy gap, and the spin splitting. Recently Geshi et al. [70] investigated the stability of half metallicity in the ZB structure against tetragonal distortion. They fixed the cell volume to the ZB equilibrium and found two local minima in the total energy for a c/a ratio of $\approx$ 1.47 and 0.66, respectively, where only for the latter half metallicity occurred. The results of a more detailed calculation, including a variation of the cell volume V for each c/a, are shown in fig. 4.2. Our results are only in partial agreement with the findings of Geshi et al. [70], insofar as the cubic structure ($c/a = 1$) is always at a local maximum in energy, but there is no stable solution within the half metallic regime. This becomes evident by comparing the total energy surface with the magnetic moment contour plot in the center panel of fig. 4.2. We find that HMF is present near the cubic symmetry, but vanishes for increasing tetragonal distortion and in general becomes favored only for large cell volumes. The dots crossing the HMF regime mark the equilibrium cell volume at a given c/a-ratio. We find that half metallicity is found for $0.8 \lesssim c/a \lesssim 1.15$ and that the maximum energy
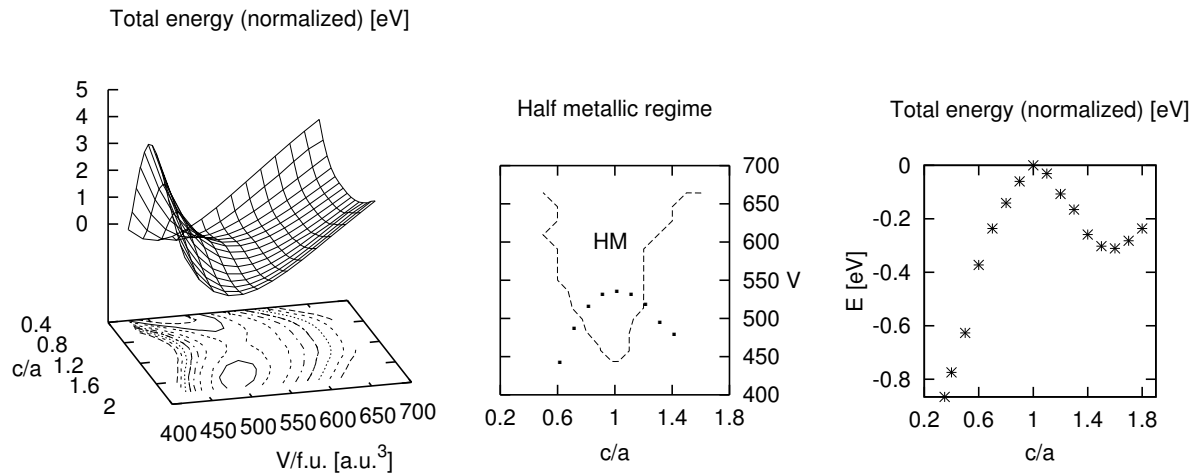
Figure 4.2: Left panel: total energy for CaAs in a tetragonal distorted ZB structure for various values of c/a and volume $V/f.u.$. Center panel: The dashed line marks the existence region of HMF solutions in the c/a vs. V plane; the dotted line denotes the equilibrium cell volume for a given c/a-ratio. Right panel: total energy as a function of c/a and the respective equilibrium volume (minimal energy path in the c/a vs. V plane).

gain within the HMF regime due to the distortion is 0.15 - 0.2 eV/f.u. In the right panel of fig. 4.2 the lowest energy for each c/a ratio is shown. There exists a local (non-magnetic) minimum around 1.55, in the limit of small c/a no stable solution has been found within the investigated c/a-range. These results show that the ground state of CaAs found experimentally is energetically rather far away ($\approx$ 1.4 eV/f.u.) from the structures which are expected to exhibit HMF. Nevertheless, a preparation as a thin film on a substrate may be possible. Due to the large lattice constant of CaAs it might be grown as a kind of superstructure on a ZB-host (related to the host lattice constant by a factor of $\sqrt{2}$), or as a intermediate layer between two stable structures. For the lighter representatives discussed in the following paragraph, a greater variety of substrates is available. However, further investigations into this direction might be very useful.

However, the occurrance of p-electron magnetism in these materials clearly distinguishes them from the transition-metal pnictides and chalcogenides ([71, 68, 72]) where the transition metals carry the magnetic moments. In the present systems the magnetic moments appear in the anion p-band, and therefore makes them a new and technologically challenging research area.
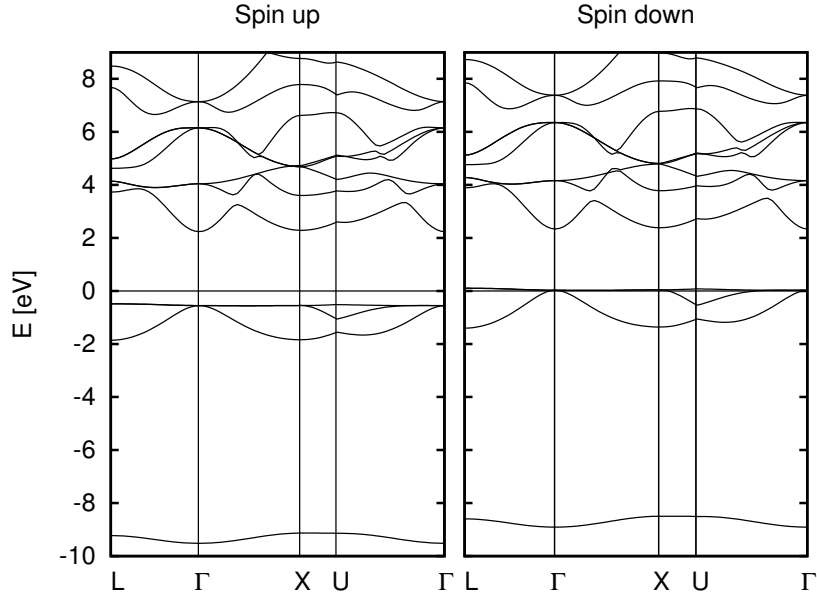
Figure 4.3: Band structure of ZB-CaAs for both spin channels.

4.2 Magnetism in II-V zinc-blende compounds

In the following detailed investigation we present our results for the ZB structure, however, due to their close similarity an equivalent behavior can be expected for the respective compounds in the WZ structure. The half metallic ferromagnets ZB-CaX with X=P, As and Sb exhibit a magnetic moment of 1 μ_B, caused by a curious, almost dispersionless band (see fig. 4.3) [58]. The band structure for CaAs (a_0=12.86 bohr) is shown in fig. 4.3, the site and orbital projected density of states (DOS) is given in fig. 4.4. It has been argued that the reason for this flat band is a mixing of Ca t_{2g} and As-p like states, and that the flat band is essential for the HMF. In order to study the mechanism behind this phenomenon and to explore other candidates for half metallicity several other combinations of group II elements with group V elements have been investigated, table 4.2 lists the results for the ground states and the respective equilibrium lattice constants a_0. For the half metallic compounds investigated here, a_0 varies in a wide range between 9.15 bohr for MgN to 15.37 bohr for BaSb. Compared to conventional ZB III-V semiconductors with values up to 12.25 bohr (CdTe), the II-V compounds tend towards large interatomic spacings, which can be attributed to the comparably big cations. Thus the lighter representatives such as MgN or CaN having lattice constants in a physically reasonable range, might be of great technological importance and will warrant further experimental investigation.
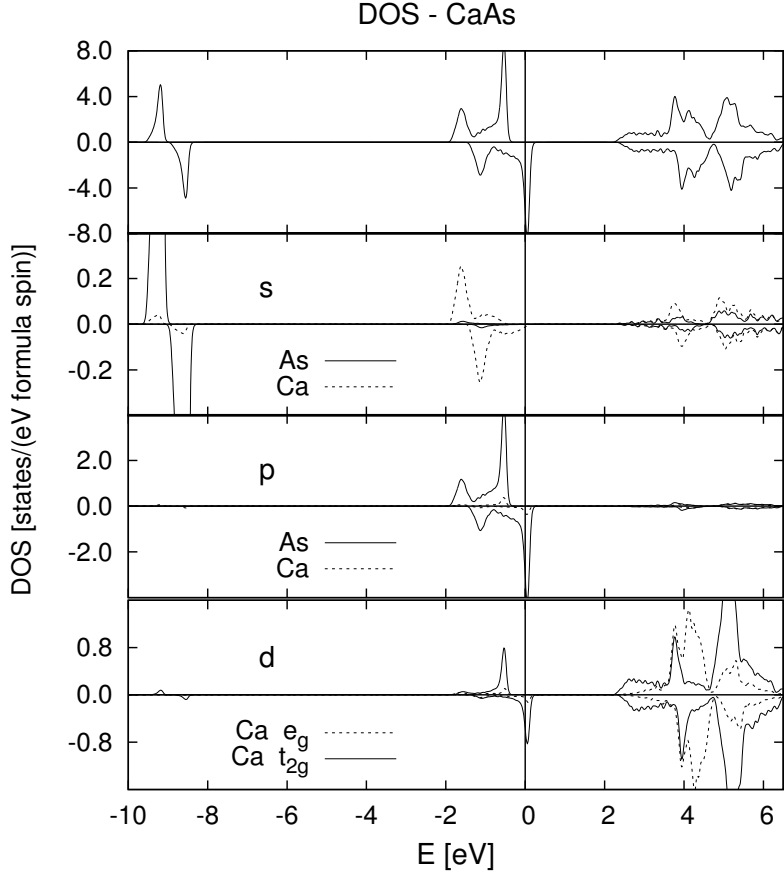
Figure 4.4: Orbital and symmetry projected DOS of ZB-CaAs. The main contribution at E_F comes from As-p with a small admixture from Ca-d (t_{2g}) and Ca-p.

4.3   The origin of magnetism

As expected, all HMF compounds investigated exhibit a magnetic moment M of 1 μ_B per formula unit. This integer value comes about because for the majority spin direction the Fermi energy E_F is situated within a gap, which means that the bands below are occupied by an integer number of spin-up electrons. Since the total number of electrons is integer as well, a resulting magnetic moment has to be integer, too. The magnitude of the magnetic moment can be determined by the $|(8\text{-n})|$ rule, where n denotes the total number of valence electrons per formula unit. In other words, the rather localized anion p-band is completely filled with the exception of one hole, which is responsible for the magnetic moment of 1 μ_B. Comparing tables 4.3 and 4.2, one finds a clear correlation between the DOS at E_F and the ground state of the corresponding compound. A high DOS at the Fermi energy –

Table 4.2: Left part: Ground state calculated at the equilibrium lattice constants a_0 for several II-V compounds in the ZB structure. '+' denotes a half metallic, '-' a non-magnetic metallic ground state and 'm' a system at the verge of a magnetic state. Right part: equilibrium lattice constants (given for an fcc unit cell containing four formula units) for the various systems investigated.

It is remarkable how widespread HMF is found within this class of compounds. All representatives having Ca, Sr or Ba as cations exhibit HMF, additionally also MgN. All have in common that their band structure exhibits a gap separating the anion- and the cation-states. This feature is different for the 3d pnictides where the gap appears only in the minority states, an asymmetry which is caused by the large exchange splitting of the d bands [35].

	ground state				lattice constant a_0 [bohr]			
	N	P	As	Sb	N	P	As	Sb
Be	-	-	-	-	7.49	9.38	9.82	10.69
Mg	+	m	m	-	9.15	11.16	11.54	12.45
Ca	+	+	+	+	10.57	12.45	12.86	13.71
Sr	+	+	+	+	11.34	13.29	13.62	14.55
Ba	+	+	+	+	12.20	14.11	14.43	15.37

Table 4.3: DOS at E_F assuming a hypothetical non-magnetic state.

	$N(E_F)$ states/(eV f.u.)			
	N	P	As	Sb
Be	1.30	1.16	1.17	1.19
Mg	3.47	2.39	2.28	1.10
Ca	5.30	5.52	5.38	5.17
Sr	5.10	5.64	5.70	5.79
Ba	4.52	5.23	5.55	5.64

in these compounds created by a narrow anion p-band – appears to be sufficient to cause an instability of the non-magnetic state within the framework of the Stoner criterion. The application of this criterion is justified because in the non-magnetic state, all these compounds are good metals. However, the criterion itself does not say anything about the type of magnetism which might appear in the magnetically ordered equilibrium state. In the present case the magnetic state is, however, not an itinerant electron state but rather
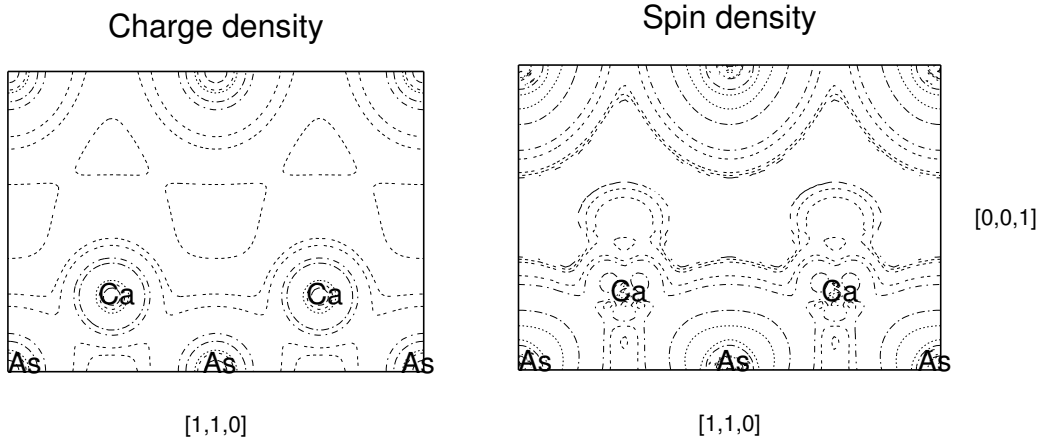
Charge density

Spin density

[0,0,1]

[1,1,0]

[1,1,0]

Figure 4.5: Charge and spin density of CaAs in the ZB structure within the [1,1,0] plane in the fcc cell.

a localized one where the unpaired spins are located in well defined orbitals. The flat band magnetism appearing in this class of compounds can be seen as the magnetism of unpaired electrons occupying an atomic like state, which in the language of band structure appears as a flat (undispersed) band. The resulting magnetic band splitting is much larger that the respective band width, which is a typical sign for a well localized magnetic moment.

MgP and MgAs ($M \approx 0.08$ and 0.02 $\mu_B/f.u.$) are the boarderline cases where the DOS value is on the verge to produce a spin splitting, which is smaller than the width of the p-band, so that in the magnetic state both spin channels have a nonvanishing DOS at E_F. These systems are typical for itinerant electron magnetism with small magnetic moments and a magnetic band splitting which is smaller than the respective band width. For all II/V compounds investigated the magnetic moment can be attributed mainly to the anion (0.6 to 0.8 $\mu_B/$atom), the cation plays only a minor role. The cation moment is always aligned parallel to that of the anion and always smaller than 0.1 $\mu_B/$atom. The relatively large contribution of the interstitial region to magnetism is typically for a structure with large voids. A plot of the charge and spin density of CaAs is shown in fig. 4.5. The spin density is well localized at the As site, whereas everywhere else only a small diffuse induced spin-density occurs. The mechanism for this parallel alignment between the anion- and the cation-moment can be understood in terms of the model of covalent polarization [23]. The cation states mix weakly with the flat anion p-band, which is spin split and almost of equal shape in both spin channels. As the hybridization is of similar strength for both spin directions, the cation has less occupied states in the spin down channel, which results in a parallel polarization of the latter. This becomes evident by inspecting the orbital-projected

53

DOS in fig. 4.4: there are fewer Ca-d states below E_F in the minority than in the majority direction.

Recapitulating, two simple conditions have to be fullfilled in order to have HMF present in the ZB structure, i) there must exist a gap between anion and cation states and ii) the band at the Fermi energy must be flat. In this case the spin splitting will automatically shift the majority states below E_F and create HMF.

4.3.1   Volume dependence of HMF

Since the cell volume controls the dispersion of the electronic bands it has probably the largest influence on the formation of HMF. Fig. 4.6 compares the magnetic moment, the energy gap and the bandwidth along the path L-Γ-X-U-Γ for CaAs and BeN versus the fcc lattice constant a. CaAs has been chosen as a typical representative of the heavier compounds, while BeN is nonmagnetic and the lightest system investigated. The magnetic moment of CaAs is surprisingly stable, it retains its integer value down to a cell volume of 58 % from its equilibrium. BeN on the contrary becomes half metallic only if the cell volume is increased by 62 %, a volume change which is probably beyond physical realizability. This behavior is not surprising as it also has been found among the 3d-pnictides, e.g. in CrAs [73]. For BeN the bandwidth of the anion p-like band at E_F is reduced with increasing interatomic separation, which explains the HMF state appearing at $a \approx 8.8$ bohr. The trend is the same for CaAs, which, however, has an initially much smaller bandwidth.

The behavior of the electronic gap has been studied, too. Coming from large volumes it first increases due to the repulsion of anion and cation states. This effect becomes increasingly reduced (BeN) or even overcompensated (CaAs) by the broadening of the bands forming the gap. The gap values plotted represent the smallest value along the path L-Γ-X-U-Γ, irrespectively whether they were due to a direct or an indirect gap.

4.3.2   Ionicity

Another quantity that plays an important role for magnetism is the ionicity of the compound. This can be seen best if one investigates the non-magnetic to magnetic transition by a stepwise increase of the anion-electronegativity, e.g. in the series MgX with X=As, P and N. Even though the cell volume is smallest for MgN, it is the only magnetic compound in this series. This behavior is due to the stronger localization of the N 2p states compared to the P 3p states. In fig. 4.7 the site and symmetry projected DOS for MgP and MgN is compared. In both cases the admixture of cation states at E_F is negligible, but there is a difference in the shape of the anion p-orbital, resulting in a clearly higher DOS at E_F for MgN.
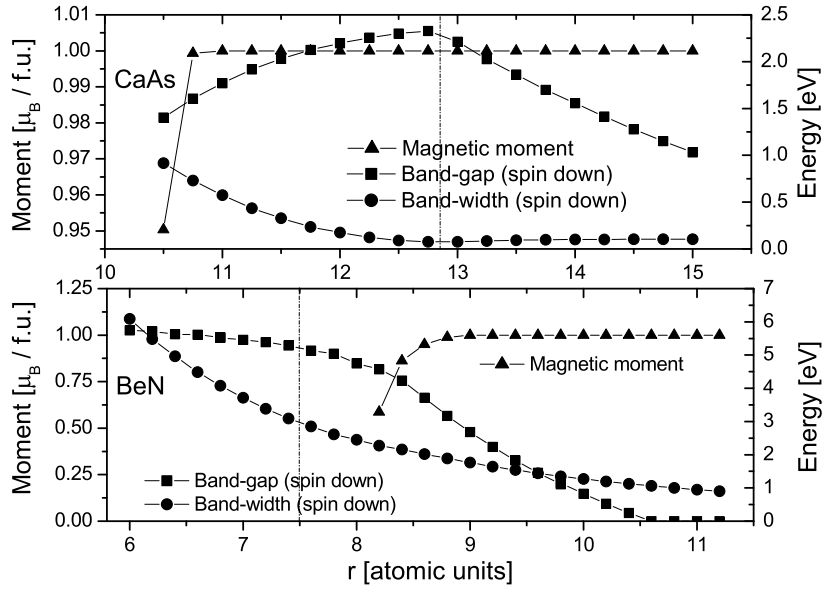
Figure 4.6: Comparison of the magnetic moment, the width of the gap and the maximum bandwidth of the anion p-like band along the path L-Γ-X-U-Γ for CaAs and BeN. The vertical line marks the equilibrium lattice constant.

Table 4.4: Energy gap in eV (d ... direct, i ... indirect), for magnetic members '+' denotes spin up and '-' spin down.

	Energy gap [eV]			
	N	P	As	Sb
Be	8.07/5.32 (d/i)	3.79/1.63 (d/i)	3.69/1.45 (d/i)	2.92/1.26 (d/i)
Mg	3.86/2.82 (+d/-d)	2.61/2.50 (+i/-i)	2.08/2.05 (+d/-d)	1.91 (d)
Ca	3.2/2.17 (+i/-i)	2.96/2.42 (+i/-i)	2.72/2.23 (+i/-i)	2.67/2.26 (i+/-i)
Sr	2.45/1.37 (+i/-i)	2.62/2.10 (+i/-i)	2.27/1.77 (+i/-i)	2.32/1.92 (+i/-1)
Ba	2.13/1.08 (+i/-i)	2.31/1.80 (+i/-i)	2.04/1.56 (+i/-i)	2.09/1.70 (+i/-i)

The ionicity also has an influence on the energy gap. Table 4.4 lists type (direct or indirect) and magnitude of the gap for the II-V compounds investigated. As discussed in the previous section, the gap becomes increasingly smaller for systems with large lattice constants because the energy bands retain their atomic energies due to the weakened repulsion be-
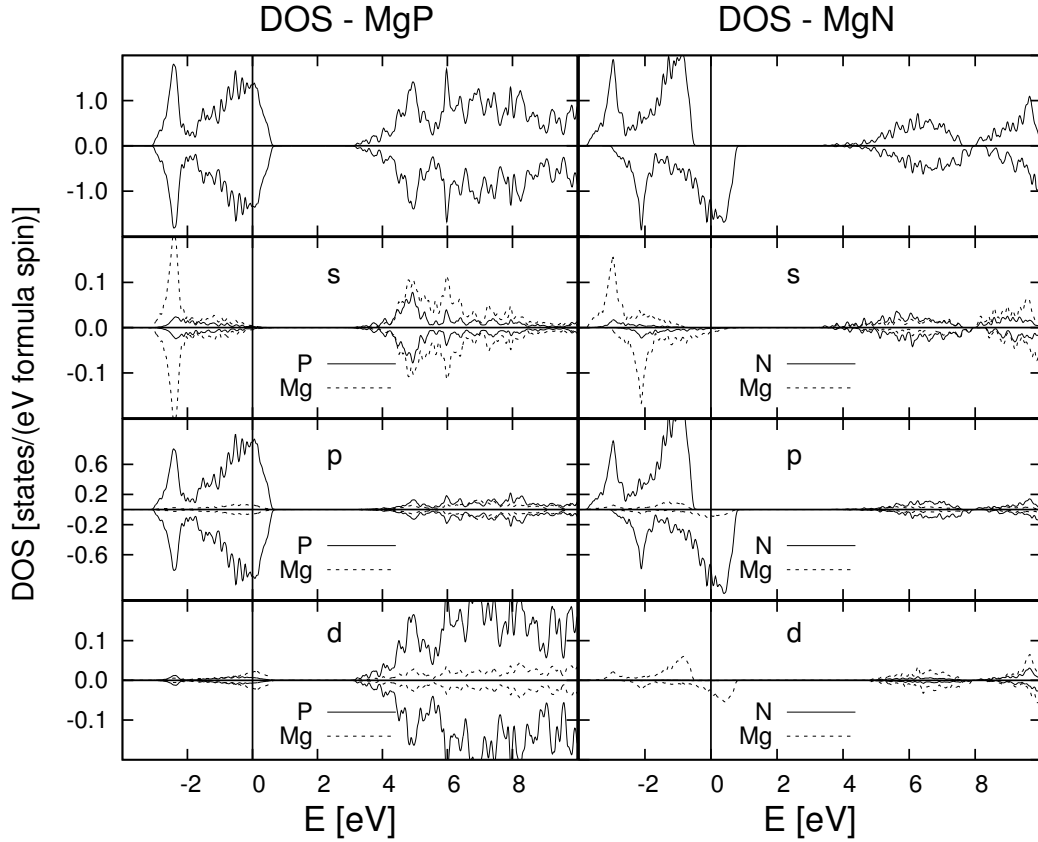
Figure 4.7: Total, site and symmetry projected DOS for MgP and MgN. The muffin tin radii r_{MT} were chosen as touching spheres, r_{MT} for Mg was 2.2 bohr.

tween anion and cation states. The ionicity is thus responsible for the exceptional position of BeN, which has the largest gap of all.

4.3.3 The importance of d-orbitals at the cation

Along the series XAs with X=Ca,Mg and Be, the ionicity varies not so strong as it is the case for MgX discussed at the beginning of the last section. However, there is a clear difference between the bonding in CaAs and MgAs, which cannot be explained by the small volume change (fig. 4.8). These differences in bonding are a consequence of the d-orbitals, which in the case of Ca are energetically close enough to the anion bands for a hybridization to occur. This hybridization leads to an anomalously flat anion p-band near E_F, a more detailled discussion in the scope of a tight binding calculation is given in a later section. Even though these d-orbitals favor this type of flat band magnetism, their
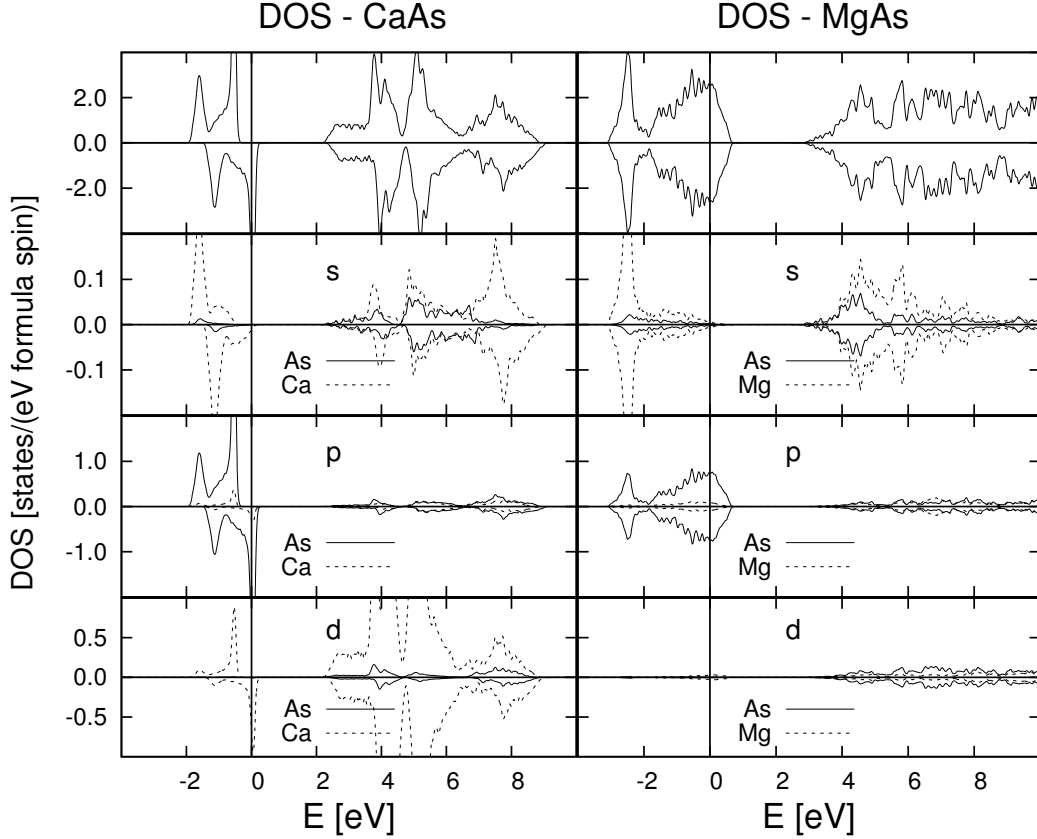
Figure 4.8: Total, site and symmetry projected DOS for CaAs and MgAs.

presence is not conditional for the described mechanism of HMF. For example in the case of MgN, which is a HMF, they play a negligible role. Furthermore, the comparison of the band structure of CaAs and hypothetical fcc As for the same lattice constant, which was first suggested by Kusakabe et al. [58], in fact shows a broader band for fcc As. In addition to the results shown by Kusakabe et al. [58] it should be pointed out, that fcc As at this volume is magnetic anyway. On the other hand, the hybridization with the d-states can induce a magnetic state into compounds that otherwise would become magnetic only at larger, often unphysical lattice constants.

4.3.4 Stability of FM versus AFM order

In order to estimate the stability of the FM against a simple antiferromagnetic (AFM) alignment of the spins, the II-V compounds were investigated in an eight atom cell with cubic primitive lattice vectors and a layer geometry along the [0,0,1] direction. Two an-

Table 4.5: Total energy difference in meV/f.u. between FM and AFM ground state ($\Delta_1 = E_{AFM} - E_{FM}$) and between FM and a hypothetical nonmagnetic state ($\Delta_2 = E_{NM} - E_{FM}$). The resulting values are given as Δ_1/Δ_2

	N	P	As	Sb
Be	0	0	0	0
Mg	114/189	≈ 0	≈ 0	0
Ca	92/222	71/123	70/178	60/80
Sr	96/189	67/118	64/111	58/93
Ba	90/166	56/77	49/71	63/63

ions are situated in the z=0 plane, two in the plane z=a/2, which can be assumed during the calculation to have an antiparallel magnetization. Table 4.5 lists the calculated total energy differences between the non-magnetic (NM), the FM and a possible AFM solution. In all magnetic cases, the FM alignment is most stable, followed by AF and finally by the nonmagnetic solution. In general, the materials containing light elements show higher energy differences, probably because their bonding is more direction-dependent leading to a stronger inter-atomic exchange. Even though the corresponding values for the 3d-metal-pnictides are two or three times larger [71], the results found here are remarkable considering that they come from p-electron exchange.

Motivated by earlier investigations [74] on magnetic stability of fcc alloys we tried to estimate the paramagnetic Curie temperature. To this end we performed spin-spiral calculations [75] employing the Augmented Spherical Wave (ASW) Method [76] for CaAs along two directions in $\mathbf{k}$-space. We find (see fig. 4.9) a smooth variation of the total energy as a function of the spin spiral $\mathbf{q}$-vector with an energy minimum at the FM case $\mathbf{q} = [0, 0, 0]$. The value $\mathbf{q} = [0, 0, 1]$ describes a spin ordering of the AFI type and $\mathbf{q} = [0.5, 0.5, 0.5]$ one of the AFII type. For the definition of AFI and AFII spin ordering in the fcc lattice see ref. [74]. In the mean field approximation the paramagnetic Curie temperature Θ can be written as

$$k_B\Theta = \frac{1}{8}\left(3\Delta E_1 + 4\Delta E_2\right). \qquad (4.1)$$

In equ. 4.1 we assume a spin of $S = 1/2$ ($1\mu_B$) and first nearest neighbor interaction on a anion fcc sublattice only. $\Delta E_1 = E(AFI) - E(FM) = 77$ meV and $\Delta E_2 = E(AFII) - E(FM) = 59$ meV. The resulting paramagnetic Curie temperature amounts to $\Theta = 680K$, which would be a temperature well suited for technological application. The magnitude of ΔE_1 from the ASW calculation is in fair agreement with the FLAPW results. The size
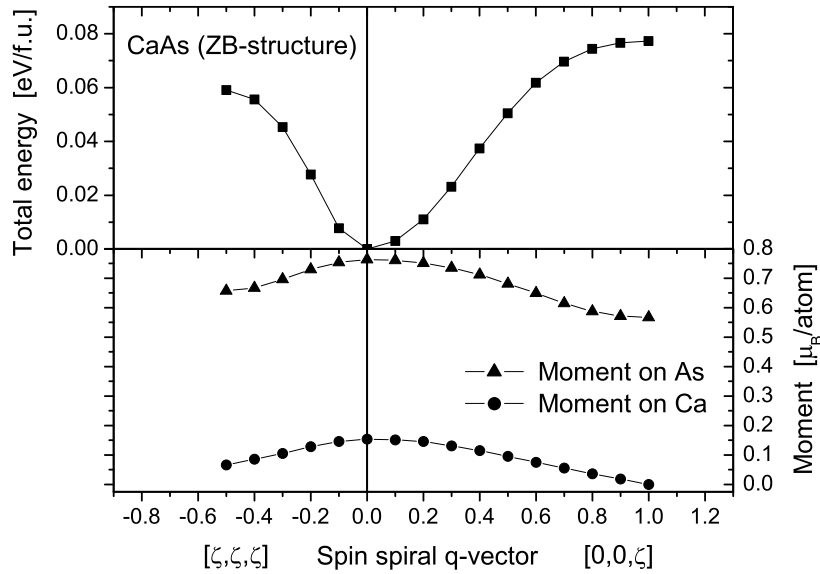
Figure 4.9: Upper panel: total energy as a function of the spin spiral in $[\zeta,\zeta,\zeta]$ and $[0,0,\zeta]$ direction, respectively. The spin spiral propagation vector $\mathbf{q}$ is given in multiples of $2\pi/a$. Lower panel: magnetic moment of Ca and As.

of the magnetic moment (lower panel of fig. 4.9) changes only slightly for different spin propagation vectors, which can be expected for a localized moment.

4.4 ZB compounds containing alkali metals

From the analysis given above one can expect HMF also among I/V compounds if the ZB structure is assumed. Even though no investigation towards their structural stability has been made, some of them have been investigated simply for the sake of interest. In all cases the magnetic moment is 2 μ_B, because there are 2 electrons missing in the anion p-band instead of 1 for the group II elements. Since the alkali s levels are situated at higher energies than those of the alkaline earth elements, the ionicity is slightly increased, thus already NaP is half metallic whereas the analog MgP is not. LiP as well as LiAs are not listed because they are nonmagnetic. The band structure of NaP as a representative can be seen in fig. 4.10. It is analogous to that of the II-V compounds, the high DOS at E_F is again the reason for the occurrance of the spin splitting. All systems listed in table 4.6 exhibit a direct gap at the center of the Brillouin zone Γ.

Table 4.6: Half metallic members among the alkali-pnictides in the ZB structure. Listed are the optimized lattice constant a_0, the bulk modulus B, the magnetic moment per f.u. $M/f.u.$, the width of the gap along L-Γ-X-U-Γ for spin up/down channel, the magnetic band splitting E_m and the energy difference $\Delta_1 = E_{AFM} - E_{FM}$ and $\Delta_2 = E_{NM} - E_{FM}$ per f.u.

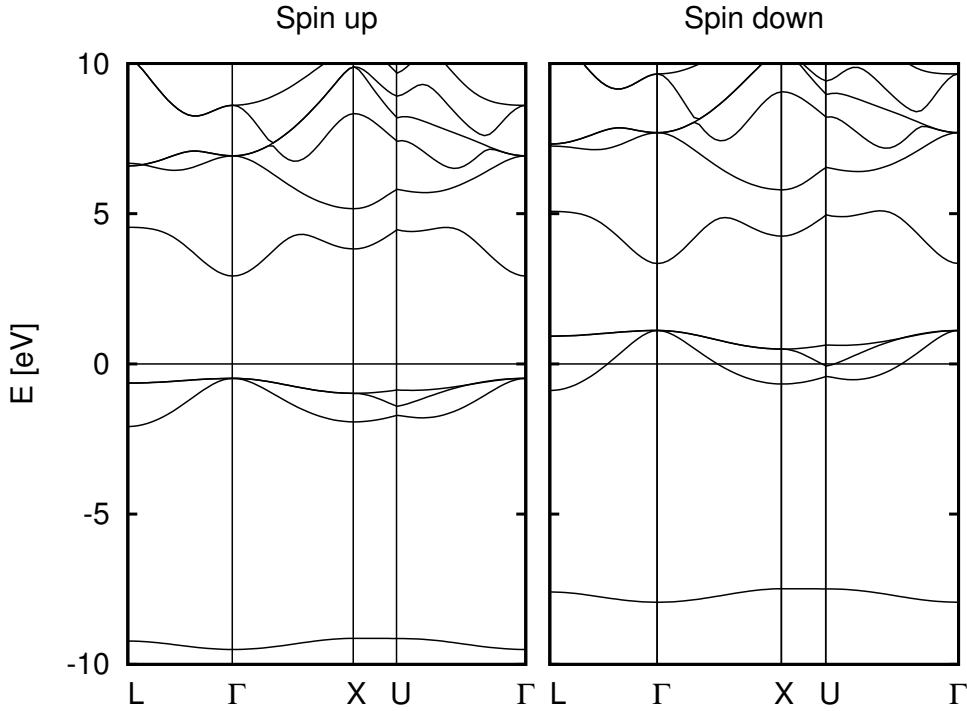|	KAs	KP	NaAs	NaP	LiN
a_0 [bohr]	14.87	14.57	12.91	12.58	8.86
B [GPa]	8.6	8.9	11.0	12.0	38.2
$M/f.u.$ [μ_B]	2	2	2	2	2
Gap [eV]	2.81/1.76	3.21/2.08	2.8/1.6	3.4/2.23	6.77/4.68
E_m [eV]	1.33	1.44	1.41	1.54	2.66
Δ_1/Δ_2 [meV]	107/514	96/582	102/248	119/345	212/688

Figure 4.10: Bandstructure of NaP

4.5 The flat band

The so-called flat-band responsible for the instability towards magnetic ordering is mainly anion p-like and located around E_F. Symmetry considerations allow to draw some con-

Table 4.7: Tight binding parameters for CaAs given in units of eV.

	V(ss)	V(sp)	V(pp σ)	V(pp π)	V(sd)	V(pd σ)	V(pd π)
As-Ca	-0.37	0.48	1.42	-0.35	-0.55	-1.03	0.48
Ca-As		0.97					
Ca-Ca	-0.16	0.21	0.37	-0.09			
As-As	-0.012	0.09	0.16	-0.04			
on-site	As(s)	As(p)	Ca(s)	Ca(d)	Ca(p)		
energy	-8.3	0.65	3.8	4.0	10.0		

clusions already in advance. The center of the Brillouin zone, Γ, has the full symmetry of the crystal $T_d(\overline{4}3m)$ and hence only mixing between As p and Ca t_{2g} states belonging to the same representation T_2 occurs. Along the direction Λ (Γ to L) symmetry reduces to 3m, and one p-band splits off towards lower energies due to s-p_z and p_z-p_z hybridization creating a second peak in the DOS at approximately -1.6 eV (spin up) (see e.g. figure 4.3). A further lifting of the remaining degeneracy in the p-band close to E_F occurs, e.g. at U (mm2 symmetry), where p_y-d_{yz}, p_x-d_{xz}, and p_z-s-e_g mixing is allowed. For a better understanding of the nature of the flat-band a tight binding (TB) analysis of Slater-Koster type has been performed [77]. Nearest and next nearest neighbor (s,p)-interactions suffice to yield a satisfactory agreement with the DFT FLAPW results, provided that Ca-d states take part in the Ca-As interaction, whereas Ca d-d interactions may be neglected. The TB parameters, i.e. interatomic matrix elements and on-site energies, are given in table 4.7. They were obtained in the following way: Parameters for the next nearest neighbor (s,p)-interaction (As-As and Ca-Ca) were determined from the respective As and Ca fcc DFT FLAPW sub-lattice band-structures calculated at the CaAs lattice constant. The on-site energies have been chosen in accordance to the respective band centers of the CaAs DFT FLAPW band-structure. Analogous to the next nearest neighbor (As-As, Ca-Ca) interactions, all nearest neighbor Ca(s,p)-As(s,p) matrix elements were chosen to correctly reproduce the rather narrow As-s band at $\approx$ -9 eV and the width of the anion p-band. In all cases the ratio between π and σ interactions both for p-p and p-d bonding was set according to Harrison [78]. Concerning the As (s,p)-Ca d interaction, its value could be reduced if Ca d-Ca d interactions are included. These interactions broaden the Ca-d bands and thus also increase the p-d interaction. The TB band structure calculated for the symmetry L-Γ-X-U-Γ containing the five lowest lying bands is shown in the left panel of fig. 4.11 and is in good agreement with the FLAPW results, as already stated above. The other two band structures in fig. 4.11 have been calculated by switching off the d orbitals
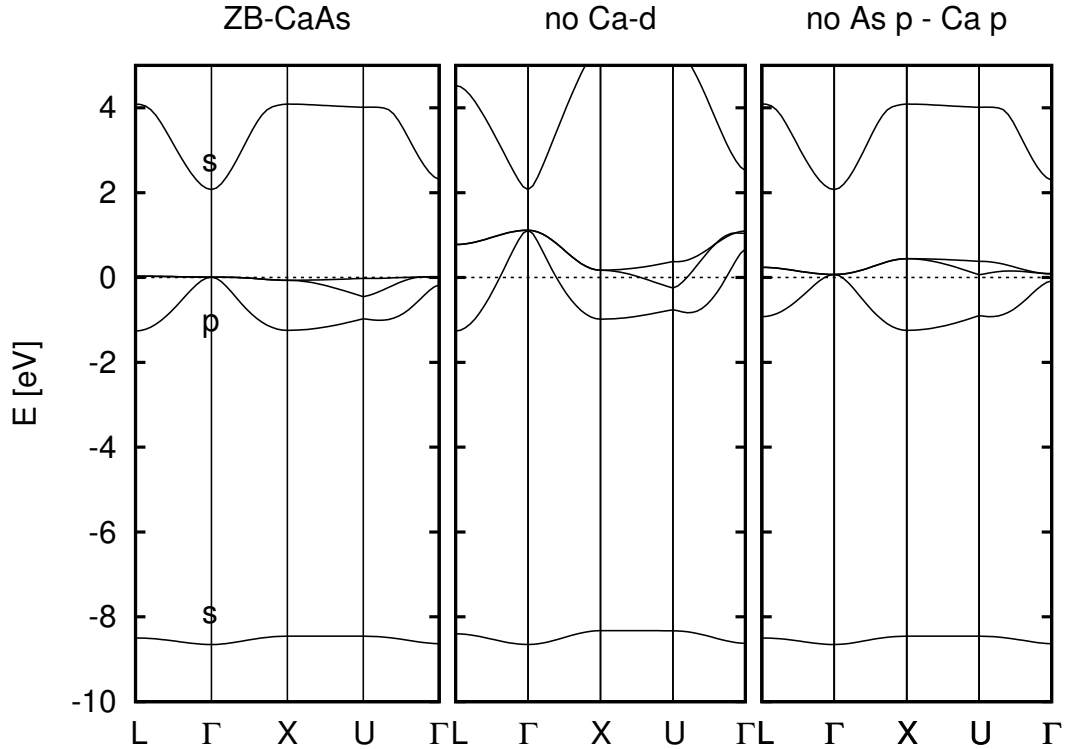
Figure 4.11: Model tight binding (TB) band structure containing the five lowest bands, plotted along the k-points L-Γ-X-U-Γ. Left panel: full TB simulation; center panel: p-d interaction switched off; right panel: p-p interaction switched off.

on Ca and the As p-Ca p mixing, respectively. Quite clearly, the Ca-p As-p interaction generates a dispersion of the flat-band with a trend opposite to the one caused by the Ca-d As-p interaction. For the existence of the magnetically active flat-band, this means that the influences of both interactions cancel each other, rendering one anion p-band dispersionless. The same differences in p-p and p-d interaction also explains the negative curvature of the uppermost p-band at Γ for compounds with mainly or exclusively s-p like interactions (e.g. ordinary semiconductors such as InSb), and the positive one if p-d interaction dominates, as it is the case for some 3d-pnictides like CrAs or MnBi [79, 73] whose minority band structure is at least partially comparable to those of the II/V compounds because all d states are situated well above the gap. Since the magnetism in all these compounds relies on the existence of a flat anion p-band, they might serve as examples for the flat band (ferro-) ferrimagnetism, which has been proposed on the basis of the Hubbard model [80]. Rigorous examples of ferromagnetism (or ferrimagnetism) in the Hubbard

model - at least in the past - have been limited to singular models with infinite Coulomb interaction U [81], or systems in which the magnetization is supported by a nearly flat [82, 83] band (large ratio U/W). Within the Hartree-Fock approximation the Hubbard- and the Stoner-model become equivalent so that the Hubbard U can be determined from the magnetic splitting of the flat band. Given a flat band dispersion of about $W = 0.07$ eV yields the ratio U/W to be about 12, much larger than for ordinary d-electron magnets.

In conclusion it was found that half metallicity is very common among ionic compounds composed of alkaline earth/alkali metals and group V elements if a tetrahedrally coordinated crystal structure like the ZB or WZ structure is assumed. Magnetic order is favored by large lattice constants, high ionicity and empty 3d orbitals present on the cation like in CaAs. The resulting spin splitting yields a half metallic state, because a gap is always present in both spin channels. The origin of ferromagnetic order of these materials depends on the appearance of a flat p-electron band at the Fermi energy in the fully ordered compound. This is in contrast to most other magnetic semiconductors (e.g. Mn doped GaAs, Mn doped Chalcopyrites), where magnetic transition metal impurities are inserted into a semiconductor host. Employing a tight-binding model we show that the flat anion p-band is a property of the crystal structure and its formation depends on the nearest neighbor s-p and p-d interaction. Calculations of the total energy show that this class of materials exists as bulk phases at best in metastable form. However, their highly interesting magnetic properties including a reasonably large Curie temperature might warrant also experimental efforts to stabilize these materials in a fourfold coordinated structure such as ZB or WZ (e.g. via vacuum laser deposition) on suitable substrates.

Chapter 5

Dilute magnetic semiconductors (DMS) based on Cu$_2$O

There is considerable recent interest in the exploration of new, suitable semiconductor hosts as a basis fer new DMS systems. A rather new family, namely the oxide-based diluted magnetic semiconductors are attracting increasing attention, following reports of room temperature ferromagnetism in anatase TiO$_2$ and wurtzite ZnO doped with a range of transition metal ions. In this paper we explore a new suitable host, namely cuprous oxide (Cu$_2$O), which has already been prepared with a small concentration of Mn, Co and Ni on the copper sites. In Mn doped Cu$_2$O the experimental results disagree in the context of room temperature ferromagnetism [84, 85, 86], in the Co doped compound only the results of the group of Kale et al. [87] are available, pointing towards room temperature ferromagnetism if in addition Al codoping is performed. On the theoretical side Ag, Ni and Zn doping has been investigated [88], but magnetic properties were not mentioned. Thus we study Mn, Fe, Co and Ni inserted in Cu$_2$O by the means of density functional theory (GGA and GGA+U) using the VASP code. By setting up 48-atom supercells (2×2×2 fcc cells) as well as 18-atom trigonal cells (simplest trigonal unit cells) with one or two copper atoms being replaced, we are already within the experimental doping regime. Correlations beyond GGA as well as geometrical relaxations around the impurity are taken into account. We analyze energy differences between ferromagnetic and antiferromagnetic coupling of spins situated on the substituents Co and Mn, in order to obtain better insights into the magnetic exchange mechanisms in these compounds.

The calculations were performed using the VASP package [21], which implements a plane wave basis and a projector augmented wave (PAW) technique [20]. Exchange and correlation were treated within the density functional formalism [64] using the generalized gradient approximation of Perdew, Burke and Ernzerhof [65]. Effects of electron correla-

tion beyond GGA were taken into account within the framework of GGA+U. To this end the simplified (rotationally invariant) approach of Dudarev has been used [89]. Since no data from spectroscopic measurements were available, values of U=5 eV and J=0.95 eV have been applied for Mn, Fe, Co and Ni. PAW potentials have been used, with 4s, 3d and 4p electrons in valence for copper and 2s and 2p electrons in valence for oxygen. A plane-wave expansion up to 400 eV was sufficient. For the supercell calculations (48 atoms) a **k**-mesh of 8×8×8 within the full Brillouin zone has been used, only in the cases where symmetry constraints were switched off a 6×6×6 mesh has been utilized. For the trigonal cells a **k**-mesh of 18×18×14 within the full Brillouin zone turned out to yield good results.

5.1   Pure cuprous oxide

Cuprous oxide (Cu_2O) is a p-type semiconducting oxide with a direct band-gap of approximately 2.1 eV [90] that crystallizes in a cubic structure ($Pn\overline{3}m$, No. 224) built up from Cu atoms located on a conventional fcc lattice and oxygens at the positions $(\frac{1}{4},\frac{1}{4},\frac{1}{4})$ and $(\frac{3}{4},\frac{3}{4},\frac{3}{4})$. While the coppers are linearly (twofold) coordinated, the oxygens are situated in the center of ideal tetrahedra (Fig. 5.1). This structure may also be viewed as consisting of two independent and interpenetrating O-Cu-O zig-zag frameworks, each one equivalent to the cristobalite structure. The calculated lattice constant is 8.14 a.u., in good agreement with the experimentally found lattice constant of a_0=8.07 bohr [91]. The calculated gap
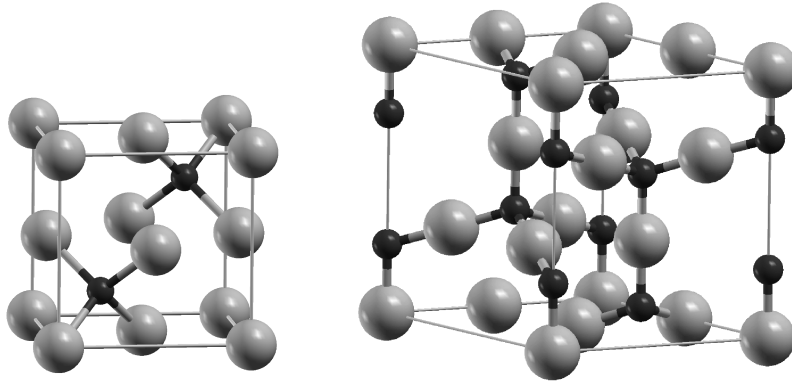

Figure 5.1: Left panel: Cubic unit cell of Cu_2O containing 6 atoms. The big bright spheres are Cu atoms, the small dark ones are oxygens. Right panel: Trigonal unit cell $Cu_{12}O_6$.

is too small (0.48 eV), but otherwise - due to the formally fully occupied 3d shell - one expects band theory to give good results. This has been confirmed by Ghijsen et al. [92] by performing several types of spectroscopies. Laskowski et al. [93] found out that LDA
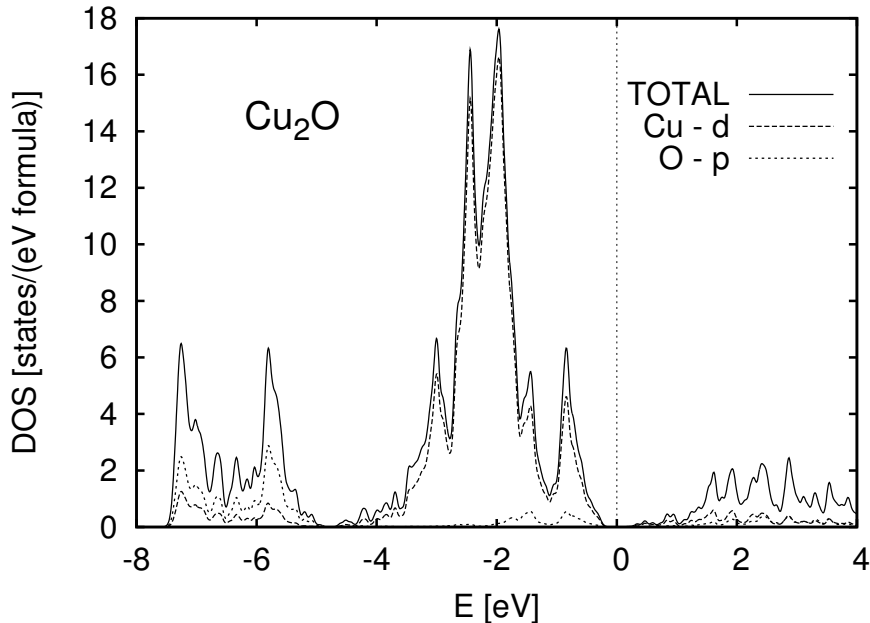
Figure 5.2: Density of states for Cu_2O.

as well as GGA slightly overestimate the s-d hybridization, but this effect can be assumed to play a minor role in the following discussion. The density of states (DOS) of Cu_2O is shown in Fig. 5.2. In addition to the total DOS per formula unit, Cu-d and O-p states are shown. The DOS below E_F has mainly three features, a main Cu d-block situated at $\approx$ -2 eV, a broad oxygen p-peak around $\approx$ -7 eV and one narrow peak at the upper edge of the Cu d-block, which is mainly built up from Cu d_{z^2}, d_{xz} and d_{yz} orbitals. One of the reasons for the stability of Cu_2O is its incompletely filled d_{z^2} orbital. In the Orgel model [94] this is justified by the formation of a s-d_{z^2} hybrid orbital on Cu, resulting in the tendency to occupy Cu s-like states and to emtpy (anti-bonding) Cu d_{z^2} states. More detailed discussions on the electronic structure of Cu_2O can be found e.g. in Ref. [95, 96, 97, 98].

5.2 Transition metal substitution

Experimentally much effort was put into the preparation of transition metal doped Cu_2O. At the moment there is some controversy about room temperature ferromagnetism in Mn doped Cu_2O. Wei et al. [84] reported a T_c of more than 300 K for bulk Cu_2O and thin films if doped with 1.7 % of Mn, whereas Pan et al. [85] identified only paramagnetic behavior. For higher doping (nominal $Cu_{1.9}Mn_{0.1}O$) Ivill et al. [86] reported no magnetic signal except that of a ferromagnetic Mn_3O_4 impurity phase with a T_c of $\approx$ 46 K. Also Co-doped

Table 5.1: Δr_{NN} denotes the changes in the TM-O bond length relative to the pure host, d/d_{ideal} is the relative change of the TM-Cu distance, equivalent to nearest neighbor sites in an fcc lattice.

	Mn	Fe	Co	Ni
U=0, 48 atoms				
Δr_{NN} [%]	+2.5	+0.4	-1.2	+0.5
d/d_{ideal} [%]	-0.74	-1.26	-1.50	-1.11
U=5 eV, 48 atoms				
Δr_{NN} [%]	+5.2	+2.3	+0.6	+2.6
d/d_{ideal} [%]	+1.91	-0.35	-0.12	+1.37

thin films were prepared, room temperature ferromagnetism was indeed reported, but only if 0.5% Al were co-doped [87], otherwise some hints pointing towards spin-glass behavior were found. Ni-doped films were also synthesized [99], but without analyzing their magnetic properties. Even though band-structure calculations for Ag, Ni and Zn doped Cu_2O with a rate of substitution of 12.5 % were done [88], nothing is known about more dilute systems and about magnetism.

5.2.1 Relaxations

In order to be close to experimental doping concentrations, supercells containing 48 atoms (8 fcc cells with 6 atoms each) have been set up, assuming the transition metal (TM) to be located at the origin. This is equivalent to a substitution of 3.125 % of the copper atoms and yields a TM-TM distance of 8.614 Å. For a realistic description of $TM_1Cu_{31}O_{16}$, in VASP all symmetry (D_{3d}) conserving relaxations have been taken into account. The ionic degrees of freedom were converged better than 1 meV, all forces better than at least 0.06 eV/Å. The lattice constant has been fixed at the (GGA) optimized value of the host material (16.28 a.u.), and from now on will be used in all calculations. In Table 5.1 the relative changes in the bond length as compared to the pure Cu_2O host as well as the relative changes in the TM-Cu distance (fcc nearest neighbor sites) are listed. For U=0 all calculations agree that the nearest neighbor relaxations are most important for Mn and Co, but only small for Fe and Ni. In all cases the Cu ions come closer to the substituent and it is found that this relaxation is strongest for Co and Fe. This feature is reasoned by the deviation from the d^{10} configuration, which causes stronger TM-Cu bonds. There is a clear trend towards a strengthening of the bond between TM-O and TM-Cu for both,

Table 5.2: Magnetic moments in μ_B for 3.2% and 9.1% (in brackets) of transition metal (TM) substitution in Cu$_2$O, assuming TM to be situated on the Cu site. Listed are the total and site projected magnetic moments, the radii of integration were chosen to be r=2.5 bohr for TM and r=1.55 bohr for the oxygens (only those closest to the substituent were considered). The upper/lower part of the table is valid for U=0 eV/U=5 eV, respectively.

		Mn	Fe	Co	Ni
Moment (U=0 eV)					
Total	[μ_B/cell]	4.02 (4.05)	3.00 (3.08)	2.00 (2.00)	1.00 (1.00)
on TM	[μ_B/atom]	3.85 (3.73)	2.88 (2.87)	1.89 (1.90)	0.56 (0.57)
on O	[μ_B/atom]	0.01 (0.02)	0.04 (0.04)	0.05 (0.05)	0.02 (0.03)
Moment (U=5 eV)					
Total	[μ_B/cell]	4.34 (4.24)	3.07 (3.18)	2.00 (2.00)	1.00 (1.00)
on TM	[μ_B/atom]	4.40 (4.29)	3.39 (3.28)	2.16 (2.11)	0.78 (0.76)
on O	[μ_B/atom]	-0.01 (0.02)	0.02 (0.01)	0.02 (0.03)	-0.02 (0.01)

U=0 and U=5 eV when going from Mn to Co, but a weakening of the bond for Ni. A finite Hubbard U always leeds to an increase of the bond length, which is a consequence of the localization of the d-states which prevents them from participating in the chemical bond. The fact that the Co-O bond length is shortest can be explained by the approximately half filled d$^{\downarrow}$ shell of Co and will be discussed in the following section.

5.2.2 Ground states for Mn, Fe, Co, and Ni doped Cu$_2$O

In cuprous oxide a substituent (e.g. Co) on the Cu-site has site symmetry D$_{3d}$ ($\bar{3}$m). Thus the d-orbitals can be characterized by two different irreducible representations, namely A$_{1g}$ with d$_{2z^2-x^2-y^2}$ and E$_g$ with (d$_{xy}$, d$_{x^2-y^2}$), respectively (d$_{xz}$, d$_{yz}$) as symmetrized basis functions. These functions are given in a coordinate system with the z-axis pointing towards one of the two nearest neighbor oxygens. Thus we performed not only calculations for cubic TM_1Cu$_{31}$O$_{16}$ but also for equivalent trigonal cells (R$\bar{3}$m, No. 166), having a z-axis pointing along the cubic (1,1,1) direction (see Fig. 5.1). These trigonal cells contain 18 atoms and the orbital projected DOS shown in Fig. 5.3 is useful for understanding the trends in bonding. In all calculations relaxations of the atomic positions were allowed as long as symmetry was not reduced. The results for the magnetic moments determined for low TM concentrations (3.2 %) as well as for high concentrations (9.1%) (given in brackets) are listed in Tab. 5.2.

From the DOS in Fig. 5.3 one can see that for **Mn$_1$Cu$_{11}$O$_6$** the Fermi energy E$_f$ is situated (slightly) within the conduction band for the spin up electrons and within a gap for the spin down electrons. In the spin down channel the peak below E$_f$ is predominantly composed of d$_{z^2}$-like states, with contributions of (d$_{xy}$,d$_{x^2-y^2}$). This peak originally comes from Mn-O anti-bonding states that in pure Cu$_2$O are responsible for the uppermost peak in the Cu-d DOS at the valence band maximum (see Fig. 5.2). These anti-bonding states can be attributed rather to the Mn atom, and in a simple covalent bond picture (Cu$_2$O is not purely ionic) the electron on Mn (d$_{z^2}$) prefers being spin-paired with the electron on oxygen that is in an orbital pointing towards Mn. Hence the d$_{z^2}$ state does not contribute to magnetism, which can be seen in the DOS. Some of the spin-down d$_{z^2}$-like states (including the peak) are occupied and compared to the undoped host the peak is shifted away by intraatomic exchange interactions from the valence band edge to slightly below E$_f$. If the Hubbard U is set to a value of 5 eV, minority (d$_{xy}$,d$_{x^2-y^2}$)-like states are no longer occupied and the number of Mn spin down d$_{z^2}$-like electrons also goes down. The peak itself is slightly shifted upwards. Regarding site-projected charges, within a radius r$_{TM}$ of 2.5 bohr around Mn the number of minority electrons reduces from 0.6 for U=0 to approximately 0.3 for U=5 eV. The total d-like charge within this radius decreases slightly from 4.95 to 4.92 electrons. A Bader charge analysis for the present material using an algorithm of G. Henkelman et al. [100, 101] results in a total charge on Cu of 10.5 (s+d), on O of 7.1 (s+p) and on Mn of 6.1 (s+d) electrons (U=0). In conclusion, the total magnetic moment of $\approx$4 μ_B can be explained by the fact that all orbitals except the d$_{z^2}$ are spin polarized. The minority d$_{z^2}$-like states are emptied if on-site correlations beyond GGA are introduced (e.g. by U), causing an increase of the total and site-projected magnetic moment.

The one additional electron in **Fe$_1$Cu$_{11}$O$_6$** goes into the (d$_{xy}$,d$_{x^2-y^2}$) orbitals, which are non-bonding with respect to the nearest neighbor oxygens. These orbitals spread out within the trigonal z=0 plane. The local coordination of the TM atom within this plane is a hexagon built up from 6 nearest neighbor Cu atoms and another hexagon (rotated by 30° with respect to the Cu hexagon) built up from second nearest neighbor oxygens, alternating above and below the z=0 plane. The magnetic moment is approximately 3 μ_B and changes slightly upon a change in the Fe concentration and moderately upon an increase in U. For the spin-up electrons E$_f$ is situated within the bottom of the conduction band and contrarily to the Mn compound spin-down E$_f$ is situated within the (d$_{xy}$,d$_{x^2-y^2}$)-like states (see Fig. 5.3), broadened by spurious TM-TM interactions due to the limited size of the supercell. The Bader charge for U=0 on Fe is 7.3 (s+d), larger by 1.2 compared to Mn. Also the total d-like charge within r$_{TM}$=2.5 bohr around Fe increases by 1.1 (U=0), indicating that the charge is slightly more localized on the Fe atom than it is on the Mn. When the total DOS of the 48 atom cubic supercells (not shown) is taken into consideration, one

finds that the energetic position of the spin up conduction band is slightly higher in Fe than in Mn doped Cu_2O. If U is set to 5 eV, the spin up conduction bands (for the cases Mn and Fe) are clearly shifted downwards. This is similar to n-type doping, which usually shifts E_f inside the conduction band.

The situation changes significantly if one additional electron is present at the TM site. **$Co_1Cu_{11}O_6$** is the first compound within the series exhibiting a stable integer magnetic moment of 2 μ_B. It has a vanishing DOS at E_f for both spin channels. Compared to the representatives discussed above, in the Co-doped system E_f for spin-up is no longer inside the conduction band. For the other spin channel, the anti-bonding d_{z^2} peak is occupied as well as a second set of orbitals, namely (d_{xy},$d_{x^2-y^2}$). This allows E_f being situated inside a crystal field gap, separating the occupied orbitals from the empty ones that have predominantly (d_{xz},d_{yz}) symmetry. The Bader charge on Co is 8.4 (s+d) (for U=0), by 1.1 electron more than on Fe. This increase relative to the core charge reflects the increase in electronegativity when the d-shell is being filled. The d-like charge within r_{TM} (2.5 bohr) is 7.23, which relative to the core charge is largest among all members of the series. In the previous section about relaxations it was found that the TM-TM and TM-O bond length are smallest for the Co doped compound. This stronger binding may be attributed to E_f falling just inside a gap, which very often is energetically favored. Moreover, the approximately half filled $d^{\downarrow}$ shell is also optimal for binding, because (for spin down) the energetically favored orbitals are occupied whereas the others are still empty. When the Hubbard U is increased, the local moment increases from 1.89 μ_B to 2.16 μ_B, and since the total moment does not change, the neighbors have to contribute antiferromagnetically to the total moment.

The compound **$Ni_1Cu_{11}O_6$** is either half metallic (U=0 eV) with a high DOS at E_f in the spin down channel, or it has no states at E_f in both spin directions (U=5 eV). In both cases the total magnetic moment is integer 1, with a local moment of 0.56 and 0.78 for U=0 and 5 eV, respectively. The Bader charge of Ni for U=0 is 9.5, reflecting the fact that Ni has a similar tendency to fill its d-shell (a similar electronegativity) as Cu with a Bader charge of 10.5 (s+d). The total d-like charge inside r_{TM} is 8.07 (U=0). A more detailled investigation of the DOS shows that for U=0 eV the energetic sequence of d-orbitals has changed compared to the compounds discussed earlier. Energetically lowest are (d_{xy},$d_{x^2-y^2}$), followed by (d_{xz},d_{yz}). The minority spin d_{z^2} peak is situated above E_f for the first time. This might come from the tendency of E_f being situated within a region of vanishing DOS. If the non-degenerate spin-down d_{z^2}-like peak were below E_f as for all the other representatives, the two-fold degenerate set (d_{xz},d_{yz}) would have to be half-filled and E_f would fall into a peak. Only in the Fe compound E_f is situated within a spin-down peak. This is because in that case the larger spin splitting makes a rearrangement of the
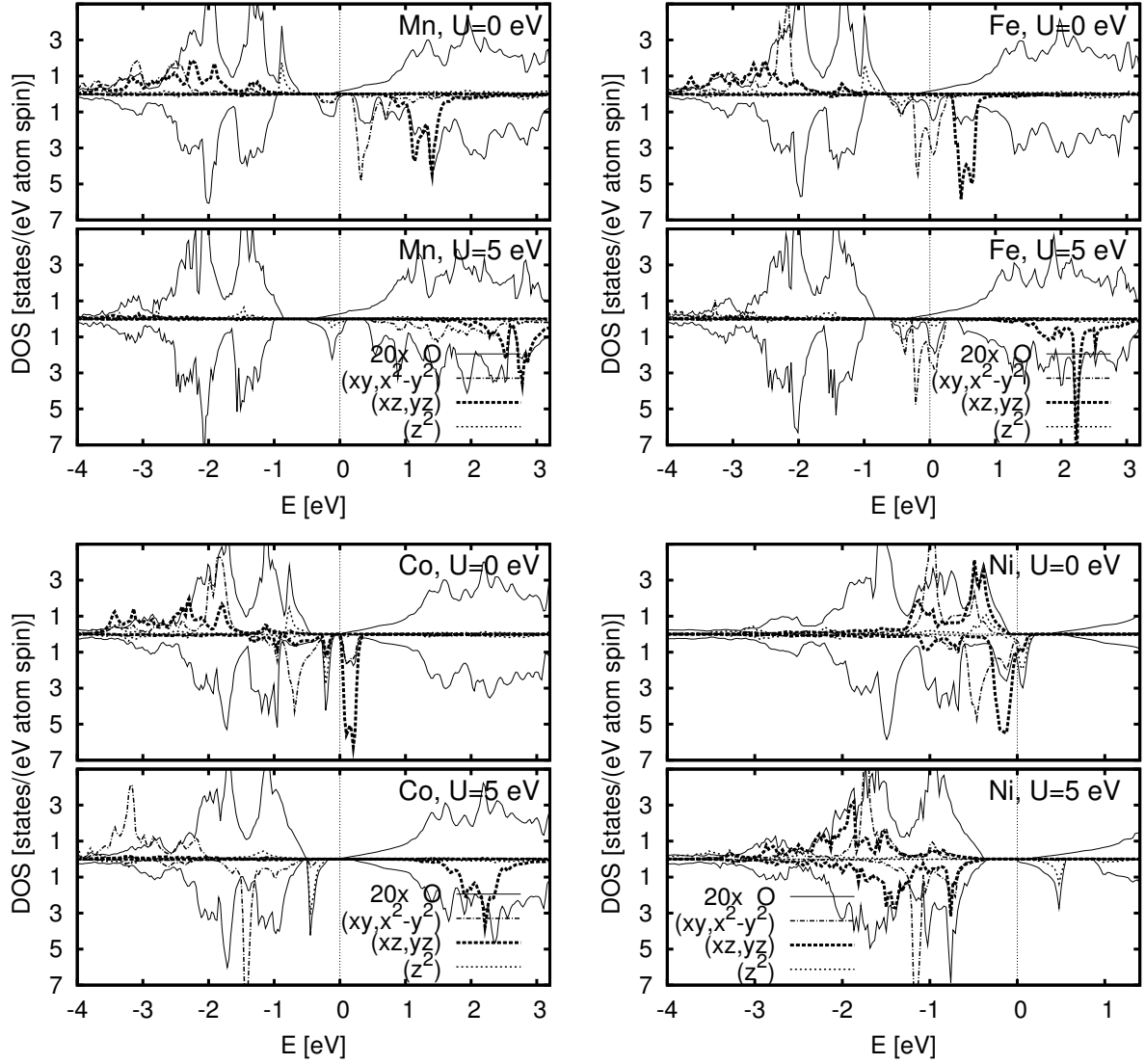
Figure 5.3: Density of states (DOS) for $TM_1Cu_{11}O_6$ with $TM=$Mn (a), Fe (b), Co (c), and Ni (d). The TM d-like DOS (radius of integration: $r_{TM}=2.5$ bohr) is splitted in its irreducible representations, and the total DOS of oxygen (r=1.55 bohr) has been multiplied by 20. One should keep in mind that the main oxygen (bonding) states are situated at energies of about -7 eV. All upper panels display standard DFT results, U=0, while all lower panels show GGA+U results for U=5eV.

spin down orbitals unfavorabale. The Hubbard U further empties the d_{z^2}-like states, most probably due to Coulomb repulsion arising from the occupied (d_{xz},d_{yz}) states.

Regarding structural properties, the contraction of the TM-O bond length when going from the Mn to the Co doped compound might originate from the fact that a half filled $d^{\downarrow}$ shell is favored, since the bonding part is occupied and the unfavored states are empty. The position of E_f within a crystal field gap as in the case of the Co system is also favorable, explaining the exceptional small Co-O bond length. When it comes to the magnetic properties, the earlier members of the series (Mn, Fe) are close to a half metallic state, however, their total magnetic moment depends on the Hubbard U as well as slightly on the TM concentration (see Tab. 5.2). This sensitivity is due to the fact that upon e.g. an increase of U it rather comes to an emptying of minority d-states than to a rearrangement of occupied states as in the case of Co. Since approximately one d-orbital (d_{z^2}) does not contribute to magnetism due to its strong overlap with non spin-polarized oxygen, the total moment for Mn and Fe doped Cu_2O is about 4 and 3 μ_B, respectively. The compounds containing Co and Ni are clearly either half metallic (Co: U=0/5 eV, Ni: U=0 eV) or insulating (Ni, U=5 eV), meaning that there are no states at E_f in either one or even both spin directions. As one would expect, due to the filling of minority d-states on TM the total magnetic moment is 2 and 1 μ_B for Co and Ni doped Cu_2O, respectively. If Cu is substituted by lighter transition metals, the lower electronegativity compared to Cu acts similar as n-type doping. The charge that can not be localized is no longer spin polarized, explaining why for the spin up channel E_f is situated within the conduction band (Mn/Fe). By adding further electrons on TM, E_f then successively moves away from the spin-up conduction band, until it almost reaches the valence band edge in the case of Ni, which has an electronegativity similar to Cu.

5.2.3 Magnetic exchange in Co and Mn doped Cu_2O

In order to investigate the effective magnetic exchange between two substituents, the energy difference between a ferromagnetic (FM) and an antiferromagnetic (AF) spin arrangement for two TM atoms in $TM_2Cu_{30}O_{16}$ (6.7 % doping-rate) has been determined. One TM was put at the origin (0,0,0), the other one was assumed to occupy either the nearest neighbor $(\frac{1}{4},\frac{1}{4},0)$, the second nearest neighbor $(\frac{1}{2},0,0)$, the third nearest neighbor $(\frac{1}{2},\frac{1}{4},\frac{1}{4})$, the fourth nearest neighbor $(\frac{1}{2},\frac{1}{2},0)$, or the fifth nearest neighbor $(\frac{1}{2},\frac{1}{2},\frac{1}{2})$ positions, the fractional coordinates refer to the supercell. Again geometric relaxations were taken into account. In order to analyze possible clustering, the energetically favored spin-arrangement (AF or FM) has been recalculated without any symmetry-related constraints. This improves the total energy predominantly for the nearest neighbor arrangement, typically by several meV.

In the compound $\mathbf{Co_2Cu_{30}O_{16}}$ FM alignment is favored up to the fourth nearest neigh-

Table 5.3: $\Delta E = E_{AF} - E_{FM}$ gives the energy differences in meV between AF and FM arrangement of two spins for interactions up to the fifth neighborshell. The TM-TM distance in multiples of the fcc nearest neighbor distance is given in brackets in the head of the table. Positive values of ΔE indicate FM ordering. The magnetic moments are determined inside a sphere of 2.0 a.u. CE stands for clustering energy, which is the energy of a given atomic arrangement (2nd to 5th nearest neighbor position) relative to the ground state energy of a system with nearest neighbor TM substituents. Negative values indicate that the given configuration is lower in energy than the nearest neighbor reference.

			1st (1)	2nd ($\sqrt{2}$)	3rd ($\sqrt{3}$)	4th (2)	5th ($\sqrt{6}$)
Mn	U=5 eV	ΔE [meV]	-106	-70	-53	-53	-64
		Moment (FM/AF) [μ_B]	4.42/4.38	4.42/4.38	4.36/4.37	4.35/4.35	4.38/4.38
	U=0 eV	ΔE [meV]	-64	-59	-33	-1	-20
		Moment (FM/AF) [μ_B]	3.79/3.85	3.79/3.85	3.83/3.86	3.78/3.85	3.83/3.88
		CE [meV]	-	0	0	+34	+72
Co	U=5 eV	ΔE [meV]	-73	+1	+14	+3	-5
		Moment (FM/AF) [μ_B]	2.13/2.16	2.15/2.16	2.15/2.15	2.16/2.16	2.15/2.16
	U=0 eV	ΔE [meV]	+60	+47	+33	+7	-3
		Moment (FM/AF) [μ_B]	1.87/1.85	1.86/1.87	1.88/1.88	1.90/1.90	1.90/1.90
		CE [meV]	-	+2	+35	+110	+108

bor interaction, only the distant fifth nearest neighbor interaction is weakly antiferromagnetic. An oscillatory behavior is found when correlations are switched on (U=5 eV). Since the on-site Coulomb repulsion directly influences only the local environment around Co, predominantly the shorter interactions are modified towards antiferromagnetic coupling. A very important fact is that the magnetic interactions decay rather rapidly when the distance between the Co substituents is increased, regardless of the strength of U. This suggests that magnetic exchange is not carrier mediated in $Co_2Cu_{30}O_{16}$, which is in good agreement with the DOS discussed in the previous section. The Fermi energy is situated clearly inside the host gap for the majority spin direction and inside a d band-gap for the spin down electrons, which is stable against all values of U investigated. Thus no host states are available at E_F and long range Zener p-d exchange [46] between well localized magnetic moments, mediated by host hole-states, is probably not responsible for magnetic exchange. The values of the clustering energies (CE) suggest that it is most favorable for Co to occupy nearest or next nearest neighbor sites, thus for the real Co doped material rather strong clustering can be expected if produced at too high temperatures where the mobility of the atoms is rather large. A comparison of the local magnetic moments at the
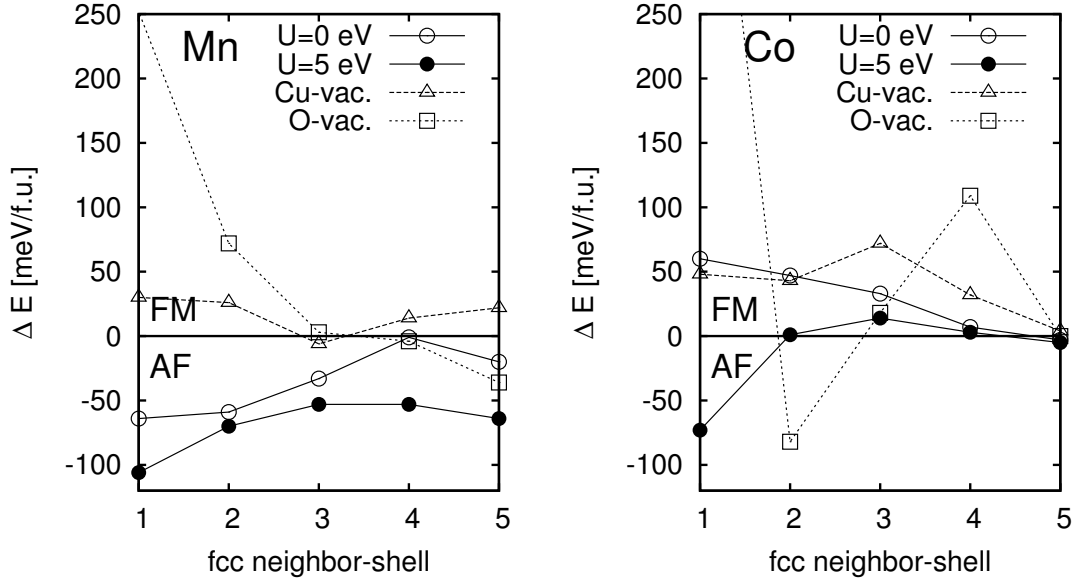
Figure 5.4: Energy difference in meV between AF and FM coupling (E_{AF}-E_{FM}) as a function of fcc neighbor-shell distance. The solid lines show the data for Mn (left hand side) and Co (right hand side) doping of perfect Cu_2O, the dashed lines represent Mn/Co doping of Cu_2O exhibiting intrinsic defects, such as copper vacancies (Cu-vac.) and oxygen vacancies (O-vac.).

substituents for the FM and AF configuration exhibits only minor differences.

In **$Mn_2Cu_{30}O_{16}$** magnetic exchange is exclusively antiferromagnetic for all pairs of substituents investigated. When the Hubbard U is increased, the antiferromagnetic character becomes even stronger. This shows that ferromagnetism, which would be desirable for spintronics applications, is not an intrinsic property of this compound. The strength of the magnetic interactions decays much more slowly with increasing distance than for the Co doped oxide, especially when correlations are introduced. Clustering is less pronounced than in the corresponding Co compound.

Both compounds have in common that there is a continuous change in the exchange constants between nearest neighbors and between impurities more far-off. Since only the nearest and fourth nearest neighbor sites belong to the same Cu-O-Cu zig-zag chain, which allows for a interaction of the substituents via the oxygens, indirect superexchange via the closed shell oxygen is not the only interaction present. This is obvious because the cation sublattice is of fcc type and a deviation from a d^{10} configuration in such a lattice introduces cation-cation bonding without the direct involvement of oxygen. Due to the ongoing discussion about the realizeability of room temperature ferromagnetism in Mn doped cuprous

oxide, we additionally took into account **defects**, which in a semiconductor are expected to play an important role. We assumed single copper as well as oxygen vacancies, the most relevant defects in Cu_2O [102, 103]. For this purpose we removed one atom of our supercell (Cu at $(0,\frac{1}{4},\frac{1}{4})$ or O at $(\frac{1}{8},\frac{1}{8},\frac{1}{8})$) and allowed for a relaxation of all other atoms but with a fixed lattice constant. All calculations were performed applying GGA only (U=0). Our results are shown in Fig. 5.4, presented together with the exchange constants of the defect-free oxide discussed above.

On the left hand side the results for **Mn doped** Cu_2O clearly show that both, copper and oxygen vacancies strongly enhance the FM character of the Mn-Mn interactions. However, while Cu-vacancies cause Mn to couple predominantly FM, except for a small AF 3rd nearest neighbor interaction, the effect of oxygen vacancies is more complex. Even though the removal of oxygen affects magnetic exchange much stronger (e.g. huge Mn-Mn nn interaction of 252 meV), Fig. 5.4 indicates that the Mn-Mn interactions in this case change sign towards AF coupling with increasing $TM\text{-}TM$ separation. Due to the limitation of the supercell size we can only estimate the behavior of Mn-Mn pairs more far off, but further AF interactions can be expected. Thus it is not clear which type of defect is suited best for achieving a T_c as high as possible, however, the important finding is that defects, regardless whether oxygen or copper vacancies, are an important ingredient to stabilize FM Mn-Mn interactions.

In the **Co-doped** system oxygen vacancies again have a much stronger influence on magnetism. While Cu-holes slightly stabilize FM interactions, O-holes induce extremely strong oscillations, which are not desirebale for long range FM. As a consequence, in this system one can expect that Cu-holes, which might appear under Cu-poor preparation conditions, increase the Curie temperature. Contrarily, the lack of oxygen and the resulting short-ranged oscillations in the Co-Co magnetic interaction might be one prerequisite for the spin-glass behavior in Co doped Cu_2O found in experiment [87].

To summarize, cuprous oxide Cu_2O with transition metals substituted on the copper site exhibits a great variety of magnetic ground states. Ni and Co substitution introduces stable integer magnetic moments per cell, and thus results in either insulating (Co, Ni U=5 eV) or half metallic (Ni U=0) ground states. In semi-metallic, defect-free $Mn_2Cu_{30}O_{16}$,independently of U, antiferromagnetic spin arrangement is favored. Long range ferromagnetism might occur when defects (copper or oxygen vacancies) are present. The huge difference between the magnetic properties of perfect and imperfect Cu_2O resolves the discussion about room temperature ferromagnetism, and explains why some groups find long range FM and others not. On the other hand, in insulating defect-free $Co_2Cu_{30}O_{16}$ most of the exchange constants already favor ferromagnetism, only the exchange between nearest

neighbor sites changes towards an AF coupling when the Hubbard U is increased. When defects are taken into account, it turns out that copper vacancies are very likely to increase T_c while a lack of oxygen introduces strong oscillations in the magnetic exchange, favoring a more complex type of ordering. This is in fair agreement with experiment, which even suggests spin-glass behavior in Co doped Cu_2O, if no additional Al-doping is performed. Our calculations further revealed that magnetic interactions are relatively short-ranged in the Co doped system but longer-ranged in the Mn doped compound.

Part III

Metals

Chapter 6

Making metals magnetic

In the previous chapter magnetism in semiconductors was investigated. Now metals are in the center of attention. The interesting question is how to make otherwise non-magnetic materials magnetic. Three examples will be discussed. The first one is $T\mathrm{Cu_3N}$ with T =Pd, Rh and Ru [104]. The host, $\mathrm{Cu_3N}$, serves as non-magnetic cage accommodating well separated 4d elements like Pd, Rh, and Ru. Even though the latter are usually non-magnetic, their large mutual separation within the cage of $\mathrm{Cu_3N}$ significantly reduces the 4d band-width so that for T =Rh and Ru the Stoner criterion for FM is fullfilled. Thus in particular the compound $\mathrm{RhCu_3N}$, which was found to be stable, might be a good candidate for the investigation of possible quantum critical behavior. $\mathrm{AlC}_x\mathrm{Ni_3}$ and $\mathrm{GaC}_x\mathrm{Ni_3}$ with $0 \leq x \leq 1$ belong to the second class of materials studied [105]. These compounds change from a non-magnetic to an almost magnetic ground state upon the removal of carbon. It will be shown that $\mathrm{AlC}_x\mathrm{Ni_3}$ and $\mathrm{GaC}_x\mathrm{Ni_3}$ are non-magnetic in their stoichiometric form ($x = 1$). This was not completely clarified up to now due to uncertainties in the sample characterization. However, when carbon is removed bonds break up and the resulting reduction in the band-width again brings the compound close to or even beyond the Stoner limit. The third class of materials are $\mathrm{Ga}M_4X_8$ with M=Mo, V, Nb, Ta and X=S and Se. They are called Mo-cluster compounds because of their prototype $\mathrm{GaMo_4S_8}$. Their characteristic feature are well-separated, tetrahedral M_4 clusters. In a simple ionic picture one can easily explain their integer magnetic moment of 1 μ_B. After removing those electrons that can be considered as completely transferred to the X p-shell, the remaining electrons on M contribute to a metallic bond within the M_4 cluster. In the case of $\mathrm{GaMo_4S_8}$ ($\mathrm{GaV_4S_8}$) exactly one electron per $\mathrm{Mo_4}$ cluster is missing (present) within the narrow, t_{2g} cluster orbital. This yields a magnetic moment of 1 μ_B per cluster (f.u.). Since the M_4 clusters are well-separated, correlations are believed to play an important role. We show that there are huge differences between the M=Mo,V and the M=Nb,Ta representatives.

It will be demonstrated that the former (M=Mo,V) can correctly be described within plain GGA, if the atomic positions are allowed to relax properly. The role of distortions has been underestimated up to now. We show that in particular the compound $GaMo_4S_8$ is not a Mott insulator as reported elsewhere. Its gap opens up due to cluster-distortions already by using plain GGA, without the need for post-DFT methods like LDA+U that are usually required in the case of a Mott insulator.

6.1 The onset of weak itinerant magnetism in $T\mathrm{Cu_3N}$ ($T =$Pd, Rh and Ru)

Weak itinerant magnetism (WIM) in metallic alloys and compounds has attracted considerable interest over decades since it represents a limiting case, opposite to localized magnetism, providing a background for the development and testing of various spin-fluctuation models [106, 107]. Recently the experimental and theoretical activity in this field was dramatically increased, mainly because of two reasons:

i) It was recognized that weak itinerant magnets are a model class of materials applicable for studying phenomena that come along with the critical fluctuations near the so-called quantum critical point (QCP). The latter may be achieved in these compounds by applying pressure, field or performing suitably chosen chemical substitutions [108, 109].

ii) The giant magnetocaloric effects present in itinerant electron metamagnets [110] make these materials very promising for magnetic refrigeration technology [111].

It is interesting to note that the itinerant metamagnetic scenario [112, 113], case ii), almost always rules out the presence of quantum criticality, case i). It thus appears that a study of materials exhibiting WIM is motivated by the non-trivial interest not only in the character of the critical point but also in the dependence on external parameters. The interest in this field triggered an intensive experimental search for new metallic materials which may be on the border of a magnetic instability. A couple of new metamagnetic materials with very intriguing properties were found. First of all, there are those compounds exhibiting very low critical magnetic fields compared to "conventional" stoichiometric itinerant electron metamagnets (IEM) like $\mathrm{YCo_2}$ [114]. To this group belong the recently discovered $\mathrm{LaCo_9Si_4}$ [115] as well as UCoAl [116]. In addition, giant magnetocaloric and magnetovolume effects were observed in $\mathrm{La(Fe_xSi_{1-x})_{13}}$ [117]. Another example includes non-Fermi liquid behavior in Pd-Ni alloys in a composition range close to the magnetic critical concentration, studied by Nicklas *et al.* [118]. The last examples are more closely related to the compounds we have studied, namely those that are composed of usually non-magnetic metals such as fcc Pd, which is however very close to the onset of magnetic order. Moreover, the probably best studied WIM material is $\mathrm{ZrZn_2}$ [106, 107, 108], which has only non-magnetic metals as constituents. Even though there exist some more examples of that type e.g. $\mathrm{Sc_3In}$ and $\mathrm{VAu_4}$, which for a long time have been regarded as WIM prototypes [106], there is no common route for designing weak itinerant magnetic systems out of usually non-magnetic elements. Thus only a limited number of such compounds is known up to date. In this work we exploit an idea similar to that which nowadays very fruitfully is used to produce strongly correlated materials having unusual magnetic and transport properties, namely that of filled scutterudites. In these materials the cages
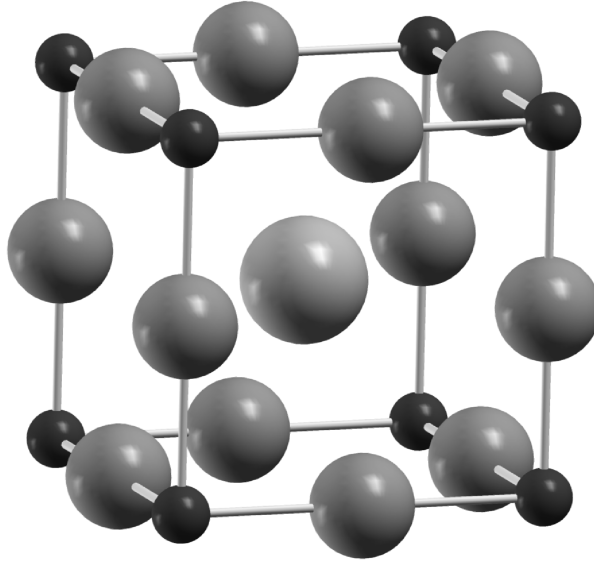
Figure 6.1: Unit cell of $T\mathrm{Cu_3N}$, the small spheres in the corners are nitrogen atoms, the bigger ones situated at the edges are copper atoms and in the center e.g. T=Pd has been added.

created by a network of covalently bound p-elements can be filled with magnetic atoms (usually rare-earth elements [119]) leading to a number of phenomena intensely studied in the last years (see e.g. Ref. [120] for a recent review). As a candidate for filling with a $4d$ metal we chose $\mathrm{Cu_3N}$, which has a rather open crystal structure and rigid, perpendicular Cu-N-Cu covalent bonds (Fig. 6.1). However, most important for our choice has been the earlier experimental evidence [121] for the stability of this structure with Pd incorporated into the $\mathrm{Cu_3N}$ cage. The resulting stoichiometric compound $\mathrm{PdCu_3N}$ (see Fig. 6.1) has antiperovskite crystal structure and a dissociation temperature of approximately 740 K, similar to that of the host [121].

In this work we have performed first principles studies of the electronic structure and the magnetic properties of the series $T\mathrm{Cu_3N}$ with T =Pd, Rh and Ru. In order to estimate the stability of these compounds we calculated their formation energies. It will be shown that both, the Rh and the Ru antiperovskite, become magnetically unstable, however, only $\mathrm{RhCu_3N}$ probably can be stabilized since it has a negative formation energy similarly to $\mathrm{PdCu_3N}$. Moreover, $\mathrm{RhCu_3N}$ is found to be very close to a magnetic critical point, which makes it to an excellent candidate for exhibiting quantum criticality.

Our calculations were performed using the VASP package [21], which implements density functional theory with a plane wave basis and a projector augmented wave (PAW)

Table 6.1: E_H [eV] denotes the formation energy, calculated as the difference between the energy of the ternary compound E_{co} minus the energy E_T of its constituents T (Pd, Rh or Ru) and the energy of pure Cu_3N. Negative values of E_H indicate that the formation of TCu_3N is energetically preferred.

	Cu_3N	$PdCu_3N$	$RhCu_3N$	$RuCu_3N$
E_{co} [eV]	-19.514	-25.516	-26.380	-27.010
E_T [eV]	-	-5.001	-6.675	-9.274
E_H [eV]	-	**-1.001**	**-0.191**	**+1.778**

technique [20]. Exchange and correlation were treated within the local density functional formalism [64], using either LDA (as parameterized by Perdew and Zunger) or GGA (PW91) [65]. A copper potential with *4s*, *3d* and *4p* electrons as valence states and a nitrogen potential with *2s* and *2p* electrons as valence states has been used. A plane-wave expansion up to 400 eV was applied during all calculations. Since the system of interest is metallic and accurate results were required (total energies converged better than 1 meV), a **k**-mesh of 38×38×38 within the full Brillouin zone has been employed.

6.1.1 Results and discussion

Our parent compound is Cu_3N, a narrow gap semiconductor with an open crystal structure (αReO_3, Pm$\bar{3}$m, No. 221) [122]. The calculated lattice constant is 3.83 Å and 3.72 Å within GGA and LDA, respectively. The GGA result is in very good agreement with experiment (a_0 =3.817 Å), but LDA underestimates the lattice constant, a well-known problem which will be discussed in a later section. The cubic unit cell of filled Cu_3N is shown in Fig. 6.1. Pure Cu_3N is built up from nitrogen atoms situated in the corner positions of a cube with copper atoms occupying all 12 edges. While Cu is linearly coordinated by nitrogen, and hence essentially in a valence state +1, N is situated in the center of an ideal octahedron. The unusual Cu(I) state has attracted some interest in the past (see Ref. [123] and references therein). As already mentioned in the introduction, the stoichiometric ternary compound $PdCu_3N$ (see Fig. 6.1), which is obtained when Pd is inserted into Cu_3N, has antiperovskite crystal structure and is stable at room temperature, with a dissociation temperature of approximately 740 K. First-principles calculations on this ternary antiperovskite by Hahn and Weber [124] have shown that the Pd *d*-states only weakly interact with their environment, resulting in semimetallic behavior and an electronic structure that is in principle maintained under Pd doping. From a geometrical

point of view, the voids in Cu_3N (especially the 1b Wyckoff positions) are large enough for the incorporation of Rh or Ru into the structure. However, the situation may be quite different from a simple "rigid" band picture, e.g. due to an increased $3d$-$4d$ hybridization when exchanging Pd by Rh or Ru. Since the question of overall structural stability of $RhCu_3N$ and $RuCu_3N$ is crucial, we first compared the total energy of TCu_3N with that of its constituents Cu_3N and T. Even though this is only a rough estimation, because we do not take into account the maybe more realistic decomposition into bound N_2 and possible alloys of type T_xCu_y, one gains some insight into the relative stability of these compounds compared to that of $PdCu_3N$. The results are listed in Tab. 6.1 and show that indeed most stable is $PdCu_3N$ with a formation energy E_H of approximately -1 eV, followed by $RhCu_3N$ with an E_H of -191 meV. The compound $RuCu_3N$ seems to be unstable due to its strong tendency to separate into metallic Ru and Cu_3N (1.78 eV).

For a better insight into bonding and magnetism in these compounds, the non spin-polarized DOS for Cu_3N and TCu_3N with T = Pd, Rh and Ru is shown in Fig. 6.2. The most significant features in the DOS of Cu_3N are the rather narrow Cu d states at $\sim$ -3 eV, as well as two smaller peaks: one bonding combination between Cu d and N p orbitals at $\sim$ -7 eV and one antibonding combination at $\sim$ -1 eV; The structure of this DOS is very similar to that of other linearly coordinated Cu(I) compounds, e.g. Cu_2O. In $PdCu_3N$ the gap closes and its small DOS at E_F makes this material semi-metallic. Moreover, the Pd d states all seem to be occupied, indicating that Pd is at least close to a d^{10} configuration. This phenomenon has been studied in more detail by Hahn et al. [124]. They found out that there is on the one hand a slight accumulation of negative charge on Pd (-0.1 to -0.4 electrons), giving the bonds some ionic character, and on the other hand there are covalent contributions to bonding carried by s and p states on Cu and Pd (so-called d^{10}-d^{10} bonding). The large formation energy (1 eV) of $PdCu_3N$ might alternatively be explained by the accidental "resonance" between Pd $4d$ states and (mainly) antibonding Cu $3d$ states, creating the peak at -1.9 eV. This resonance is successively reduced in $RhCu_3N$ and in particular in $RuCu_3N$, where a strong broadening of the Cu d bands sets in. This broadening shifts the uppermost parts of the Cu d states above E_F. This decreases the overall stability of $RhCu_3N$ and in particular of $RuCu_3N$, which is no longer stable.

Due to the large T-T distance the $4d$ electrons are expected to interact only weakly with each other, and the DOS shown in the preceeding paragraph indicates that they also weakly interact with the host. Since the Fermi level moves towards a sharp peak in the DOS when replacing Pd by Rh and finally Ru, the Stoner factor is expected to increase, driving the system into the region of magnetic instability. Thus we have calculated the energy as a function of the magnetic moment per formula unit (fixed spin moment calculation
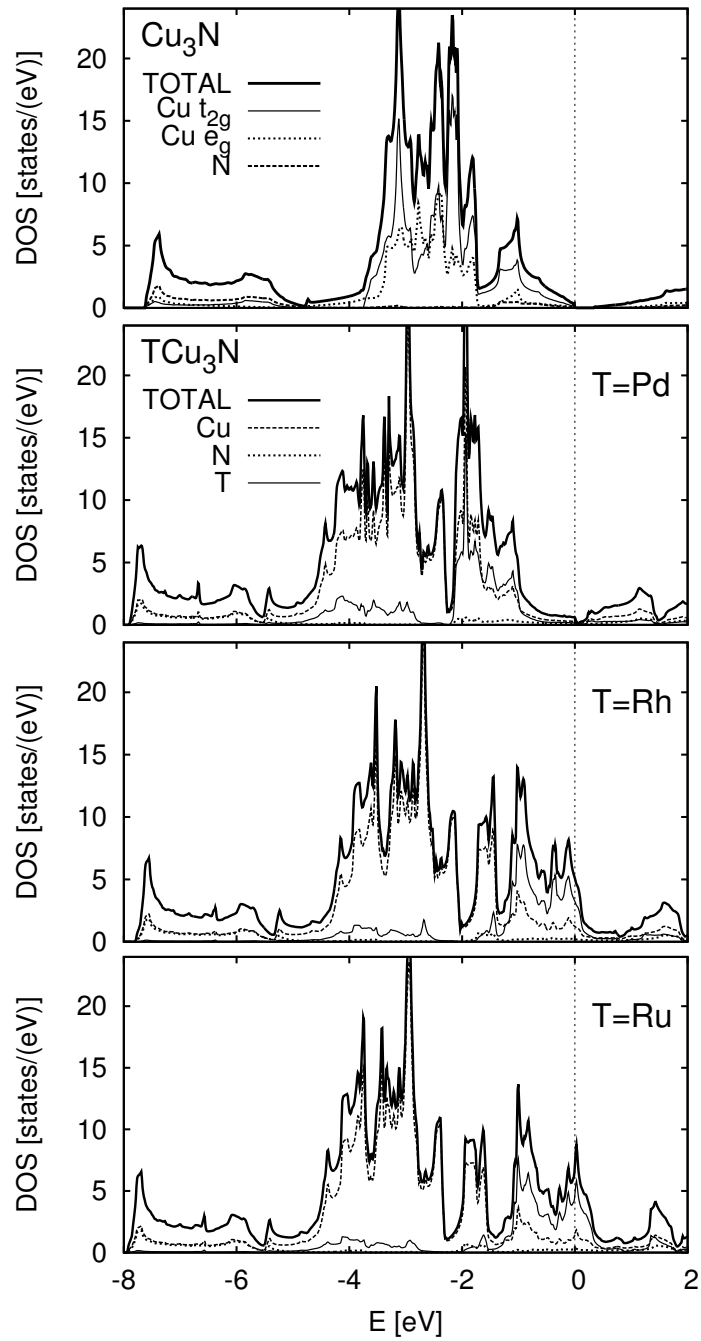
Figure 6.2: Non spin-polarized density of states (DOS) for Cu_3N and TCu_3N with T=Pd, Rh and Ru. While $PdCu_3N$ is semi-metallic, $RhCu_3N$ is close to a Stoner instability (5.12 states/(eV cell)). $RuCu_3N$ has the highest DOS at E_f and thus already a stable magnetic moment.
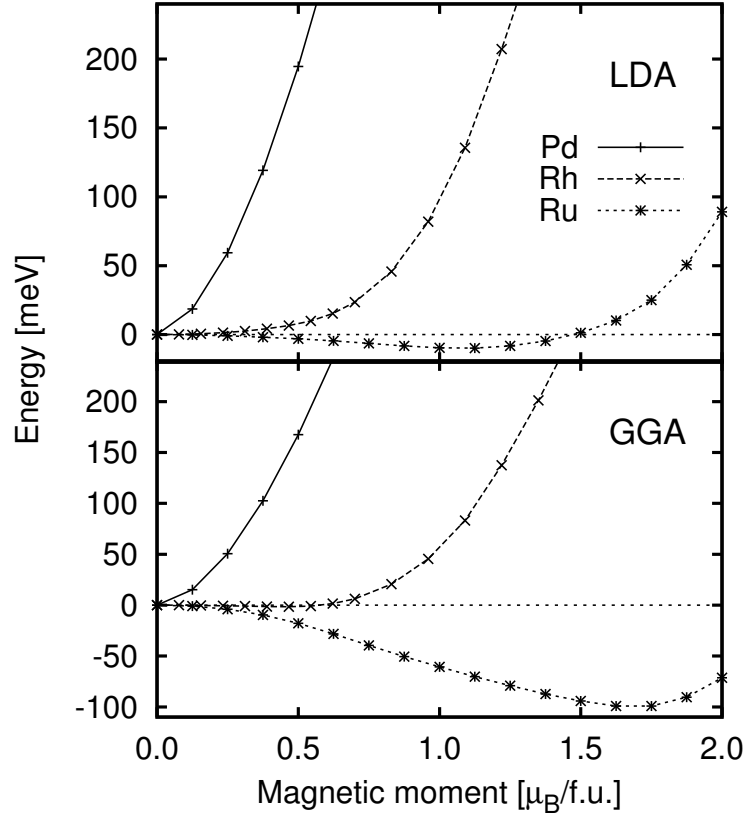
Figure 6.3: Fixed moment calculation of the total energy for the antiperovskites $T\mathrm{Cu_3N}$ with $T =$ Pd, Rh and Ru. The energies are given relative to the non spin-polarized state. In the upper panel LDA results, in the lower one GGA results are plotted.

Table 6.2: This table lists the equilibrium lattice constants a_0, the bulk moduli B (determined via the Murnaghan equation [69]), the magnetic moments per formula unit M/f.u. and per T-site M/T (inside a radius of 2.0 bohr), and the total DOS at E_F N(E_F) in the non spin-polarized state.

	$\mathbf{Cu_3N}$		$\mathbf{PdCu_3N}$		$\mathbf{RhCu_3N}$		$\mathbf{RuCu_3N}$	
	LDA	GGA	LDA	GGA	LDA	GGA	LDA	GGA
a_0 [Å]	3.724	3.833	3.783	3.894	3.768	3.872	3.774	3.885
B [GPa]	148	111	209	155	224	164	216	162
M/f.u. [μ_B]	0	0	0	0	0	0.45	1.04	1.70
M/T [μ_B]	-	-	0	0	0	0.36	0.89	1.46
N(E_F) [states/(eV f.u.)]	0	0	0.07	0.64	4.43	5.11	5.71	6.72

(FSM)), the results are shown in Fig. 6.3. While in PdCu$_3$N the low DOS near E$_F$ makes it energetically unfavorable to split the spin subbands and to create a magnetic moment, the Rh antiperovskite is near to a quantum critical point, and hence an excellent candidate for studying critical behavior. While LDA favors a non-magnetic state, GGA results in a magnetic state with an equilibrium magnetic moment of ≈0.45 μ_B, determined from the minimum in the E vs. M curve. It is remarkable that this minimum is situated energetically only 1.7 meV (≈ 20 K) below the non-magnetic state! For the last member of the series, RuCu$_3$N, the magnetic ground state is favored in both approximations, GGA and LDA, with total magnetic moments of 1.04 μ_B and 1.70 μ_B, respectively. It is worth mentioning that a comparative analysis of LDA and corresponding GGA results is crucial for a metallic system on the border of a magnetic instability. It has been shown for a number of weak itinerant magnetic systems like ZrZn$_2$ [125], MnSi [126], nearly ferromagnetic YCo$_2$ [127], fcc Pd [128], and Ni$_3$Al [129], that GGA always overshoots the values for magnetic moments compared to experiment. In contrast to that, LSDA, on its equilibrium lattice constant, underestimates magnetism and consequently, in the case of NFS, overestimates the values of the metamagnetic critical fields. However, the following empirical rule can be applied when analyzing LSDA calculations for metals: If both, GGA and pure LSDA predict a magnetic ground state at their equilibrium lattice constants, then the system is magnetic. If GGA predicts magnetism and LSDA a nearly ferromagnetic state, then the system is at the border of a magnetic instability (for more details see ref. [130]). This seems to be the case in RhCu$_3$N.

A list of our results (within LDA and GGA) including equilibrium lattice constants, bulk moduli, magnetic moments on the T-site and per formula unit as well as the total DOS at E$_F$ is given in Tab. 6.2. The lattice constants a$_0$ of the antiperovskites are only slightly larger than that of Cu$_3$N, the least change is present when Rh is added to Cu$_3$N (1.1 %), followed by Ru and Pd, which has the largest effect on the lattice spacing (1.6 %). The trend in the bulk moduli for the filled compounds is inverse to that of the lattice constants, hence the Rh compound exhibits the hardest lattice with a bulk modulus of 164 GPa and 224 GPa within GGA and LDA, respectively. The values for the total DOS at E$_F$ in the bottom row of Tab. 6.2 show the increase when Pd is replaced by Rh and Ru. From our FSM calculations we can estimate the value of the Stoner enhancement factor by fitting the free energy E vs. M for RhCu$_3$N (GGA results) with a polynomial expansion $E = E_0 + a_2 M^2 + a_4 M^4$, where a_2 is directly related to the Stoner parameter I_s via $a_2 = 1/N(E_F) - I_s$ [106]. Our fit yields a_2 =-0.027(4) eV and a_4 =0.080(4) eV, and by using the DOS at E$_F$ originating from the Rh d-states N(E$_F$)∼ 1.6 states/(eV spin) one can determine the value of the Stoner integral I_s for Rh. We find a value of about 646(4) meV, which is in rather good agreement with values taken from literature (653 meV [23]).

The small negative value of the parameter a_2 reflects the fact that RhCu$_3$N is close to a magnetic critical point, with a resulting Stoner product $N(E_F) * I_s$ of 1.03.

In conclusion, we have studied the magnetic properties of a new family of ternary nitride antiperovskites, TCu$_3$N, with T = Pd, Rh and Ru. PdCu$_3$N has already been prepared successfully, and our calculations suggest also RhCu$_3$N to be stable, only RuCu$_3$N, however, seems to be energetically unfavorable. Stoichiometric RhCu$_3$N is the most interesting representative investigated because it is found to be close to a magnetic critical point and thus may be an excellent candidate for possible quantum critical behavior.

6.2 The perovskites AlC_xNi_3 and GaC_xNi_3: carbon stoichiometry and magnetism

Since the discovery of superconductivity in $MgCNi_3$ [131] there is great interest in related, isostructural so-called cubic anti-perovskites of the type $TCNi_3$, where T denotes either divalent (Zn) or trivalent (Al, Mg) elements. $ZnCNi_3$ has already been investigated intensively [132, 59], mainly due to its close similarity to the superconductor $MgCNi_3$. However, the situation is different for $AlCNi_3$ and $GaCNi_3$. Even though experimental results have been published, to our knowledge no theoretical investigation on the magnetic properties of $AlCNi_3$ and in particular no theoretical investigation on $GaCNi_3$ has been done. For $GaCNi_3$ Tong *et al.* [133] performed specific heat measurements indicating the presence of strong electron-electron correlations, whereas for $AlCNi_3$, Dong *et al.* [134] did magnetization measurements revealing weak ferromagnetism. Our motivation is not only to investigate the ground states of these compounds, we also want to clarify several unresolved issues found in literature: The lattice constant of $AlCNi_3$ determined by Dong *et al.* [134] is significantly smaller (by 5.6%) than the value reported earlier by Goodenough *et al.* [135], who did systematic studies on this class of compounds. For $GaCNi_3$ Tong *et al.* [133] recently published a lattice constant of 3.6 Å, which curiously is almost identical to the older value of L'Heritier *et al.* for a sample with nominal composition $GaC_{0.1}Ni_3$ [136]. Thus there seems to be a disagreement between old data and some of the new experiments. In DFT calculations Okoye *et al.* [137] reported a rather huge disagreement between their calculated (LDA) lattice constant and the experimental one for $AlCNi_3$ [134]. LDA seems to overestimate the cell volume, which is very unusual. For $ZnCNi_3$ a similar but less pronounced disagreement regarding lattice constants exists. In this context Johannes *et al.* [132] argued that carbon deficiencies could be the reason.

Employing the full potential linearized augmented plane wave (FLAPW) method [17] we perform fixed spin moment (FSM) calculations for $TCNi_3$ with T=Al, Ga, Mg, and Zn in order to probe these systems' response to an external magnetic field. We find that $GaCNi_3$ and $AlCNi_3$ are non-magnetic metals with a low Stoner enhancement factor S and thus far away from a magnetic ground state. This behavior is found within both LDA and GGA. It is important to mention that a comparative analysis between LDA and GGA is crucial for a metallic system at the border of a magnetic instability (for more details see our recent paper [104]). In addition we investigate carbon deficient samples and will show that the lack of carbon leads to an enhancement of the tendency towards magnetism. This is not surprising if one bears in mind that isostructural $AlNi_3$ and $GaNi_3$, which can be obtained from the ternary anti-perovskites by the complete removal of carbon, are close to a ferromagnetic quantum critical point. In order to show the similarities and differences
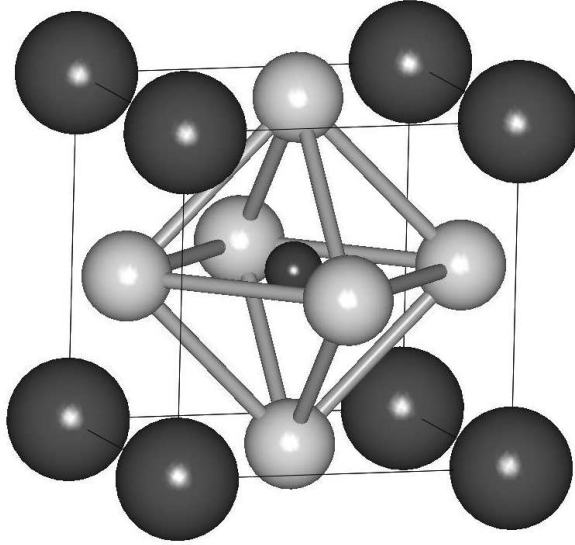
Figure 6.4: Unit cell of the cubic anti-perovskites TCNi$_3$. T is situated in the corner, carbon in the center and Ni occupies the face centers similar to fcc Ni.

between the compounds with and without carbon from the viewpoint of powder X-ray diffraction, we finally discuss theoretical X-ray spectra. With this additional information we have another hint at hand indicating that the tendency towards magnetism found in recent experiments for GaCNi$_3$ and AlCNi$_3$ is an artefact stemming from carbon deficient samples, and that truly stoichiometric ones are not at the border of magnetism. The interesting physical properties of the carbon free compounds AlNi$_3$ and GaNi$_3$, including strong magnetic fluctuations due to the proximity to a ferromagnetic quantum critical point (QCP), make also TCNi$_3$ highly interesting materials. One could for example tune them very slowly towards this QCP by changing the carbon concentration.

The calculations were performed using the FLAIR [18] code, an implementation of the full potential linearized augmented plane wave (FLAPW) method [17]. Exchange and correlation were treated within the local density functional formalism [64] using either the parameterization of Perdew and Zunger (Ceperley Alder) [138, 139] (LDA) or that of Perdew, Burke and Ernzerhof [65](GGA). Potential and charge density were expanded up to $l = 8$ and $G_{\max} = 12$ $a.u.^{-1}$. Inside the muffin tin spheres (r=2.5 bohr for Ga/Al, r=1.4 bohr for carbon, and r=2.05 bohr for Ni) the wave-functions were expanded up to $l = 8$ and a plane-wave cutoff k_{max} of $7/\min(r_{MT})$ was used, where $\min(r_{MT})$ denotes the radius of the smallest muffin-tin sphere in the cell (carbon). A **k**-mesh sampling with at least 120 k-points in the irreducible wedge of the Brillouin zone for lattice optimizations and at
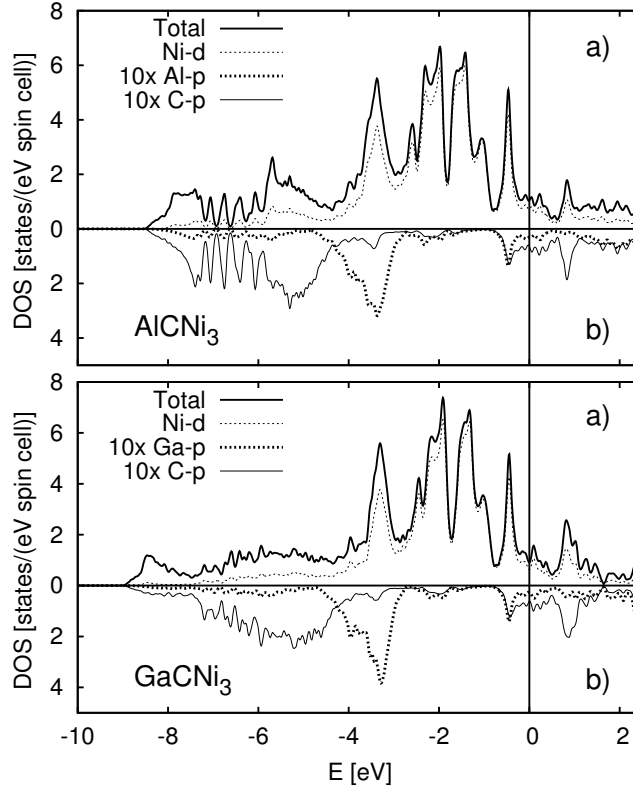
Figure 6.5: Density of states (DOS) for AlCNi$_3$ (top) and GaCNi$_3$ (bottom). In part a), GGA results for the total and Ni-d resolved DOS are shown. In part b) the Al/Ga-p and C-p states multiplied by 10 are plotted.

least 220 irreducible **k**-points for fixed spin moment (FSM) calculations were used.

6.2.1 Results and discussion for AlCNi$_3$ an GaCNi$_3$

The anti-perovskite unit cell of TCNi$_3$ with $T =$Mg, Zn, Al, and Ga contains one formula unit and is shown in Fig.6.4. The T element is situated in the corner of the cube, C in the center, and Ni occupies the face centers. All compounds are metals, and the Ni d-shell is partially filled also if the T-cation is formally trivalent. The density of states (DOS) is plotted in Fig. 6.5. Carbon-p and T-p states have been multiplied by a factor of 10 and are shown in part b) of the corresponding plots. In both materials, E$_F$ is situated in a region with predominantly Ni-d states (mainly (d$_{xz}$,d$_{yz}$) and d$_{x^2-y^2}$), followed by C-p and small contributions of T-p states. The peak below E$_F$, which is responsible for the tendency towards magnetism in ZnCNi$_3$ and especially MgCNi$_3$ [142, 143, 144], has mainly (d$_{xz}$,d$_{yz}$) character. In GaCNi$_3$, the carbon states are situated slightly higher in energy

Table 6.3: Calculated (a_{DFT}) and measured (a_{exp}) lattice constants of the cubic anti-perovskites TCNi$_3$ with T =Mg, Zn, Al, and Ga as well as of AlNi$_3$ and GaNi$_3$, which can be obtained from the former by removing carbon. In brackets theoretical results obtained by other groups are listed.

		MgCNi$_3$	**ZnCNi$_3$**	**AlCNi$_3$**	**GaCNi$_3$**
a_{exp} [Å]		3.81 [131]	3.66 [59], 3.77 [135]	3.587 [134], 3.80 [135]	3.604 [133]
a_{DFT} [Å]	LDA	3.74	3.69 (3.679 [132])	3.70 (3.697 [137])	3.71
	GGA	3.82	3.78	3.78 (3.774[137])	3.79

Table 6.4: Calculated (a_{DFT}) and measured (a_{exp}) lattice constants of the cubic binary compound AlNi$_3$ and GaNi$_3$, obtained from the former by completely removing carbon. In brackets theoretical results obtained by other groups are listed.

		AlNi$_3$	**GaNi$_3$**
a_{exp} [Å]		3.568 [140]	3.576 [140]
a_{DFT} [Å]	LDA	3.47	3.49
	GGA	3.56 (3.574 [141])	3.58 (3.591 [141])

than in the Al compound, and the reduced lattice constant causes the d-states to be slightly narrower ($\approx$70 meV). While in AlCNi$_3$ E$_F$ is situated within a local minimum in LDA and GGA, in GaCNi$_3$ E$_F$ is situated in a local maximim and a local minimum within LDA and GGA, respectively. Nevertheless, the absolute values in all cases are much below the value necessary for magnetic instabilities.

A list of lattice constants for the series TCNi$_3$, obtained via a fit to the Murnaghan equation [69], is given in the tables 6.3 and 6.4. With a_{DFT} we denote theoretical results and with a_{exp} measured ones. AlNi$_3$ and GaNi$_3$ are given on the right hand side of the table. While for MgCNi$_3$ calculated and measured lattice constants are in good agreement (in particular for GGA), already in the case of ZnCNi$_3$ deviations occur. This has already been addressed by Johannes *et al.* [132], who argued that carbon deficiencies might be responsible. Regarding **AlCNi$_3$**, the biggest discrepancy among experimental values has been found. A comparison with AlNi$_3$ shows that the additional carbon in the perovskites unambiguously leads to an increase in the cell volume. Thus it is plausible to compare calculated results with those of Goodenough *et al.* [135], whose lattice constant for AlCNi$_3$ is the bigger one of the two values listed. This value (3.80 Å), however, is in good agreement

Table 6.5: Total DOS ($N^{tot}(E_F)$) as well as total Ni-d DOS ($N^{Ni-d}(E_F)$) (for 3 Ni) at E_F for one spin direction calculated for the ternary anti-perovskites. Listed are further I and S determined via the spin splitting. In the bottom the calculated molar Pauli paramagnetic susceptibility χ [10^{-4}emu/mol] and the calculated γ coefficient of the electronic contribution to the specific heat [mJ/(mol f.u. K^2)] are given.

		MgCNi$_3$		ZnCNi$_3$		AlCNi$_3$		GaCNi$_3$	
		LDA	GGA	LDA	GGA	LDA	GGA	LDA	GGA
$N^{tot}(E_F)$	[states/(eV f.u. spin)]	2.67	2.07	2.18	2.29	0.84	1.04	1.18	0.91
$N^{Ni-d}(E_F)$	[states/(eV Ni-d spin)]	1.97	1.52	1.64	1.72	0.58	0.73	0.82	0.63
I	[eV]	0.99	1.16	1.01	1.17	1.03	1.15	1.01	1.11
S		2.9	2.4	2.2	4.3	1.2	1.4	1.4	1.3
χ^{mol}	[10^{-4} emu/mol]	1.73	1.34	1.41	1.48	0.54	0.67	0.76	0.59
γ	[mJ/(mol f.u. K^2)]	12.6	9.8	10.3	10.8	4.0	4.9	5.6	4.3

with our GGA result, only LDA underestimates the lattice constant more strongly than one would expect. When **GaCNi$_3$** is considered, there is - to our knowledge - only one experimental value available (3.6 Å), which is almost identical to that of L'Heritier *et al.* [136], who give a stoichiometry GaC$_{0.1}$Ni$_3$. Thus we expect the truly stoichiometric compound GaC$_1$Ni$_3$ to have a lattice constant of approximately 3.78(4) Å, close to our GGA result. For the border-compounds AlNi$_3$ and GaNi$_3$, listed in the right hand side of the table, again our GGA calculations yield a cell volume almost identical to the experimental one, whereas LDA calculations as usual underestimate the experimental lattice constants by 2.7 % and 2.4 % for AlNi$_3$ and GaNi$_3$, respectively. These findings clearly show that GGA is much better suited for a proper description of these compounds.

In our DFT-based calculations AlCNi$_3$ and GaCNi$_3$ are clearly non-magnetic at their equilibrium lattice constants in both LDA and GGA. In order to assess whether these compounds are close to magnetism or not we performed fixed spin moment (FSM) calculations, which allow for an estimation of the Stoner enhancement factors S. First we tried to fit the total energy E (in eV) vs. the total magnetization per unit-cell M (in μ_B) via a quadratic function of the form $E = E_0 + aM^2$. This method yields rather unsatisfactory results. For the divalent compounds, T= Zn and Mg, the pre-factor a depends sensitively on the fit interval. For small magnetic moments a is much smaller and the system much closer to magnetism than for large moments. This problem is also present in the compounds with trivalent Al and Ga, even though much weaker. In literature the deviation of $E(M)$ from a quadratic behavior is a well-known problem (e.g. in MgCNi$_3$ [142]) and it can be circumvented by applying extended Stoner theory [145], in which $\tilde{N}(m)$, an average between the

DOS at E_f for spin-up and spin-down electrons is used. However, we used a different and very successful technique, which exploits the spin splitting Δ between spin-up and spin-down states on Ni and the relation $\Delta = M_{loc}I$. M_{loc} (in μ_B) denotes the local magnetic moment inside one Ni muffin tin sphere (r=2.05 a.u.), Δ is the spin splitting given in eV and I is the so-called Stoner I. In this method the DOS at E_F and I are related to one Ni atom. As required for a proper analysis, I turned out to be rather insensitive to the chemical environment, not only among all the ternary compounds but also in comparison to elemental Ni (I_{Ni}=1.18). For all compounds the Ni-d peak situated approximately 0.5 eV below E_F has been used as a reference state for the determination of Δ. In order to get accurate results we averaged $I=\Delta/M_{loc}$ over 10 different values of M_{loc} (for each compound), and M_{loc} was tuned by fixing several values of the total magnetic moment per cell. Finally S was determined via the relation $S=1/(1-N^{1 \times Ni-d}(E_f)I)$, $N^{1 \times Ni-d}(E_f)$ denoting the d-like DOS at E_f attributed to one Ni atom and one spin channel. The results of this analysis are listed in table 6.5. One can easily see that in the compounds with trivalent Al and Ga the Stoner enhancement factor S is even slightly smaller than for T=Mg and Zn, which are known to be non-magnetic. The strong differences between Mg and Zn and between LDA and GGA are due to the proximity of the sharp Ni-peak to E_F. The DOS at E_F is very sensitive to computational approximations (exchange correlation potential, potential and charge density expansion, ..) and hence the results of different groups scatter strongly. Moreover, the error in S is huge when the product NI approaches one. The compounds with T=Al and Ga, however, do not exhibit this sensitivity since they are much further away from a magnetic instability. They all have S values below 1.5. In order to allow for an easier comparison with experiment, we also listed the Sommerfeld constant γ^{th} and the Pauli paramagnetic susceptibility χ_p^{th} for the non-interacting electron gas, given by $\gamma^{th}=\pi^2/3\ k_B^2 N(E_f)$ and $\chi_p^{th} = \mu_B^2 N(E_F)$, N($E_F$) denoting the total DOS at E_F for both spin channels. In experiment Tong $et\ al.$ determined for GaCNi$_3$ a γ value of 30 mJ/(mol K^2) and a χ_p^{th} around 3.9×10^{-3} emu/mol. They estimated N(E_F) to be around 1.6 states/(eV spin unit) resulting in a Stoner enhancement S around 30. This is in disagreement with our calculations showing no signs of magnetic fluctuations. When AlCNi$_3$ is concerned, our N(E_F) is in agreement with calculations made by Okoye $et\ al.$, but weak ferromagnetism as suggested by Dong $et\ al.$ seems to be unlikely, provided that stoichiometric samples are considered.

In conclusion, in the compounds with trivalent elements (Al and Ga) the Fermi energy is well separated from the uppermost Ni-d peak and consequently the DOS at E_F is situated between 0.8 to 1.2 states/(eV cell spin). Since the Stoner I is almost constant (as it should be) also the Stoner enhancement factors S, independently whether the LDA or the much more appropriate GGA approximation is used, are below 1.5.
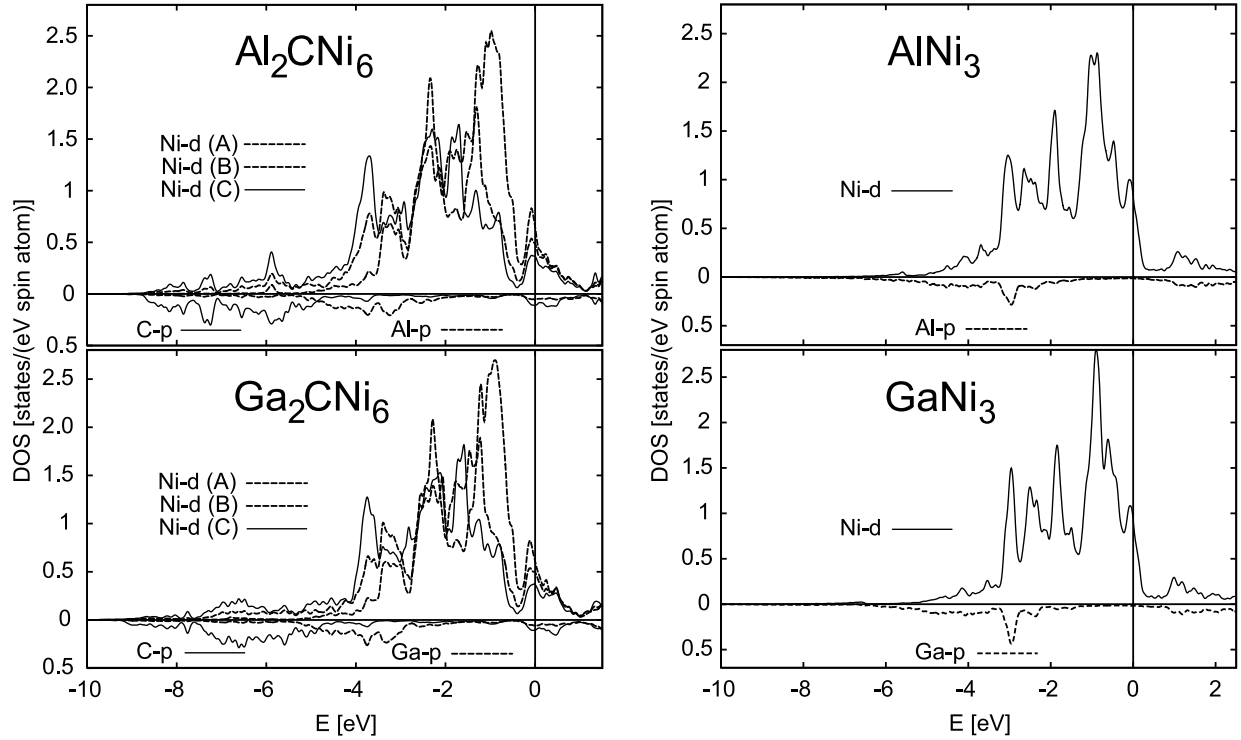
Figure 6.6: Left panel: Total as well as projected DOS for Al_2CNi_6 (top) and Ga_2CNi_6 (bottom). Ni-d sites with no (A), one (B) and two (C) neighrest neighbor carbon sites are splitted, p-states are plotted in the y<0 regime. Right panels: DOS of the compounds $AlNi_3$ and $GaNi_3$, Al/Ga-p states are plotted in the y<0 regime.

6.2.2 The role of carbon in TCNi$_3$

In order to figure out the role of carbon for magnetism we compared the results above with those obtained for T_2CNi_6 (doubled unit cell) and the carbon-free compounds TNi$_3$. It is well known that GaNi$_3$ is an enhanced Pauli paramagnet, whereas AlNi$_3$ is a weak ferromagnet [146, 147]. Both are ferromagnetic in our calculations, but this is a well known problem. The failure of LDA particularly for GaNi$_3$ is due to the unsatisfactory description of spin fluctuations, which are associated with the ferromagnetic quantum critical point (QCP)[147]. These fluctuations are stronger in the Ga compound, and even though (from experiment) AlNi$_3$ is closer to magnetism (actually it is magnetic) than GaNi$_3$, calculations result in the opposite. For the further discussion we will neglect these difficulties since it is only important to realize that in the present case LDA and in particular GGA at their equilibrium lattice constants overestimate but never underestimate the tendency towards magnetism. In Fig. 6.6 one can see easily the increase of the DOS at E_F when carbon is

removed. The lack of one carbon atom in T_2CNi_6 splits the 6 Ni atoms into three groups of 2 members each. Ni of the first type (labeled as A) has no nearest neighbor carbon, Ni of the second type (B) has one nearest neighbor carbon and the third type of Ni (C) has 2 carbon atoms as nearest neighbors. The DOS for type A, B, and C is plotted separately in Fig. 6.6. The lower the number of carbon atoms in the neighborhood of Ni becomes, the higher is the DOS at E_F. This is due to the reduced Ni-C hybridization and the resulting narrowing of the Ni-d bands. We further examined the total DOS at E_F for GaC_xNi_3 with x=1, 0.5, and 0 (GGA results only) by setting up tetragonal super-cells with doubled dimension in z direction. We found out that $N(E_F)$ varies about linearly with the carbon concentration, increasing by about 1.10(2) states/($AlNi_3$ spin) upon a reduction of x by 0.5. On the basis of these considerations we believe that within the series GaC_xNi_3 no magnetism will be found, only strong spin fluctuations are expected close to $x \approx 0$. For AlC_xNi_3 $N(E_F)$ also increases linearly by about 0.89(3) states/($AlNi_3$ spin) when 50% of C are removed. However, since $AlNi_3$ is a weak ferromagnet, also AlC_xNi_3 with x sufficiently close to 0 will be magnetic. In the super-cell calculations described above we neglected relaxations and assumed a linear variation of the lattice constants upon a variation of the carbon concentration. As a reference we used our GGA-based values for $AlNi_3$ and $GaNi_3$ (3.56 Å and 3.58 Å) as well as $AlCNi_3$ and $GaCNi_3$ (3.78 Å and 3.79 Å). These approximations are reasonable and allow us to roughly estimate the carbon concentration of the samples measured in experiment [134, 133], provided that these samples indeed were homogeneous and substoichiometric with respect to carbon. In the case of $GaCNi_3$, Tong *et al.* [133] find a lattice constant of 3.587 Å, which would result in a C concentration of 11 %, if based on our GGA results and the above approximations. However, for a carbon concentration as low as $\approx$ 11 % strong spin fluctuations are plausible due to the proximity to the quantum critical border-compound $GaNi_3$. For $AlCNi_3$ the same analysis results in an estimation of 14 % of carbon in the sample measured in Ref. [134], being a possible explanation why they find weakly itinerant magnetic order.

6.2.3 Powder X-ray diffraction

From the viewpoint of powder X-ray diffraction experiments, Cu_3Au-type TNi_3 and anti-perovskite type $TCNi_3$ are closely related. Both belong to the same space group ($Pm\overline{3}m$) and consequently have the same selection rules for Bragg peaks. Thus we calculated theoretical powder X-ray spectra of $TCNi_3$ and TNi_3 for T=Mg and Al by using the program "Powdercell" [148]. In all simulations we fixed the lattice constant to a value of 3.62 Å. While the differences between the Al and Mg compound are negligible, the presence of carbon is clearly visible and can best be observed by comparing the intensity of the (1 0 0)

and the (1 1 0) peak. Assuming coherent X-ray scattering, the intensity of a certain peak is proportional to the absolute square of the structure factor, which itself is a sum over atomic form factors (assumed to be specific for one atomic species) multiplied with a phase factor. The crucial point is the phase factor of carbon, which changes sign from -1 to +1 when changing from the (1 0 0) to the (1 1 0) peak. Thus the additional presence of carbon will lead to a higher intensity of the (1 0 0) and a reduced intensity of the (1 1 0) peak. For the further discussion we define R as the ratio between these intensities, namely $R = I_{(1\ 0\ 0)}/I_{(1\ 1\ 0)}$. While R is approximately 1.2 and 1.3 for the carbon-free compounds AlNi$_3$ and (hypothetical) MgNi$_3$, respectively, it increases to 3.6 for AlCNi$_3$ and 4.0 for MgCNi$_3$. In other words, the (1 0 0) peak clearly dominates over the (1 1 0) one for the carbon-rich compounds. This trend in R is a useful guideline and could possibly help to evaluate the quality of samples in future experiments, in particular if a comparison to a spectrum of a stoichiometric sample (e.g. MgCNi$_3$) is available.

Applying these results to the X-ray data of Dong *et al.* [134] we find another hint that the AlCNi$_3$ sample might be carbon-deficient. While in the spectrum of MgCNi$_3$, which can be considered as stoichiometric, the (1 0 0) peak is clearly dominant, in the spectrum of AlCNi$_3$ it is not. It has a higher intensity than the (1 1 0) peak, but much less pronounced than one would expect from a comparison to MgCNi$_3$. From the viewpoint of our calculations, R should be similar for AlCNi$_3$ and MgCNi$_3$. Since not stated explicitly in Ref. [134] we have to assume that both measurements were performed on the same equipment. Thus one can directly compare the spectra and deviations between our calculations and the measurements should no longer play a role. A similar analysis for GaCNi$_3$ is much harder because the spectrum presented in Ref. [133] is rather noisy. Moreover, no comparison to a stoichiometric sample (e.g. MgCNi$_3$) is given.

In conclusion, our full-potential DFT calculations employing both, the LDA and GGA approximation, clearly show that stoichiometric AlCNi$_3$ and GaCNi$_3$ in the cubic anti-perovskite structure are non-magnetic metals with a low Stoner enhancement factor and energetically far away from a magnetic ground state. However, the DOS at E$_f$ increases about linearly when the carbon concentration is lowered, strongly enhancing the tendency towards magnetism. A comparison of our calculated lattice constants with some older, experimentally determined ones [135] shows that GGA is much better suited for a proper description of these compounds than LDA. Moreover, a comparison of calculated X-ray spectra for samples with and without carbon shows a change in the relative peak intensity between the (1 0 0) and the (1 1 0) peak, caused by the presence of carbon. In future experiments this could be used to roughly estimate the sample quality. Taking all above results into consideration we also have evidence that some recent measurements on GaCNi$_3$ and AlCNi$_3$ [133, 134] were performed on carbon deficient samples. Both times tendencies

towards magnetism were found, namely strong electron-electron correlations in $GaCNi_3$ and weak ferromagnetism in $AlCNi_3$, which clearly were absent in our calculations. In future experimental work it is important to put great emphasis on the correct carbon stoichiometry. A controlled reduction of x in TC_xNi_3 with T=Al and Ga would be desireable, in particular due to the interesting physical properties at $x \approx 0$.

6.3 The importance of cluster-distortions in the tetrahedral cluster compounds: Ab initio investigations

In this section we study the structural properties of selected representatives of the so-called Molybdenum cluster compounds. Belonging to this family are GaM_4X$_8$ with M=Mo as a group VIB element and V, Nb, Ta as a group VB element. X denotes either S or Se. These compounds are known to exhibit semiconducting behavior in the electrical resistivity, caused by hopping of electrons between well-separated metal clusters. The large separation of the tetrahedral metal (M_4) clusters is believed to be the origin of strong correlations. We show that recent calculations neglected an important type of structural distortions, namely those happening only within the M_4 unit upon a fixed angle $\alpha = 60°$ of the trigonal (fcc-like) cell. These internal distortions gain a significant amount of energy compared to the cubic cell and they are - to our knowledge - almost undetectable within powder x-ray diffraction. However, they strongly influence the band-structure by opening up a gap at the Fermi-energy. This, however, puts into question whether all compounds of this family are really called Mott insulators as stated elsewhere. In particular ferromagnetic GaMo$_4$S$_8$ and GaV$_4$S$_8$ are well described within DFT. Only the Nb and Ta-based representatives require a large effort due to the lack of magnetic long range order caused by frustrated AF M-M interactions.

6.3.1 Introduction

The Molybdenum cluster compounds GaM_4X$_8$ with M=Mo (group VIB), V, Nb, Ta (group VB) and X=S and Se are known to exhibit semiconducting behavior in the electrical resistivity. Regarding the crystal structure, GaMo$_4$X$_8$ with X=S,Se and GaV$_4$S$_8$ show a structural phase transitions from a cubic to a slightly distorted trigonal structure around T$_S \approx$ 50K [149]. Well below T$_S$ at temperatures T$_c \approx$ around 20 K ferromagnetism sets in. Contrarily, GaNb$_4$Se$_8$ and GaTa$_4$Se$_8$ are known to remain cubic and paramagnetic without magnetic long range order down to lowest temperatures. The latter compounds have been reported to be Mott insulators and to become superconducting under external pressure [150]. In this paper we show that recent calculations neglected an important structural degree of freedom [151, 149, 152, 153, 150]. Even though the change from cubic to trigonal structure has been correctly ascribed to a Peierls distortion originating from the M_4 clusters [151, 149], no notion has been taken the fact that the M_4 clusters can also distort in a geometry with ideal, fcc-like axes spanning an angle of $\alpha = 60.0°$. To our knowledge, small distortions of roughly 3% occurring only within the M_4 units are practically undetectable

within powder x-ray diffraction, in contrast to the strong broadening of the peaks in the case when the angle α deviates from 60°. In our calculations, however, the energy gain of distorting the M_4 units while fixing $\alpha = 60°$ in the cases of $GaMo_4S_8$ and GaV_4S_8 is significant, making it very likely that the M_4 tetrahedra also distort above the structural phase transition. This would be hardly detectable experimentally. Moreover, we believe that the neglect of these degrees of freedom in previous DFT investigations [151, 149, 152, 153, 150] led to an overestimation of the importance of electron-electron correlations. We find that M_4 distortions alone are enough to open up a gap at E_F. This shows that not all representatives of this family, in particular ferromagnetic $GaMo_4S_8$ and GaV_4S_8, can be called Mott insulators. If relaxations are performed properly, all compounds investigated exhibit a vanishing DOS at the Fermi energy, in agreement with experiment. Only the Nb and Ta based representatives have to be treated with care. Their strong AF M-M interactions prohibit long range order and the strong coupling between cluster geometry and magnetic configuration makes the investigation very difficult.

6.3.2 Results and discussion

All calculations were performed using the PAW-technique [20] as implemented in the VASP package [21]. For Ga a PAW potential with s, p and d electrons as valence states has been chosen, for X (S,Se) s and p electrons were treated as valence states. During all calculations a plane-wave expansion up to 400 eV was applied and at least 85 irreducible $\boldsymbol{k}$-points (for trigonal set-up) were used. In all cases the Wyckoff-positions were relaxed upon fixed volume and fixed cut-off. In the low-symmetry set-up the trigonal angle α was changed by hand and never relaxed automatically, avoiding too many degrees of freedom.

At high temperatures all cluster compounds of the type GaM_4X_8 with M=Mo,V,Nb, and Ta and X=S, Se crystallize in a face-centered cubic (fcc) phase (F$\bar{4}$3m) that can be derived from the spinel structure (Fd$\bar{3}$m, hypothetical $Ga_2M_4X_8$) by removing half of the Ga atoms. Complete ordering of the resulting vacancies finally results in the present structure having symmetry F$\bar{4}$3m. Some representatives like Mo-based $GaMo_4X_8$ with X=S, Se and V-based GaV_4S_8, however, undergo a structural phase transition upon cooling into a slightly distorted, trigonal structure (R3m). While the Mo-based compounds distort towards a trigonal angle α larger than the ideal (fcc) one of 60.0° (α_{exp}=60.53° for $GaMo_4S_8$), the V-based compounds distort in the opposite direction (α_{exp}=59.6 ° for GaV_4S_8). Both types order ferromagnetically below a T_c of 19.5 K, 26.7 K and 10 K for $GaMo_4S_8$, $GaMo_4Se_8$, and GaV_4S_8, respectively. For the Mo compounds metamagnetism with rather low magnetic critical fields has been reported [154]. Different from the above representatives, the Nb and Ta-based cluster compounds not only remain cubic down to lowest temperatures, they
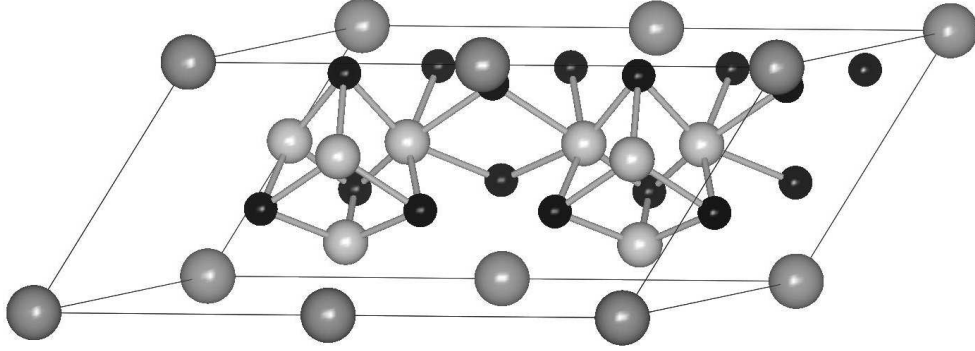
Figure 6.7: Doubled fcc unit cell. The corner atoms are Ga, the small bright atoms form the tetrahedral M_4 clusters and the small dark spheres are X. One can easily see the bridge between two M_4 clusters mediated by two X-atoms and a M-X-M angle of $\approx 104.6°$.

also exhibit no magnetic long-range order even though from the Curie law a magnetic moment of roughly 1 μ_B/f.u. has been extrapolated. A doubled unit-cell cell containing two formula units is shown in Fig. 6.7. In the cubic geometry the M_4 units build a fcc lattice and one M atom is connected via 2 X atoms with the neighboring cluster. For the low-temperature phase R3m trigonal axes were used. In the trigonal geometry all lengths are equivalent (a=b=c) and only the angle $\alpha = \beta = \gamma$ can be changed. The basis vectors $\vec{b_1}$, $\vec{b_2}$, and $\vec{b_3}$ are related to the simple cubic axes $\vec{A}$, $\vec{B}$, and $\vec{C}$ via

$$\begin{pmatrix} \vec{b_1} \\ \vec{b_2} \\ \vec{b_3} \end{pmatrix} = \frac{b}{\sqrt{1+2x+3x^2}} \begin{pmatrix} 1+x & x & x \\ x & 1+x & x \\ x & x & 1+x \end{pmatrix} \begin{pmatrix} \vec{A} \\ \vec{B} \\ \vec{C} \end{pmatrix}.$$

The length of all basis vectors is b. These vectors span the volume of the trigonal unit cell, V_T, given by

$$V_T = b^3 \frac{(1+3x)}{(1+2x+3x^2)^{3/2}}. \tag{6.1}$$

The quantity x is related to the angle α via the equation

$$x = -\frac{1}{3} + \sqrt{\frac{1}{9} - \frac{u}{3(u-1)}}, \tag{6.2}$$

u denotes the cosine of α. An angle of $\alpha = 60°$ (u=0.5, equivalent to fcc axes) results in $x = 1/3$. For simplicity, only α and the corresponding simple cubic lattice constant a_0 will be used. The quantity a_0 is related to the cell volume V_T via a_0=$(4V_T)^{1/3}$. The results for the cubic geometry are listed in Tab. 6.6. The optimized, cubic lattice constants a_0 are in

100

Table 6.6: Tabulated are the s.c. lattice constants a_0 [bohr], the intra (d_{intra}) and inter (d_{inter}) cluster M-M distances, the density of states at E_F ($N(E_F)$) [states/(eV f.u.)], the band-widths W in the FM state [eV] and the dimensionless ratios I/W relating Stoner I [eV] and band-width W [eV]. In all cases the cubic high-temperature phase was assumed.

Compound	a_0	d_{intra}/d_{inter}	$N(E_F)$	W [eV]	I/W
$GaMo_4S_8$	9.84(9.73)	2.85/4.10	45	0.570	1.09
$GaMo_4Se_8$	10.30	2.91/4.37	59	0.426	1.46
GaV_4S_8	9.68 (9.66)	2.84/4.00	10.3	0.401	1.76
GaV_4Se_8	10.19	2.93/4.27	12.4	0.296	2.39
$GaNb_4S_8$	10.06 (10.02)	2.99/4.12	7.1	0.689	0.87
$GaNb_4Se_8$	10.53 (10.42)	3.06/4.39	8.9	0.500	1.20
$GaTa_4S_8$	10.04	2.98/4.12	6.3	0.827	0.6
$GaTa_4Se_8$	10.51 (10.37)	3.04/4.39	8.9	0.604	0.8

good agreement with experiment, due to GGA they slightly overestimate the true volume. The DOS for the cubic compounds of interest is compared in fig. 6.8. It confirms that for all compounds only M-states are situated at E_F. While the cluster orbitals are almost filled for $GaMo_4X_8$ they are almost empty in the cases M=V, Nb, and Ta. Recently it has been pointed out that the cluster orbitals at E_F stem from bonding combinations of atomic, M-like t_{2g} orbitals [155]. For example in $GaMo_4X_8$ 6 electrons per Mo ($6\times4=24$ per cluster) and the 3 electrons per Ga, yielding a total number of 27 valence electrons, are available. From those $8\times2=16$ can be attributed to X, since it is most electronegative. The remaining 11 electrons per cluster almost completely fill the (4×3) Mo t_{2g} cluster orbitals.

6.3.3 Results for $GaMo_4S_8$, GaV_4S_8, $GaNb_4Se_8$, and $GaTa_4Se_8$

In the following paragraph the magnetic properties of the compounds $GaMo_4S_8$, GaV_4S_8, $GaNb_4Se_8$, and $GaTa_4Se_8$ will be compared. In order to describe the low-temperature phase (R3m) two types of distortions were taken into account. On the one hand the M_4 tetrahedra were allowed to distort and on the other hand the angles α spanned by the trigonal axes were modified by hand.

In the cubic structure only $GaMo_4S_8$ and GaV_4S_8 develop an integer magnetic moment of 1 μ_B per cluster. This is in agreement with experiments yielding FM states below T_c for the Mo- and V-based compounds. The Nb and Ta based representatives end up non-magnetic in our calculations, only in an AFM (1,0,0) set-up (the only one tested) small magnetic
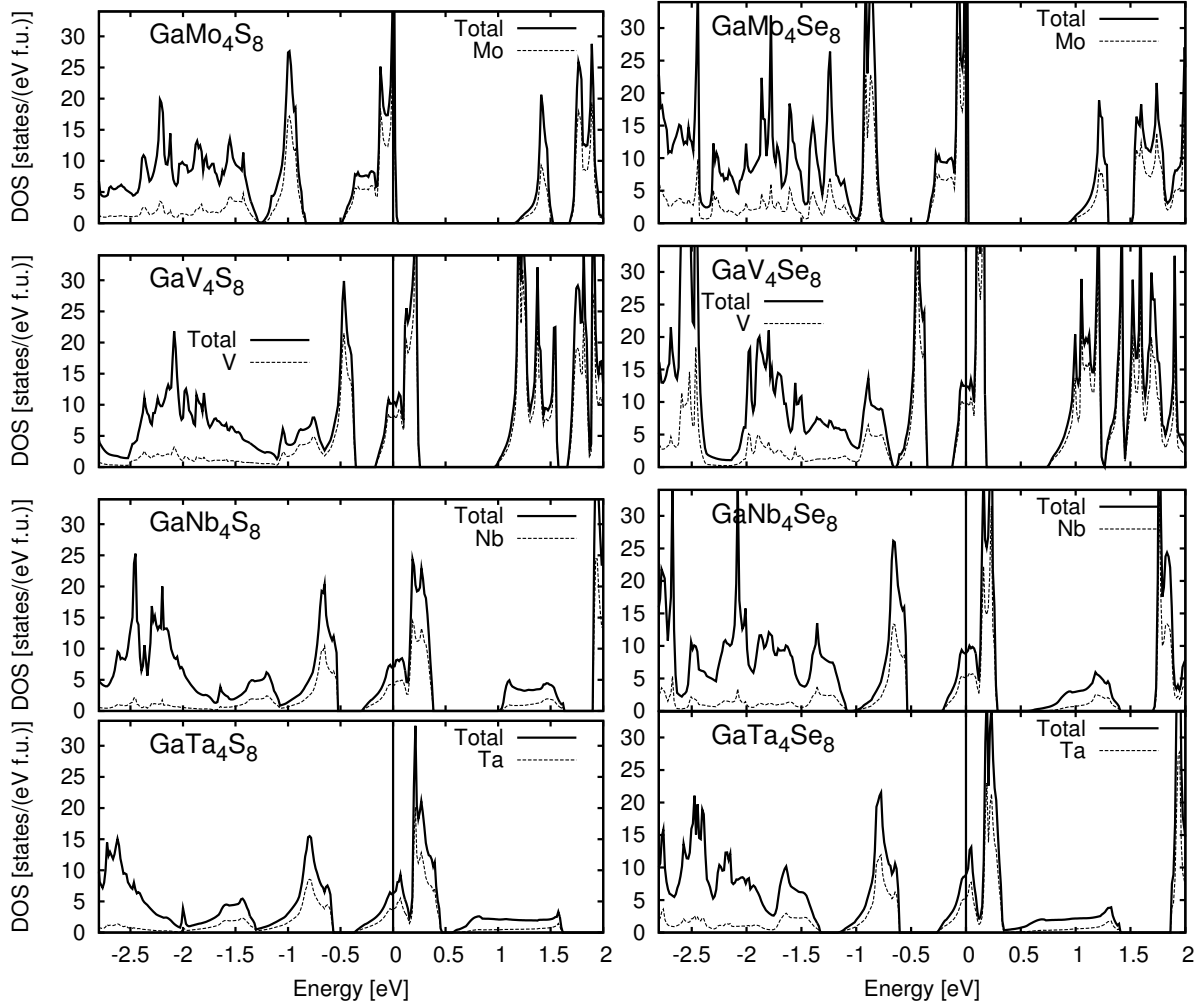
Figure 6.8: Total and M projected density of states (DOS) for the cubic compounds GaM_4X_8 with X=S (left panel) and Se (right panel) as well as M=Mo, V, Nb, and Ta.

moments on Nb/Ta arise. This is an indication of strong but frustrated AFM interactions present in cubic compounds $GaNb_4X_8$ and $GaTa_4X_8$. The plots of the energy versus the angle α for the compounds of interest are shown in fig. 6.9. Most easy to understand is $GaMo_4S_8$. In the cubic geometry the compound is clearly FM with an integer moment of $1 \ \mu_B$. This is due to one hole in the almost filled cluster orbital complex. Energetically the non-magnetic state is roughly 30 meV above the cubic FM state. The compound is
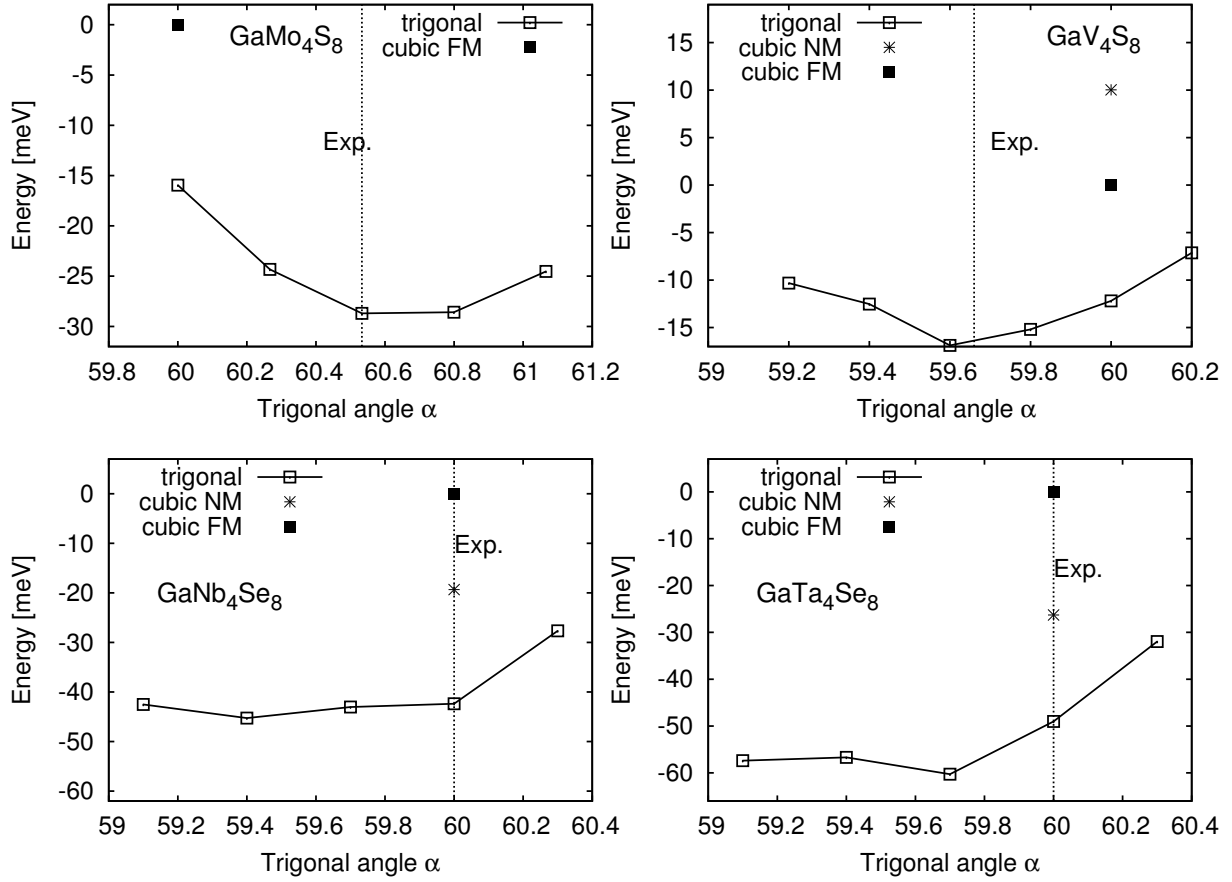
Figure 6.9: Energy versus trigonal angle α for selected compounds. Except for $GaMo_4S_8$, in addition to the cubic FM states also the cubic non-magnetic (NM) configurations are plotted.

a half-metal because of its vanishing DOS at E_F in the majority spin channel. When the Mo_4 tetrahedra are allowed to distort (transition from $F\overline{4}3m$ to R3m) upon fixed unit cell axes ($\alpha = 60.0°$), the total energy can already be lowered by 16 meV. Relaxing also the angle α further reduces the total energy by approximately 12 meV (see fig. 6.9). The angle found in our calculations (α=60.6°) is in very good agreement with the experimental one (α_{exp}=60.53°). Most impressive is the effect of the distortions on the DOS. We found that the cluster distortions alone are enough to open up the gap at E_F. A comparison between cubic and trigonal DOS is given in fig. 6.10. The gap in trigonal $GaMo_4S_8$ has a width of roughly 0.08 eV. It changes only slightly when α is modified but it is very sensitive to the degree of Mo_4 cluster distortion. Regarding the physical properties, the compound closest to $GaMo_4S_8$ is GaV_4S_8. However, in its cubic form the non-magnetic
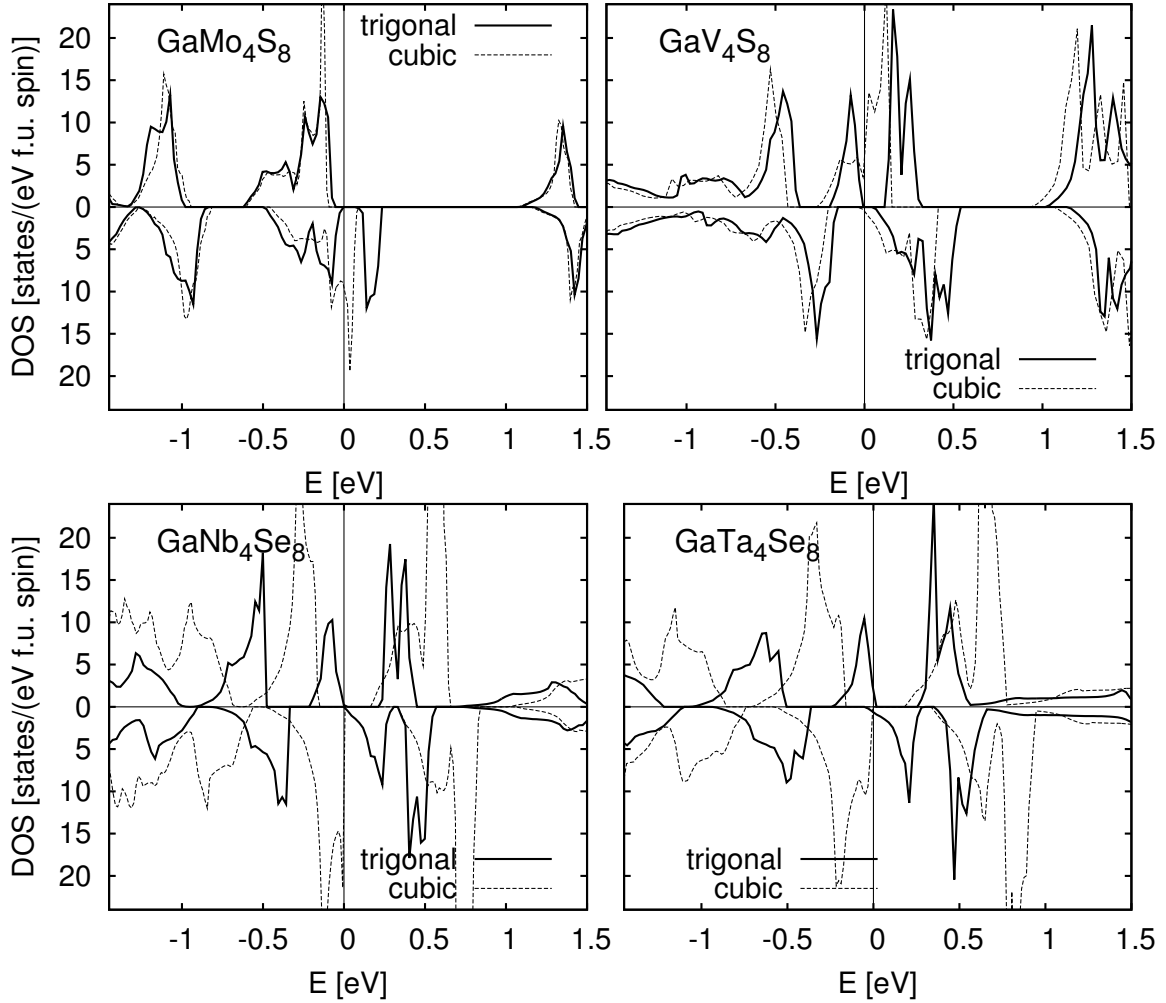
Figure 6.10: Comparison between total DOS for trigonal (always $\alpha = 60°!$) and cubic $GaMo_4S_8$ (upper left panel), GaV_4S_8 (upper right panel), $GaNb_4Se_8$ (bottom left panel), and $GaTa_4Se_8$ (bottom right panel). Only ferromagnetic configurations are compared, for M=Nb and Ta this is not the experimental ground state.

state is situated energetically only 10 meV above the FM one. Hence its FM state is strongly destabilized compared to $GaMo_4S_8$ (30 meV). Our calculations yield $\alpha \approx 59.6°$, again in very good agreement with experiment. The R3m configuration (distorted M_4 tetrahedron) with $\alpha = 60.0$ is more stable than the ideal, cubic (fcc) one by approximately 11 meV. Further relaxations of α yield only a lowering of the energy by 5 meV. This is again lower than the corresponding relaxation energy for $GaMo_4S_8$ (12 meV). The behavior of $GaNb_4Se_8$ and $GaTa_4Se_8$ is much more complex. In their cubic form they strongly disfavor

the FM state. Their cubic, non-magnetic state is lower in energy by 26 meV and 30 meV for Nb and Ta, respectively. The situation changes when cluster relaxations are taken into account. In that case the FM configuration can be stabilized without fixing the moment artificially. The internal Nb_4 and Ta_4 relaxations gain an energy of about 40 meV and 50 meV with respect to the cubic FM state. This is large compared to the change in the total energy when the angle α is modified (3 meV and 11 meV for M=Nb and Ta, respectively). However, this huge energy gain related to internal distortions is expected to be an artefact of assuming a FM state, which is not the experimental ground state. A comparison of the DOS between cubic and trigonal ($\alpha = 60°!$) geometry for the compounds of interest is given in fig. 6.10. In all cases M_4 distortions of about 3-4% significantly change the DOS. Thus also for M=Mo and V a strong pressure dependence of the electrical resistivity is expected.

In conclusion there is a big difference between the Mo/V based and the Nb/Ta-based compounds. Within the series Mo-V-Nb-Ta the DOS at E_F determined from the non-magnetic state steadily decreases. This reduction in $N(E_F)$ weakens the tendencies of structural distortions. As a consequence only the Mo and V-based representatives deviate from $\alpha = 60°$. However, it has to be checked whether M_4 distortions not also occur upon a fixed angle $\alpha = 60$ above the structural phase transition T_s. This is because powder X-ray diffraction is very insensitive to these types of structural changes, in contrast to changes in α, which are easy to identify. All compounds require a proper treatment of the internal degrees of freedom. This has not been taken into account up to now, but it must be included in all future DFT calculations. Moreover, our (plain) GGA calculations clearly yield a gap at E_F for trigonal $GaMo_4S_8$, indicating that this compound is not a Mott insulator as stated elsewhere [149]. This is because in the trigonal structure not correlations but cluster distortions create the gap at E_F. Hence correlation corrections like LDA+U are not necessary for trigonal $GaMo_4S_8$ to reproduce the gap. A similar situation is found for GaV_4S_8, even though its tendency to FM order is reduced compared to the Mo-based compound. The situation changes strongly for $GaNb_4Se_8$ and $GaTa_4Se_8$. Their (non-magnetic) DOS at E_F is of intermediate height. On the one hand it is not high enough to distort the lattice and to stabilize FM order in the cubic state, on the other hand the ratio of I/W for the cubic state is 1.2 and 0.8 for $GaNb_4Se_8$ and $GaTa_4Se_8$, placing them in the moderately correlated regime. While $GaMo_4S_8$ and GaV_4S_8 can be treated reasonably well within GGA, assuming a FM ground state, the Nb and Ta related compounds can only be treated reasonably if their magnetic configuration is accounted for correctly. Since these compounds show no long-range order and seem to have an extremely strong interplay between cluster distortions and magnetism, their description is difficult and would require a disordered local moment picture.
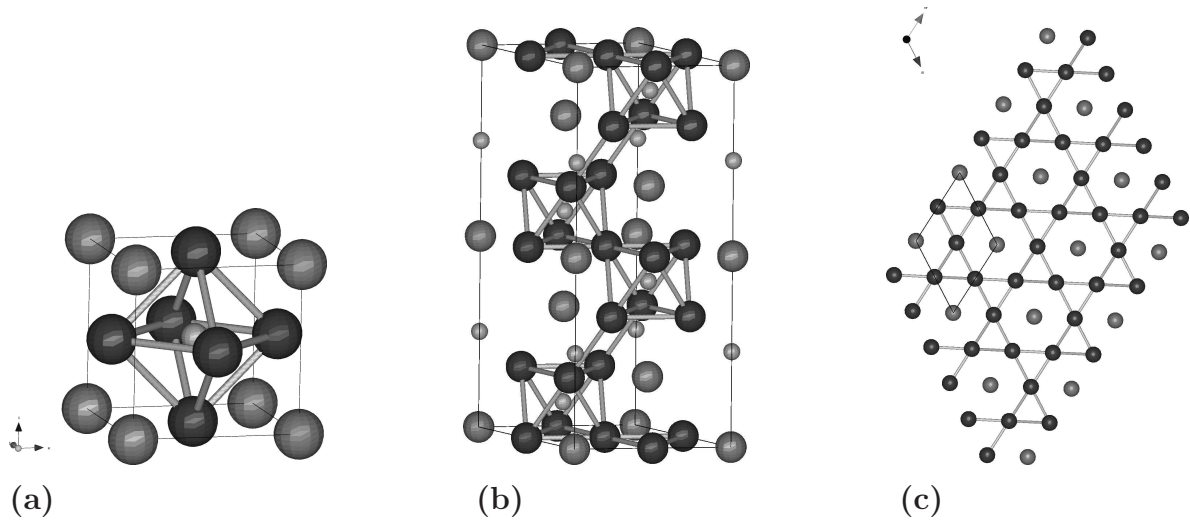
Figure 6.11: (a) Cubic unit cell of TNMn$_3$ accomodating one formula unit (f.u.). Mn is situated on the face centers, N in the center and T in the corner position of the cube. Only Mn-Mn bonds are plotted. The small spheres are N, the big unconnected ones are T. (b) Hexagonal cell with the c-axis pointing in the former, simple cubic (1,1,1) direction. (c) One layer (e.g. z=0) of the hexagonal cell, the Mn-Mn bonds form hexagons and triangles.

6.4 Mn-based anti-perovskites: The series TNMn$_3$

In the following section Mn-based perovskites will be discussed. Even though their crystal structure is very simple, the high concentration of Mn complicates their magnetic structures significantly. The Mn-based anti-perovskites TXMn$_3$ can roughly be divided into two groups, carbides and nitrides. Among the carbides most famous is probably GaCMn$_3$. It shows a first order phase transition around 160 K from an AFM ground state (FM planes couple AFM along the (1,1,1) direction) over an intermediate state (mixed AFM and FM) to a ferromagnetic phase above $\approx$ 164 K. Upon further heating GaCMn$_3$ becomes paramagnetic (around 249 K). This diversity of magnetic phases accompanies several interesting phenomena, e.g. a GMR effect [156] and a negative magnetocaloric effect [157]. Regarding their physical properties, the nitrides exhibit a similar complexity and richness. However, they have been studied less intensively in the past. Most challenging is ZnNMn$_3$. It exhibits a phase transition around 160 K from a non-collinear triangular magnetic state (similar to that in fig. 2.2) to a paramagnetic state with a resulting volume-change that is so abrupt that microcracks form. This can even be seen in the electrical resistivity, increasing stepwise with the number of thermic cycles [158]. Recently, Takenaga et al. [159, 160] showed that it is possible to broaden the phase-transition mediated jump in the

cell-volume by Ge doping in $Mn_3(Cu_{1-x}Ge_x)N$, so that a material highly desireable from a technical point of view having a large and continuous negative thermal expansion (NTE) can be obtained. Interestingly, in experiments D. Fruchart and E. F. Bertraut [161] found out that while nitrides tend towards non-collinear triangular magnetic structures carbides seem to prefer collinear structures.

In this section calculations for the nitride series $TNMn_3$, T=Cu, Zn, Ga, and Ge will be presented. For the first time also non-collinear magnetic configurations are taken into consideration. However, since the experimentally determined ground states are complex mixtures between collinear and triangular states (e.g. $CuNMn_3$) we concentrate on either purely collinear or triangular configurations. All calculations were performed using the VASP package [21]. For Mn and T (Cu, Zn, Ga and Ge) PAW potentials with s, d and p electrons as valence states have been chosen, for nitrogen a potential with $2s$ and $2p$ electrons as valence states was satisfactory. During all calculations a plane-wave expansion up to 400 eV was applied.

6.4.1 Bonding in non-magnetic $TNMn_3$ and $TCMn_3$

It is useful to start with an investigation of the non-magnetic trends in bonding within the nitride and carbide series $TNMn_3$ and $TCMn_3$, T denoting elements from Cu to Ge. Most of the compounds of interest crystallize in the ideal anti-perovskite structure (prototype $CaTiO_3$, No. 221, $Pm\overline{3}m$). Mn occupies the face centers of the cube, T the corners and N the center (see fig. 6.11). The structure is called anti-perovskite because the high-symmetry octahedral site is occupied by an anion (N/C) and not by a cation (Mn). The site symmetry of Mn is only tetragonal, only its d_{xz} and d_{yz} orbitals remain degenerate. From experiments D. Fruchart and E. F. Bertraut identified several trends in the physical properties within the series $Cu_{1-x}Ge_xNMn_3$, depending on the electron number on T [161]. For increasing x there is a transition from a tetragonal structure with c/a<1 (called T^-) over a cubic phase (C) to a tetragonal structure with c/a>1 (called T^+). A similar trend is also present in the carbide series, only the T^+ phase is absent. When nitrogen is substituted by carbon it turned out to be necessary to use higher Z numbers in order to obtain equivalent results. They also observed that the magnetic moment on Mn exhibits a peak at T=Ni and reduces linearly when the electron number Z on T increases. The density of states (DOS) for the Mn-based perovskites is shown in Fig. 6.12. E_F is situated roughly in the middle of the Mn-d states. While the s-like states of N/C are beyond the plotting region (typically around -12 eV for C and -16 eV for N), the N/C p-like states are situated between -8 eV and -5 eV. They play an important role in bonding. Compared to fcc Mn, the perovskites have one additional N/C atom in the center of the cubic unit-cell.

Table 6.7: Bader charges for T (s+d), N/C (s+p) and Mn (s+p+d) in the (hypothetical) non-magnetic state assuming a lattice constant of 3.8 Å.

compound	T	N / C	Mn
CuNMn$_3$	11.39	6.63	12.33
ZnNMn$_3$	12.00	6.65	12.45
GaNMn$_3$	13.07	6.62	12.44
GeNMn$_3$	14.28	6.57	12.38
CuCMn$_3$	11.31	5.74	12.31
ZnCMn$_3$	12.10	5.76	12.38
GaCMn$_3$	13.02	5.65	12.44
GeCMn$_3$	14.25	5.56	12.40

Thus each Mn has two N/C nearest neighbors at a very short distance. As a consequence the Mn d_{z^2}-like electron pointing towards N/C does not contribute to magnetism. In a molecular orbital picture it forms a σ bond with p-states on N/C creating bonding states around -8 eV (lower edge of N-p block) and antibonding ones above E_F. There also exists a π bond between N/C p and degenerate Mn (d_{xz},d_{yz}) states being responsible for the bonding peak around -6 eV (upper edge of N-p block) and the corresponding anti-bonding one situated around 1.5 eV. Due to symmetry, the d_{xy} and the $d_{x^2-y^2}$ states are non-bonding with respect to the nearest neighbor N/C p states. While for T=Cu and Zn the shape of the Mn-DOS is similar to a typical fcc element, the compounds with T=Ga and Ge have a clear triple-peak structure typical for bcc elements. This is because the Mn d_{xy} states point towards the T element, which deviates more and more from a transition metal the higher the number of p-electrons becomes (like in Ga and Ge).

From the shape of the Mn-d DOS carbides and nitrides are very similar. The only differences are the energetic positions of the p states, being situated at higher energies for the carbides. This implies that the Mn-C bond has more covalent character with a stronger admixture of Mn attributed states in the bondong band and a stronger admixture of carbon-like states in the anti-bonding band.

In table 6.7 the Bader charges [162] for the compounds of interest are listed. They were determined for a fixed lattice constant of 3.8 Å on a 60x60x60 grid using a numerical approach of G. Henkelman *et al.* [163] developed for the VASP code. By inspecting table 6.7 one finds that the charges on Mn and on N/C are rather insensitive to the choice of the T element. This is due to the fact that the main bonding in these compounds occurs between Mn and C/N, while T plays a minor role. Additional electrons on T stay localized at T and

are not transferred to Mn, since this would result in the occupation of anti-bonding states. This agrees well with earlier observations indicating that these compounds can well be described within a covalent picture [39]. The compounds of interest can roughly be seen as $T^0(C/N)^{-1.5}Mn^{+0.5}$. While amongst the nitrides the T=Zn member has the highest charge on Mn, amongst the carbides this is found for the T=Ga representative. This agrees well with the trend observed by D. Fruchart *et al.*[161], stating that the replacement of carbon by nitrogen seems to require the use of higher atomic numbers Z on T in order to obtain similar diagrams (e.g. for lattice distortions). Plotting differences in the charge densities revealed that the major change in the Mn d-DOS upon an increase of Z on T occurs for the non-bonding d_{xy} states of Mn. The latter become increasingly stable within the series T=Cu, Zn, Ga, and Ge and successively move through the Fermi energy (see Fig. 6.12). This is plausible because the d_{xy}-like charge spreads out towards T. Even though the coordination of 12 for T is much too high for conventional p-states to be strongly involved in bonding (e.g. elemental Ge has a coordination of 4), above results can be interpreted as weak signatures indicating a chemical bond between Ge and Mn.

6.4.2 Magnetic properties of the nitrides

For the study of the magnetic properties three different antiferromagnetic (AFM) configurations were adopted in our calculations. All directions are given with respect to the simple-cubic (s.c.) unit cell. The AFM (0,0,1) set-up is characterized by a spin propagation vector in the (0,0,1) direction. AF 120° denotes a triangular configuration with neighboring spins on the (1,1,1) plane rotated by 120°. Both of the latter can be implemented in the s.c. cell. For the third configuration, AFM (1,1,1) with propagation vector in (1,1,1) direction, a hexagonal cell containing 6 f.u. having its c-axis pointing in the s.c. (1,1,1) direction had to be used. In that geometry the characteristic layers built up from hexagons and triangles can be seen impressively (right panel of fig. 6.11). The coupling between layers is mediated either by Mn-Mn bonds (all Mn-Mn bonds are equidistant), or in particular by short Mn-N-Mn bonds. The number of FM ($\oplus$) and AFM ($\ominus$) aligned neighbors relative to one Mn are listed in table 6.8. It shows that the perovskite lattice is strongly frustrated. Mn has - unlike in fcc - only 8 Mn neighrest neighbors. In the case of AFM I one out of three Mn, lets say that one in the s.c z=0 plane, has all neighrest neighbors aligned AFM, whereas those two Mn on the face centers (z=0.5a) have at best 4 $\ominus$ and 4 $\oplus$ neighbors. This differentiation between two types of Mn is because the magnetic configuration breaks the symmetry of the lattice. In the AFM II configuration all three Mn have half of their neighbors coupled AFM. Thus if all interactions were AFM the Heisenberg model would predict the AFM I configuration to be more stable than the AF II. However, one has to

Table 6.8: Number and type ($\oplus \cdots$ parallel, $\ominus \cdots$ anti-parallel) of neighbors in the most common AFM configurations, relative to one particular Mn atom in the center.

interaction	FM		AFM I (1,0,0)	AFM II (111)	120 °
1st $(1/\sqrt{2})$ a	$8 \oplus$	2x	$4 \oplus$ / $4 \ominus$	$4 \oplus$ / $4 \ominus$	8x120
		1x	$8 \ominus$		
2nd a (via N)	$2 \oplus$		$2 \oplus$	$2 \ominus$	$2 \oplus$
2nd a (direct)	$4 \oplus$		$4 \oplus$	$4 \oplus$	$4 \oplus$
3rd $\sqrt{3/2}$ a	$16 \oplus$	2x	$8 \oplus$ / $8 \ominus$	$8 \oplus$ / $8 \ominus$	16x120
		1x	$16 \ominus$	-	
4th $\sqrt{2}$ a	$12 \oplus$		$12 \oplus$	$12 \oplus$	$12 \oplus$

account for the strong Mn-(C/N)-Mn nearest neighbor interactions.

In fig. 6.13 the total energies (left panel) and magnetic moments on Mn (right panel) for various magnetic configurations are plotted versus the lattice constant. For all cubic nitrides the non-collinear configuration has the lowest energy. This is because of the high Mn concentration and the fact that even the parent compound Mn_4N is strongly influenced by AFM Mn-Mn interactions. While in $CuNMn_3$ the FM configuration is energetically comparable to AFM (1,1,1), it is the most unfavorable set-up in the compound $GeNMn_3$. This is because of a triple-peak structure in the DOS for the representatives with T=Ga and Ge (see fig. 6.12), pinning the exchange splitting and thus the moment on Mn at too low values. Consequently the FM set-up is energetically destabilized. The reduced magnetic moment for FM $GaNMn_3$ and $GeNMn_3$ is clearly visible in the right panel of fig. 6.13. Regarding the AFM states, the AFM (0,0,1) configuration is destabilized and the AFM (1,1,1) one stabilized when passing from T=Cu to T=Ge. Comparing this with table 6.8 suggests that the early compounds (T=Cu,Zn) have FM 180° Mn-N-Mn exchange coupling, while the later compounds (T=Ga,Ge) have either much weaker FM or even AFM Mn-N-Mn coupling. Moreover, the compounds with T=Zn and Ga are expected to exhibit the strongest magneto-volume coupling because their equilibrium lattice constants are most sensitive to the magnetic configuration. The jumps in the Mn moments are most pronounced for $GaNMn_3$, indicating a transition from a low-moment to a high-moment state.

In conclusion, above results show that the main changes in the electronic structure for carbides and nitrides when passing through the series T=Cu, Zn, Ga, and Ge come from the increase in the number of p-electrons on T. This shifts the peak in the non-bonding Mn d_{xy} DOS through E_F, causing an intra-Mn charge redistribution since the total charge

remains almost constant. Moreover, the change in the shape of the DOS due to the increased importance of p-orbitals make a FM configuration more and more unfavorable. The Bader charges on Mn taken from the non-magnetic state are highest for the compounds $ZnNMn_3$ (12.45) and $GaCMn_3$ (12.44). The equivalence between $ZnNMn_3$ and $GaCMn_3$ mirrors the experimental observation that certain trends within carbides and nitrides (e.g. the structure) are similar, required that carbides containing T with atomic number Z are compared to nitrides with T having atomic number Z-1. This shift balances that C has one electron less than N. Above calculations also indicate that the nitrides are strongly influenced by short-ranged AFM interactions. This is plausible not only because the nitrides are closely related to ferri-magnetic Mn_4N, it would also explain the extreme sensitivity of the magnetic configuration on the intra-Mn charge distribution. Why nitrides tend to be non-collinear antiferromagnets and carbides rather collinear antiferromagnets could not be clarified yet and warrants further investigations. However, it must be related to the more ionic character of the Mn-N bond compared to the Mn-C bond. In order to make more precise predictions, however, more calculations including more of the complex, experimental crystal structures (like that for $CuNMn_3$) are required. Since nitrides/carbides exhibit a strong coupling between structure and magnetism, a high accuracy not only with respect to magnetic configurations but also with respect to structural relaxations is necessary.
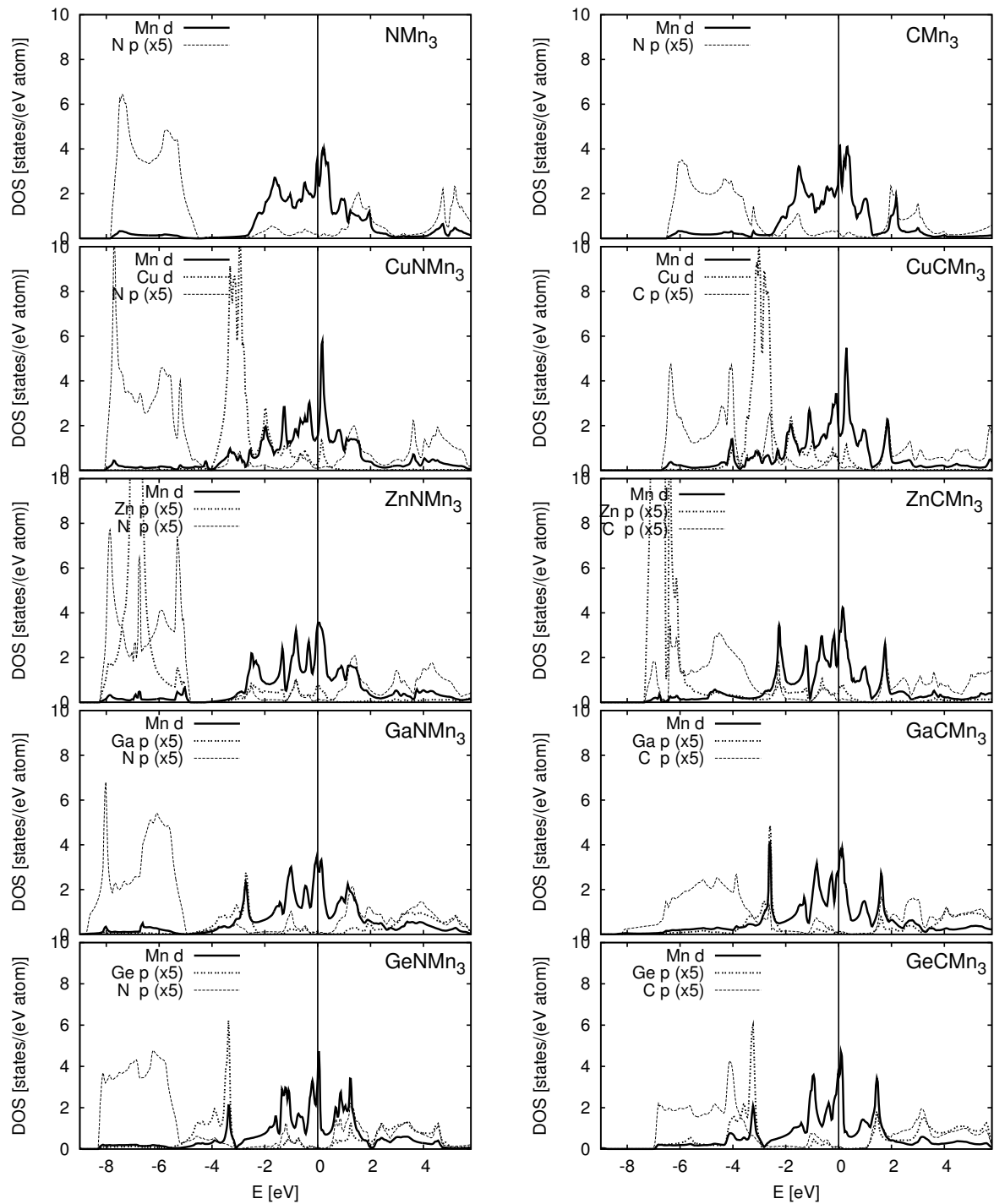
Figure 6.12: Site and symmetry projected density of states (DOS) for the compounds TNMn$_3$ (left column) and TCMn$_3$ (right column), with T ranging from Cu (uppermost row) to Ge (lowermost row). All p-like states have been multiplied by 5.
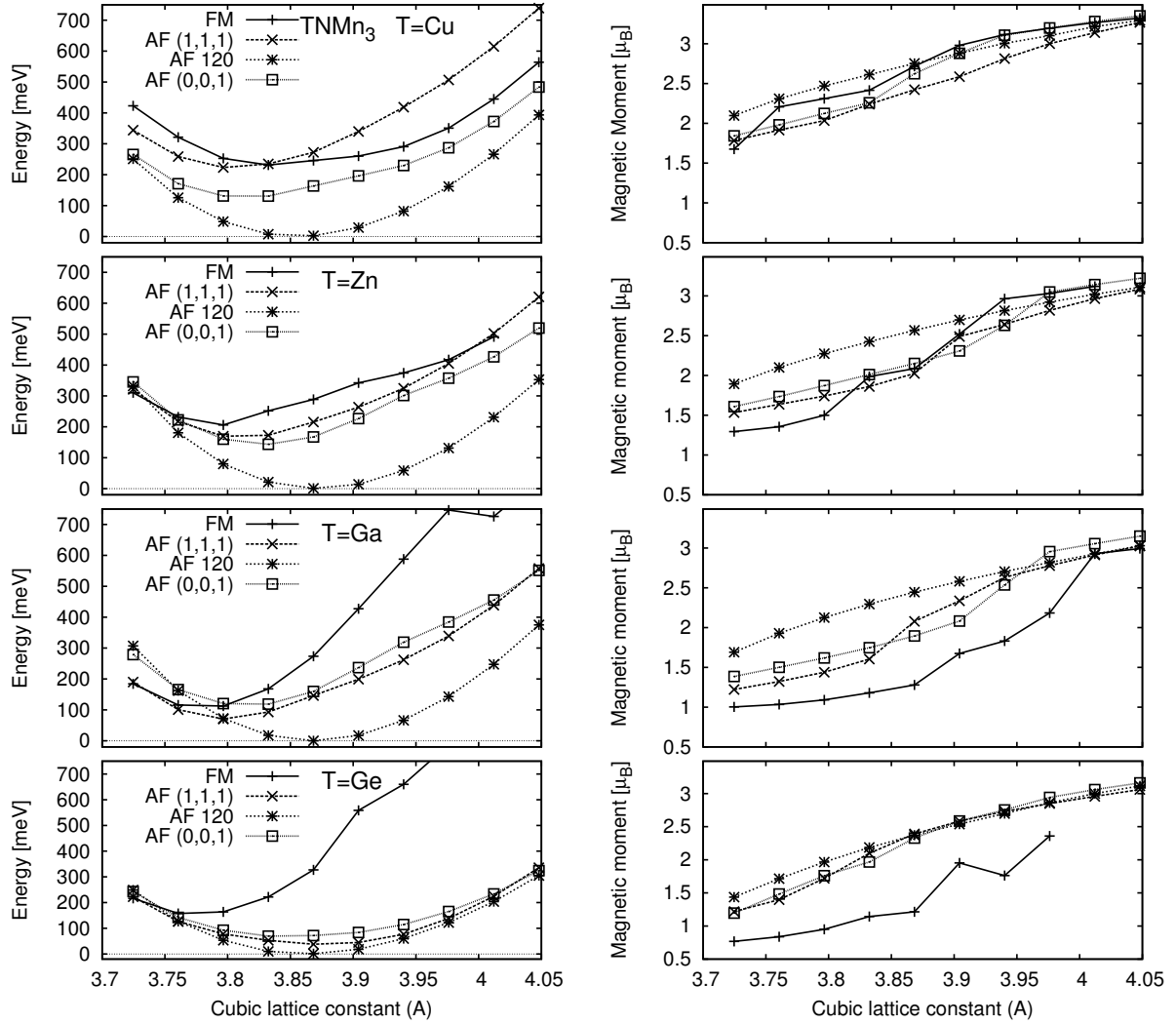
Figure 6.13: (Left panel) Energy versus s.c. lattice constant for various magnetic configurations: FM, AF(1,1,1) and AF(0,0,1) are collinear configurations, AF 120 denotes a state with neighboring Mn spins rotated by 120°. (Right panel) Moment on Mn (inside r=2.1 a.u.)

Bibliography

[1] J. C. SLATER and G. F. KOSTER, *Phys. Rev.* **94**, 1498 (1954).

[2] H. ESCHRIG, *The Fundamentals of Density Functional Theory*, B. G. Teubner Verlagsgesellschaft Stuttgart; Leipzig, 1996.

[3] L. H. THOMAS, *Proc. Cambridge. Phil. Soc.* **23**, 542 (1927).

[4] E. FERMI, *Z. Phys.* **48**, 73 (1928).

[5] W. KOHN and L. J. SHAM, *Phys. Rev.* **140**, A 1133 (1965).

[6] P. HOHENBERG and W. KOHN, *Phys. Rev.* **136**, B 864 (1964).

[7] JÜRGEN KÜBLER, *Theory of Itinerant Electron Magnetism*, Oxford University Press, New York, 2000.

[8] J. P. PERDEW and M. LEVY, *Phys. Rev. Lett.* **51**, 1884 (1983).

[9] J. P. PERDEW and A. ZUNGER, *Phys. Rev. B* **23**, 5048 (1980).

[10] V. I. ANISIMOV, J. ZAANEN, and O. K. ANDERSEN, *Phys. Rev. B* **44**, 943 (1991).

[11] I. V. SOLOVYEV, P. H. DEDERICHS, and V. I. ANISIMOV, *Phys. Rev. B* **50**, 16861 (1994).

[12] P. H. DEDERICHS, S. BLÜGEL, R. ZELLER, and H. AKAI, *Phys. Rev. Lett* **53**, 2512 (1984).

[13] A. BECKE, *J. Comp. Chem.* **98**, 1372 (1993).

[14] L. HEDIN, *Phys. Rev.* **139**, A796 (1965).

[15] M. SHISHKIN and G. KRESSE, *Phys. Rev. B* **74**, 035101 (2006).

[16] O. K. ANDERSON, *Phys. Rev. B* **12**, 3060 (1975).

[17] E. Wimmer, H. Krakauer, M. Weinert, and A. J. Freeman, *Phys. Rev. B* **24**, 864 (1981).

[18] http://www.uwm.edu/ weinert/flair.html, (2006).

[19] P. E. Blöchl, *Phys. Rev. B* **50**, 17953 (1994).

[20] G. Kresse and J. Joubert, *Phys. Rev. B* **59**, 1758 (1999).

[21] G. Kresse and J. Furthmüller, *Phys. Rev. B* **54**, 11169 (1999).

[22] N. W. Ashcroft and N. D. Mermin, *Festkörperphysik*, Oldenbourg Verlag München Wien, 2001.

[23] P. Mohn, *Magnetism in the solid state*, Springer series in solid-state sciences 134, Springer, Heidelberg, 2003.

[24] A. J. Pindor, J. Staunton, G. M. Stocks, and H. Winter, *J. Phys. F: Met. Phys.* **13**, 979 (1983).

[25] P. Soven, *Phys. Rev. B* **2**, 4715 (1970).

[26] O. N. Mryasov, U. Novak, K. Y. Guslienko, and R. W. Chantrell, *Europhys. Lett.* **69**, 805 (2004).

[27] M. H. Whangbo, H. J. Koo, and D. Dai, *J. Solid State Chem.* **176**, 417 (2003).

[28] A. I. Liechtenstein, M. I. Katsnelson, V. P. Antropov, and V. A. Gubanov, *J. Magn. Magn. Mater.* **67**, 65 (1987).

[29] W. Nolting, *Quantentheorie des Magnetismus*, B. G. Teubner, Stuttgart, 1986.

[30] D. Hobbs and J. Hafner, *J. Phys.: Condens. Matter* **13**, L681 (2001).

[31] A. Bergman, L. Nordström, A. B. Klautau, S. Frota-Pessôa, and O. Eriksson, *Phys. Rev. B* **73**, 174434 (2006).

[32] S. Nakatsuji, Y. Nambu, H. Tonomura, O. Sakai, S. Jonas, C. Broholm, H. Tsunetsugu, Y. Qiu, and Y. Maeno, *Science* **309**, 1697 (2007).

[33] S. A. Wolf, D. D. Awschalom, R. A. Buhrmann, J. M. Daughton, S. von Molnar, M. L. Roukes, A. Y. Chtchelkanova, and D. M. Treger, *SCIENCE* **294**, 1488 (2001).

[34] SANKAR DAS SARMA, *American Scientist* **89**, 516 (2001).

[35] R. A. DE GROOT and F. M. MÜLLER, *Phys. Rev. Lett.* **50**, 2024 (1983).

[36] I. TSUBOKAWA, *J. Phys. Soc. Jpn.* **15**, 1664 (1960).

[37] D. WEAIRE and M. F. THORPE, *Phys. Rev. B* **4**, 2508 (1971).

[38] D. G. PETTIFOR, *Bonding and Structure of Molecules and Solids*, Oxford University Press Inc., New York, 1995.

[39] J. B. GOODENOUGH, *Magnetism and the chemical bond*, John Wiley and Sons, Inc., 1963.

[40] L. PAULING, *The nature of the Chemical Bond*, Cornell Univ. Press, Ithaca, N.Y., 1960.

[41] C. PERSSON, YU-JUN ZHAO, S. LANY, and A. ZUNGER, *Phys. Rev. B* **72**, 035211 (2005).

[42] A. ZUNGER, *Appl. Phys. Lett.* **83**, 57 (2003).

[43] C. W. M. CASTLETON, A. HÖGLUND, and S. MIRBT, *Phys. Rev. B* **73**, 035215 (2006).

[44] P. KACMAN, *Semiconductor Science and Technology* **16**, R25 (2001).

[45] P. FAZEKAS, *Lecture Notes on Electron Correlation and Magnetism*, World Scientific Publishing Co. Pte. Ltd., 1999.

[46] T. DIETL, H. OHNO, and F. MATSUKURA, *Phys. Rev. B* **63**, 195205 (2001).

[47] J. M. D. COEY, M. VENKATESAN, and C. B. FITZGERALD, *Nat. Mater.* **4**, 173 (2005).

[48] J. OSORIO-GUILLÉN, S. L. S. V. BARABASH, and A. ZUNGER, *Phys. Rev. B* **75**, 184421 (2007).

[49] M. A. RUDERMAN and C. KITTEL, *Phys. Rev.* **96**, 99 (1954).

[50] P. MAHADEVAN, A. ZUNGER, and D. D. SARMA, *Phys. Rev. Lett.* **93**, 177201 (2004).

[51] P. W. ANDERSON, *Phys. Rev.* **79**, 350 (1950).

[52] H. Saito, W. Zaets, S. Yamagata, Y. Suzuki, and K. Ando, *J. Appl. Phys* **91**, 8085 (2002).

[53] J. Blinowski, P. Kacman, and J. A. Majewski, *Phys. Rev. B* **53**, 9524 (1996).

[54] C. Zener, *Phys. Rev.* **82**, 403 (1951).

[55] H. Akai, *Phys. Rev. Lett.* **81**, 3002 (1998).

[56] K. Sato, P. H. Dederichs, H. Katayama, and J. Kudrnovsky, *J. Phys.: Condens. Matter* **16**, 5491 (2004).

[57] M. Sieberer, J. Redinger, S. Khmelevskyi, and P. Mohn, *Phys. Rev. B.* **73**, 024404 (2006).

[58] K. Kusakabe, M. Geshi, H. Tsukamoto, and N. Suzuki, *J. Phys.: Condens. Matter* **16**, 5639 (2004), see also cond-mat/0402641 v1.

[59] M. S. Park, J. S. Giim, S. H. Park, Y. W. Lee, S. I. Lee, and E. J. Choi, *Supercond. Sci. Technol.* **17**, 274 (2004).

[60] P. Esquinazi, D. Spemann, R. Höhne, A. Setzer, K.-H. Han, and T. Butz, *Phys. Rev. Lett.* **91**, 227201 (2003).

[61] K. Kusakabe and M. Maruyama, *Phys. Rev. B* **67**, 092406 (2003).

[62] P. O. Lehtinen, A. S. Foster, Yuchen Ma, A. V. Krasheninnikov, and R. M. Nieminen, *Phys. Rev. Lett.* **93**, 187202 (2004).

[63] Z. Wu, D. J. Singh, and R. E. Cohen, *Phys. Rev. B* **69**, 193105 (2004).

[64] W. Kohn and L. J. Sham, *Phys. Rev.* **40**, A 1133 (1965).

[65] J. Perdew, K. Burke, and M. Ernzerhof, *Phys. Rev. Lett.* **77**, 3865 (1996).

[66] *http://cst-www.nrl.navy.mil/lattice/struk/b4.html* (2005).

[67] P. L'Haridon, J. Guyader, and M. Hamon, *Revue de Chimie minerale* **13**, 185 (1976).

[68] M. S. Miao and W. R. L. Lambrecht, *Phys. Rev. B* **71**, 064407 (2005).

[69] F. D. Murnaghan, *Proc. Nat. Acad. Sci. USA* **30**, 244 (1944).

[70] M. Geshi, K. Kusakabe, H. Tsukamoto, and N. Suzuki, *AIP Conf. Proc.* **772**, 327 (2005).

[71] B. Sanyal, L. Bergqvist, and O. Eriksson, *Phys. Rev. B* **68**, 054417 (2003).

[72] Wen-Hui Xie, Bang-Gui Liu, and D. G. Pettifor, *Phys. Rev. B* **68**, 134407 (2003).

[73] I. Galanakis and P. Mavropoulos, *Phys. Rev. B* **67**, 104417 (2003).

[74] J. Kübler, A. R. Williams, and C. B. Sommers, *Phys. Rev. B* **28**, 1745 (1983).

[75] L. M. Sandratskii, *Phys. Stat. Solidi B* **135**, 167 (1986).

[76] A. R. Williams, J. Kübler, and C. D. Gelatt Jr., *Phys. Rev. B* **19**, 6094 (1979).

[77] J. C. Slater and G. F. Koster, *Phys. Rev.* **94**, 1498 (1954).

[78] W. A. Harrison, *Electronic Structure and the Properties of solids, W. H. Freeman and Company, San Francisco* (1980).

[79] Ya-Qiong, Bang-Gui Liu, and D. G. Pettifor, *Phys. Rev. B* **66**, 184435 (2002).

[80] E. H. Lieb, *Phys. Rev. Lett.* **62**, 1201 (1989).

[81] Y. Nagaoka, *Phys. Rev.* **147**, 392 (1966).

[82] H. Tasaki, *Phys. Rev. Lett.* **75**, 4678 (1995).

[83] A. Mielke, *Phys. Rev. Lett.* **82**, 4312 (1998).

[84] M. Wei, N. Braddon, D. Zhi, P. A. Midgley, S. K. Chen, M. G. Blamire, and J. L. MacManus-Driscoll, *Appl. Phys. Lett.* **86**, 072514 (2005).

[85] L. Pan, H. Zhu, C. Fan, W. Wang, Y. Zhang, and J. Q. Xiao, *J. Appl. Phys.* **97**, 10D318 (2005).

[86] M. Ivill, M. E. Overberg, C. R. Abernathy, D. P. Norton, A. F. Hebard, N. Theodoropoulou, and J. D. Budai, *Solid-State Electronics* **47**, 2215 (2003).

[87] S. N. Kale, S. B. Ogale, S. R. Shinde, M. Sahasrabuddhe, V. N. Kulkarni, R. L. Greene, and T. Venkatesan, *Appl.Phys. Lett.* **82**, 2100 (2003).

[88] A. Martinez-Ruiz, M. G. Moreno, and N. Takeuchi, *Solid State Sciences* **5**, 291 (2003).

[89] S. L. Dudarev, G. A. Botton, S. Y. Savrasov, C. J. Humphreys, and A. P. Sutton, *Phys. Rev. B* **57**, 1505 (1998).

[90] A. P. Young and C. M. Schwartz, *J. Phys. Chem. Solids* **30**, 249 (1969).

[91] A. Werner and H. D. Hochheimer, *Phys. Rev. B* **25**, 5929 (1982).

[92] J. Ghijsen, L. H. Tjeng, J. van Elp, H. Eskes, and M. T. Czyzyk, *Phys. Rev. B* **38**, 11322 (1988).

[93] R. Laskowski, P. Blaha, and K. Schwarz, *Phys. Rev. B* **67**, 075102 (2003).

[94] L. E. Orgel, *J. Chem. Soc.* , 4186 (1958).

[95] P. Marksteiner, P. Blaha, and K. Schwarz, *Z. Phys. B.:Condens. Mater.* **64**, 119 (1986).

[96] L. Kleinmann and K. Mednick, *Phys. Rev. B* **21**, 1549 (1980).

[97] E. Ruiz, S. Alvarez, P. Alemany, and R. A. Evarestov, *Phys. Rev. B* **56**, 7189 (1997).

[98] W. Y. Ching, Young-Nian Xu, and K. W. Wong, *Phys. Rev. B* **40**, 7684 (1989).

[99] H. Kikuchi and K. Tonooka, *Thin Solid Films* **486**, 33 (2005).

[100] R. Bader, *Atoms in Molecules: A Quantum Theory*, Oxford University Press, New York, 1990.

[101] G. Henkelman, A. Arnaldsson, and H. Jonsson, *Comput. Mater. Sci.* **36**, 254 (2006).

[102] R. Haugsrud and T. Norby, *J. Electrochem. Soc.* **146**, 999 (1999).

[103] O. Porat and I. Riess, *Solid State Ionics* **74**, 229 (1994).

[104] M. Sieberer, S. Khmelevskyi, and P. Mohn, *Phys. Rev. B* **74**, 014416 (2006).

[105] M. Sieberer, P. Mohn, and J. Redinger, *Phys. Rev. B.* **75**, 024431 (2007).

[106] T. MORIYA, *Spin-fluctuations in the itinerant electron magnetism*, Springer-Verlag, Berlin, 1987.

[107] Y. TAKAHASHI, *J. of Phys.: Condens. Mat.* **13**, 6323 (2001).

[108] S. S. SAXENA, P. AGARWAL, K. AHILAN, F. M. GROSCHE, R. K. W. HASSEL-WIMMER, M. J. STEINER, E. PUGH, I. R. WALKER, S. R. JULIAN, P. MONTHOUGH, G. G. LONZARICH, A. HUXLEY, I. SHEIKIN, D. BRAITHWAITE, and J. FLOUQUET, *Nature(London)* **406**, 587 (2000).

[109] C. PFLEIDERER, D. REZNIK, L. PINTSCHOVIUS, H. v. LÖHNEYSEN, M. GARST, and A. ROSCH, *Nature(London)* **427**, 227 (2004).

[110] H. YAMADA and T. GOTO, *Phys. Rev. B* **68**, 184470 (2003).

[111] O. TEGUS, E. BRÜCK, K. H. J. BUSCHOW, and F. R. DE BOER, *Nature (London)* **415**, 150 (2002).

[112] E. P. WOHLFARTH and P. RHODES, *Phil. Mag.* **7**, 1817 (1962).

[113] H. YAMADA, *Phys. Rev. B* **47**, 11211 (1993).

[114] T. GOTO, T. SAKAKIBARA, K. MURATA, and H. KOMATSU, *Solid State Commun.* **12**, 945 (1989).

[115] H. MICHOR, M. EL-HAGARY, M. D. MEA, M. W. PIEPER, M. REISSNER, G. HILSCHER, S. KHMELEVSKYI, P. MOHN, G. SCHNEIDER, G. GIESTER, and P. ROGL, *Phys. Rev. B* **69**, 081404 (1989).

[116] A. V. ANDREEV, M. I. BARTASHEVICH, T. GOTO, K. KAMISHIMA, L. HAVELA, and V. SECHOVSKÝ, *Phys. Rev. B* **55**, 5847 (1997).

[117] A. FUJITA, S. FUJIEDA, Y. HASEGAVA, and K. FUKAMICHI, *Phys. Rev. B* **67**, 104416 (2003).

[118] M. NICKLAS, M. BRANDO, G. KNEBEL, F. MAYR, W. TRINKL, and A. LOIDL, *Phys. Rev. Lett.* **82**, 4268 (1999).

[119] V. KEPPENS, D. MANDRUS, B. C. SALES, B. C. CHAKOUMAKOS, P. DAI, R. COLDEA, M. B. MAPLE, D. A. GAJEWSKI, E. J. FREEMAN, and S. BENNINGTON, *Nature* **395**, 876 (1998).

[120] Y. AOKI, H. SUGAWARA, and H. SATO, *J. of Alloys and Comp.* **21**, 408 (2006).

[121] H. Jacobs and U. Zachwieja, *J. Less-Common Met.* **170**, 185 (1990).

[122] U. Zachwieja and H. Jacobs, *J. Less-Common Met.* **161**, 175 (1990).

[123] M. G. Moreno-Armenta, A. Martinez-Ruiz, and N. Takeuchi, *Solid State Sci.* **6**, 9 (2004).

[124] U. Hahn and W. Weber, *Phys. Rev. B* **53**, 12684 (1995).

[125] I. I. Mazin and D. J. Singh, *Phys. Rev. B* **69**, 020402 (2004).

[126] T. Jeong and W. E. Pickett, *Phys. Rev. B* **70**, 075114 (2004).

[127] S. Khmelevskyi, P. Mohn, J. Redinger, and M. Weinert, *Phys. Rev. Lett.* **94**, 146403 (2005).

[128] P. Larson, I. I. Mazin, and D. J. Singh, *Phys. Rev. B* **69**, 064429 (2004).

[129] A. Aguayo, I. I. Mazin, and D. J. Singh, *Phys. Rev. Lett.* **92**, 147201 (2004).

[130] S. Khmelevskyi, I. Turek, and P. Mohn, *J. Phys.: Cond. Mat.* **14**, 13799 (2002).

[131] T. He et al, *Nature (London)* **411**, 54 (2001).

[132] M. D. Johannes and W. E. Pickett, *Phys. Rev. B* **70**, 060507(R) (2004).

[133] P. Tong, Y. P. Sun, X. B. Zhu, and W. H. Song, *Phys. Rev. B* **73**, 245106 (2006).

[134] A. F. Dong, G. C. Che, W. W. Huang, S. L. Jia, H. Chen, and Z. X. Zhao, *Physica C* **422**, 65 (2005).

[135] J. B. Goodenough and M. Longo, *Landolt-Boernstein - Group II Condensed Matter*, volume 4, Springer Berlin / Heidelberg, 1970.

[136] Ph. L'Heritier, D. Fruchart, R. Madar, and R. Fruchart, *Alloys and Compounds of d-Elements with Main Group Elements. Part 2*, volume 4 of *Landolt-Börnstein - Group II Condensed Matter*, Springer Berlin / Heidelberg, 1970.

[137] C. M. I. Okoye, *Solid State Commun.* **136**, 605 (2005).

[138] J. P. Perdew and A. Zunger, *Phys. Rev. B.* **23**, 5048 (1981).

[139] D. M. Ceperley and B. J. Alder, *Phys. Rev. Lett.* **45**, 566 (1980).

[140] W. B. PEARSON, *A Handbook of Lattice Spacings and Structures of Metals and Alloys*, Pergamon, New York, 1958.

[141] G. Y. GUO, Y. K. WANG, and L.-S. HSU, *J. Magn. Magn. Mater.* **239**, 91 (2002).

[142] D. J. SINGH and I. I. MAZIN, *Phys. Rev. B* **64**, 140507(R) (2001).

[143] H. ROSNER, R. WEHT, M. D. JOHANNES, W. E. PICKETT, and E. TOSATTI, *Phys. Rev. Lett.* **88**, 027001 (2001).

[144] S. B. DUGDALE and T. JARLBORG, *Phys. Rev. B* **64**, 100508(R) (2001).

[145] G. L. KRASKO, *Phys. Rev. B* **36**, 8565 (1987).

[146] J. R. SCHRIEFFER, *J. Appl. Phys.* **30**, 1049 (1969).

[147] A. AGUAYO, I. I. MAZIN, and D. J. SINGH, *Phys. Rev. Lett* **92**, 147201 (2004).

[148] (2006).

[149] R. POCHA, D. JOHRENDT, and R. PÖTTGEN, *Chem. Mater.* **12**, 2882 (2000).

[150] M. M. ABD-ELMEGUID, B. NI, D. I. KHOMSKII, R. POCHA, D. JOHRENDT, X. WANG, and K. SYASSEN, *Phys. Rev. Lett.* **93**, 126403 (2004).

[151] H. MÜLLER, W. KOCKELMANN, and D. JOHRENDT, *Chem. Mater.* **18**, 2174 (2006).

[152] R. POCHA, D. JOHRENDT, BINGFANG NI, and M. ABD-ELMEGUID, *J. Am. Chem. Soc.* **127**, 8732 (2005).

[153] N. SHANTHI and D. D. SARMA, *J. Solid. State. Chem.* **148**, 143 (1999).

[154] A. K. RASTOGI and E. P. WOHLFARTH, *Phys. stat. sol.* **142**, 569 (1987).

[155] H. NAKAMURA, H. CHUDO, and M. SHIGA, *J. Phys.: Condens. Mater* **17**, 6015 (2005).

[156] K. KAMISHIMA, T. GOTO, H. NAKAGAWA, N. MIURA, M. OHASHI, and N. MORI, *Phys. Rev. B* **63**, 024426 (2000).

[157] T. TOHEI, H. WADA, and T. KANOMATA, *J. Appl. Phys.* **94**, 1800 (2003).

[158] W. S. KIM, E. O. CHI, J. C. KIM, N. H. HUR, K. W. LEE, and Y. N. CHOI, *Phys. Rev. B* **68**, 172402 (2003).

[159] K. Takenaka and H. Takagi, *Materials Transactions* **47**, 471 (2006).

[160] K. Takenaka and H. Takagi, *Appl. Phys. Lett.* **87**, 261902 (2005).

[161] D. Fruchart and E. F. Bertraut, *J. Phys. Soc. Jpn.* **44**, 781 (1977).

[162] R. Bader, *Atoms in Molecules: A Quantum Theory*, Oxford University Press, New York, 1990.

[163] G. Henkelman, A. Arnaldsson, and H. Jonsson, *Computational Materials Science* **36**, 354 (2006).

Acknowledgments

I want to express my honest gratefulness to my supervisor Peter Mohn, not only for his scientific encouragement during the last years but also for providing me a very pleasant working atmosphere.

Thanks also to Josef Redinger for his assistance in the form of many, time-consuming discussions about various, interesting topics.

Thanks to Peter Weinberger, Jan Zabloudil, Robert Hammerling, and Maria Nassey for their help in both, scientific and administrative affairs.

I also want to thank Raimund Podloucky at the Institute of Physical Chemistry for putting time and effort into reading the present work.

I also wish to thank all other members of the Center for Computational Materials Science, not only for providing the technical environment but also for creating a friendly and helpful atmosphere. At this place I also want to mention Sergej Khmelevskyi, Tanya Khmelevska, Corinna Etz, and Irene Reichl.

Thanks to Herwig Michor and Gerfried Hilscher. Their contribution to my experimental physics education during my diploma thesis helped me to write this work.

Last but not least I want to thank my family for their personal encouragement and their aid in many matters.

Curriculum Vitae

Personal data

Name:	Martin Sieberer
Address:	Frauentorgasse 15, A-3430 Tulln, Austria
Born:	June 26, 1981 in Vienna, Austria
Parents:	Waltraut Sieberer and Alfred Sieberer
Marital status:	unmarried, no children
Languages	German, English

Education

1987-1991	elementary school in Tulln
1991-1999	grammar school in Tulln (BRG), emphasis on science, finished with distinction in June 1999

Studies

1999-2004	Technical Physics at Technische Universität Wien, Austria, main focus on solid state physics
Nov 2001	First diploma examination passed with distinction
Dez 2003 - Aug 2004	diploma thesis: 'Selten-Erd Nickel Boronitride: Präparation und supraleitende Eigenschaften', supervisor Ao. Univ. Prof. Dr. Herwig Michor, Institut für Festköperphysik
Oct 2004	diploma degree with distinction
Since Feb. 2005	PhD student at the Center for Computational Materials Science (CMS), supervisor Ao. Univ. Prof. Dr. Peter Mohn

List of publications by M. Sieberer

M. Sieberer, J. Redinger, and P. Mohn, *Electronic and magnetic structure of cuprous oxide Cu_2O doped with Mn, Fe, Co, and Ni: A density-functional theory study*, Phys. Rev. B **75**, 035203 (2007).

M. Sieberer, P. Mohn, and J. Redinger, *Role of carbon in $AlCNi_3$ and $GaCNi_3$: A density functional theory study*, Phys. Rev. B **75**, 024431 (2007).

M. Sieberer, S. Khmelevskyi, and P. Mohn, *Magnetic instability within the series TCu_3N (T=Pd, Rh, and Ru): A first-principles study*, Phys. Rev. B **74**, 014416 (2006).

M. Sieberer, J. Redinger, S. Khmelevskyi, and P. Mohn, *Ferromagnetism in tetrahedrally coordinated compounds of I/II-V elements: Ab initio calculations*, Phys. Rev. B **73**, 024404 (2006).

M. Sieberer, H. Michor, S. Manalo, M. Della Mea, G. Hilscher, A. Grytsiv, and P. Rogl, *The effect of hydrogenation upon superconductivity in layered $La_3Ni_2B_2N_{3-\delta}$*, Physica **B** 378-380, pp 904 (2006).

R. Lackner, M. Sieberer, H. Michor, G. Hilscher, E. Bauer, P. S. Salamakha, O. L. Sologub, and K. Hiebl, *Low temperature properties of the ternary compounds $CePt_2B$ and $CePt_3B$* , J. Phys.: Condens. Matter **17**, S905−S910 (2005).

E. Bauer, G. Hilscher, H. Michor, M. Sieberer, E.W. Scheidt, A. Gribanov, Yu. Seropegin, P. Rogl, A. Amato, W.Y. Song, J.-G. Park, and D.T. Adroja, *Unconventional superconductivity and magnetism in $CePt_3Si_{1-x}Ge_x$*, Physica **B** 359-361, pp 360 (2005).

E. Bauer, R. Lackner, G. Hilscher, H. Michor, M. Sieberer, A. Eichler, A. Gribanov, Y. Seropegin, and P. Rogl, *$REPt_3Si$ (RE = La, Pr, Nd, Sm and Gd): isotypes of the heavy fermion superconductor $CePt_3Si$* , J. Phys.: Condens. Matter **17**, 1877 (2005).

E. Bauer , G. Hilscher, H. Michor, M. Sieberer, E.W. Scheidt, A. Gribanov, Yu. Seropegin, P. Rogl, A. Amato, W.Y. Song, J.-G. Park, D.T. Adroja, M. Nicklas, G. Sparn, M. Yogi, and Y. Kitaoka, *Unconventional superconductivity and magnetism in $CePt_3Si_{1-x}Ge_x$*, Physica **B** 359−361, pp 360 (2005).